SEASON

Self-Managed Sustainable High-Capacity Optical Networks

This project is supported by the SNS Joint Undertaken through the European Union's Horizon RIA research and innovation programme under grant agreement No. 101096120

Deliverable D2.2

Techno-economic Analysis: First Results

Editor A. Souza (INF-P)

Contributors INF-P, TIM, ADVA, TID, UC3M, UPC, INF-G, ACC, ERI + WEST and CNIT

Version 2.0

Date February 11, 2025

Distribution PUBLIC (PU)

DISCLAIMER

This document contains information which is proprietary to the SEASON consortium members that is subject to the rights and obligations and to the terms and conditions applicable to the Grant Agreement number 101096120. The action of the SEASON consortium members is funded by the European Commission.

Neither this document nor the information contained herein shall be used, copied, duplicated, reproduced, modified, or communicated by any means to any third party, in whole or in parts, except with prior written consent of the SEASON consortium members. In such case, an acknowledgement of the authors of the document and all applicable portions of the copyright notice must be clearly referenced. In the event of infringement, the consortium members reserve the right to take any legal action it deems appropriate.

This document reflects only the authors' view and does not necessarily reflect the view of the European Commission. Neither the SEASON consortium members as a whole, nor a certain SEASON consortium member warrant that the information contained in this document is suitable for use, nor that the use of the information is accurate or free from risk, and accepts no liability for loss or damage suffered by any person using this information.

The information in this document is provided as is and no guarantee or warranty is given that the information is fit for any particular purpose. The user thereof uses the information at its sole risk and liability.

Dissemination Level	SEN (Sensitive - limited under the conditions of the Grant Agreement)

REVISION HISTORY

Revision	Date	Responsible	Comment
0.1	October 16, 2024	A. Souza (INF-P)	Table of Contents
1.0	January 31, 2025	A. Souza (INF-P)	Complete version
1.1	February 3, 2025	M. Quagliotti (TIM)	Final revision
2.0	February 11, 2025	C. Pinho	Final version quality checked

LIST OF AUTHORS

Partner	Name Surname
CNIT	Filippo Cugini
CTTC	Laia Nadal
ADVA	Arantxa Villavicencio Paz, Achim Autenrieth
TID	José Manuel Rivas-Moscoso, Antonio Melgar, Óscar González de Dios
UC3M	Farhad Arpanaei, José Alberto Hernández, Fernando Díaz de María
TIM	Marco Quagliotti, Mauro Agus
UPC	Marc Ruiz, Luis Velasco, Jaume Comellas, Olga Muñoz, Josep Vidal
INF-P	André Souza, Cátia Pinho
INF-G	Carlos Castro, Mohammad Hosseini, Antonio Napoli
WEST	Andrea Marotta, Carlo Centofanti
ACC	Simon Pryor, Stephen Parker
ERI	Gianluca Gambari, Roberto Magri

EXECUTIVE SUMMARY

This report is the first of two deliverables that will present the CAPEX and OPEX benefits of the technologies developed in the SEASON project compared to current technologies. It includes the results of techno-economic evaluations from the first two years of the project. The remaining results will be presented in the next Deliverable 2.3. Both deliverables D2.2 and D2.3 are built upon the overall architecture and reference network scenarios defined in Tasks 2.1 and 2.2 and presented in deliverable D2.1 [SeaD2.1].

All techno-economic-related key performance indicators (KPIs) have at least one ongoing or planned activity described in this report. Some activities are still in the ideation stage, with planned activities in the first semester of 2025. Others have initial results, mostly related to the complexity, number of devices, and energy consumption benefits of the developed technologies. The extension of these initial studies to CAPEX and OPEX analysis will be based on a detailed and unified cost model that is being defined in WP2 and will be presented in the next deliverable D2.3.

The insights and results from this report can significantly impact future projects in several ways:

1. **Informed Decision-Making**: The techno-economic evaluations provide a clear understanding of the cost and operational benefits of the new technologies. This helps stakeholders make informed decisions about adopting these technologies in future developments (e.g., HW or SW products for vendors, network upgrades and new deployments for operators).
2. **Improved Efficiency**: The initial results related to complexity, number of devices, and energy consumption benefits can guide the design and implementation of more efficient systems.
3. **Strategic Planning**: The planned activities and ongoing evaluations offer a roadmap for future research and development efforts. This ensures that future projects can build on the progress made in the SEASON project.
4. **Cost Model**: The development of an up-to-date cost model will provide a framework for analyzing CAPEX and OPEX, enabling more accurate budgeting and financial planning.
5. **Scalability and Innovation**: The detailed objectives and activities outlined in the report highlight innovative solutions and scalable network infrastructures that can be applied to future projects, enhancing their overall effectiveness and sustainability.

In the next deliverable, we will explain how, in light of the final results of the technical and economic analyses, the technological and architectural innovations proposed by the SEASON project will impact each of the 5 points listed above.

By leveraging the findings and methodologies from this report, future projects can achieve greater success and contribute to the advancement of technology in the field.

Dissemination Level	SEN (Sensitive - limited under the conditions of the Grant Agreement)

TABLE OF CONTENTS

1 INTRODUCTION

The deliverable D2.2 is the second deliverable of WP2 and the first of a series of two (the second and final will be D2.3 scheduled for month M32) that reports the results of the technical and economic studies carried out in the SEASON project. The inputs that support the works reported in this deliverable are the ones developed in WP2 and reported in deliverable D2.1 (Network architecture and service use cases, [SeaD2.1]) and the activities carried out in WP3 and WP4 in which the solutions for the data plane (MBoSDM, packet-optical and P2MP systems and subsystems) and for the control plane, monitoring and telemetry aspects are developed.

The organization in chapters of the deliverable is as follows. Chapter 2 reports a summary of key performance indicators (KPIs) covered by techno-economic studies carried on in WP2 with their degree of achievement. Its motivation is explained later in this Introduction.

Chapters 3 to 8 are those that report on performed studies and each of them is dedicated to one of the project objectives that potentially has implications on techno-economic aspects. In fact, all the project objectives excluding objectives Obj. 1, which is comprehensive project objective based on the achievement of the other specific objectives, Obj. 7, which concerns exclusively technical aspects, and Obj. 9, which addresses the impact on standardization, dissemination and promotion of good practices, have impact on techno-economic aspect.

As the approach in conceiving and presenting studies on techno-economics is made by project Objectives and more precisely on the related KPIs, Chapter 2 was introduced with the aim to summarize the KPIs taken into consideration. KPIs are reported with their degree of achievement having as a reference and source the studies reported in detail in chapters from 3 to 8. It is noted that the selected KPIs are a part of all the project KPIs, those that are relevant to technical and economic aspects. Furthermore, among the selected KPIs, a distinction has been made between those that are "**mandatory**", i.e., those that directly express an economic requirement (such as, for instance, a CAPEX saving), and those which express some technical requirement or target that could have an implication on economic aspects, even if not direct. This second type of KPIs are defined as "**additional**".

In chapters from 3 to 8 the deliverable studies are presented at different levels of advancement. Many studies have already produced preliminary results and in a few cases even advanced ones. Some other studies are still in progress and for them the reference scenario is presented and indications about the assumptions and expected results are outlined, while the publication of the results are postponed to the next deliverable D2.3 mentioned above. Each study is developed in four stages: (1) the ideation; (2) the development of the model; (3) the first results; and the (4) final results. In this Deliverable, studies that may have reached one of the four stages mentioned above will be documented, while in the final deliverable D2.3 they must all be at stage (4)., that of the final results.

From a methodological point of view, the approach to the studies in chapters 3 to 8 is as follows.

Within each study and associated KPI, a “baseline” solution is identified: it uses state-of-the-art technologies or their simple upgrades and is used as a reference for technical-economic comparison. An “innovative” solution which includes and uses a system or a technology among those proposed by the SEASON project is then identified as well. For example, a network solution that uses only C-band systems, the one that constitutes the “baseline”, is compared with a solution that uses multi-band systems and SDM (based on the prototypes developed in WP3), which constitutes the innovative solution. The two solutions, baseline and innovative, are then compared from the point of view of cost under the assumption that they must provide the same performance and the same capacity or load. The comparison can also take place between one or more baseline-type solutions and one or more innovative solutions, depending on the approach given to the specific study.

Chapter 9 includes the conclusions and summarizes the results obtained by taking stock of the level of satisfaction of the KPIs. It is also reported what is left to the next deliverable D2.3 to complete the work on the technical-economic evaluations within WP2.

2 KPI VALIDATION

In this chapter the KPIs considered in WP2 are presented. For each KPI the statement (as defined in the project proposal), the classification given in relation to the technical-economic aspects (*mandatory* or *additional*), the degree of achievement at the end of the second year of the project and a brief description of the activities carried out or in progress in relation to the KPI are provided.

2.1 KPI 2.2

KPI 2.2: *"50% CAPEX reduction by (1) designing an architecture that jointly leverages on parallel fibers (where fiber resources are abundant), multiple bands (where fiber resources are scares), and multi-core fibers (where fibers are not present, e.g., for cell densification); (2) limiting intermediate aggregation in routers thanks to the ultra-high capacity of MBoSDM and by exploiting smart coherent pluggable to remove aggregation layers and unnecessary O/E/O conversions."*

This KPI is classified as **mandatory**.

Status: Partially achieved, additional studies and cost model are in progress to finalize the validation.

Chapter 3 presents some techno-economic evaluations of several technologies developed to reduce the CAPEX of future MBoSDM transmission systems (some are presented in this document and others are described in more detail in deliverable D3.2 [SeaD3.2]) and are therefore related to KPI 2.2.

Several preliminary results are presented regarding the complexity and number of components of optical transmission systems and serve as basis for a more complete CAPEX and OPEX analysis in the future (to be presented in deliverable 2.3), after the definition of a cost model. These preliminary results include a multi-objective optimization algorithm capable of controlling the number of Raman amplifiers while maximizing the performance of optical systems and results showing the benefits of fiber core switching by analyzing the complexity and number of components of three node architectures presented in deliverable 3.2 [SeaD3.2] (depending on number of cores that are directly switched, the number of WSSs may be reduced by more than 50%). Other preliminary results focus on strategies to improve the robustness of existing optical networks such as optimizing filterless horseshoe networks considering the robustness against uncertainties and variations in the link parameters; or using smart RAN operation, focusing on how such operation will impact the autonomous operation of a fixed network.

Other CAPEX-reduction techno-economic studies are planned to be performed in the next months and be presented in deliverable 2.3. These include a study on the benefits of open coherent pluggables in MBoSDM architectures and of operating filterless horseshoe networks with reduced margin.

2.2 KPI 3.1

KPI 3.1: *"Design and implement flexible and modular MBoSDM node prototypes able to switch/add/drop channels in at least 3 different bands (e.g., S, C, L) in an SDM/MCF fiber infrastructure featuring up to 10 fibers/cores, able to cope with switching capacities scalable up to between 2.4-3.6 Pb/s (considering a 4-degree node with 50% local add/drop and depending on the number of used bands and SDM cores/fibers) [SRIA, mid-term evo ~2028], by approaching (fractional) space-wavelength flexible architectures."*

This KPI is classified as **additional**.

Status: Partially achieved.

Section 4.1 offers a preliminary techno-economic investigation into ultra-high-capacity MBoSDM optical networks, focusing on a fundamental comparison of multi-core fiber (MCF) and bundled multi-fiber pair (BuMFP) architectures. A detailed physical layer analysis is presented, evaluating the performance of various MCF types (with differing cladding diameters, core pitches, and loss coefficients) under varying conditions. This physical layer incorporates a comprehensive model for inter-core crosstalk (ICXT) and nonlinear impairments (NLIs), including the Kerr effect and inter-channel stimulated Raman scattering (ISRS), which are crucial considerations for accurate techno-economic analysis of MBoSDM systems. Simulation results indicate that, under specific conditions of ultra-low loss and ICXT, the throughput of MCF-based systems can be up to 14% higher than that of BuMFP-based systems. However, increasing core counts beyond a certain point (e.g., with non-standard cladding diameters below 230 µm) leads to degraded MCF performance. In scenarios with 19 multi-fiber pairs, BuMFP-based BSDM outperforms 19-core MCF-based systems, increasing throughput by 55% to 73% depending on network size. This fundamental study highlights the trade-offs between MCF and BuMFP approaches for various network scales and topologies; however, a full techno-economic assessment, including CAPEX and OPEX, is required and will be presented in deliverable 2.3.

2.3 KPI 3.2

KPI 3.2: *"MBoSDM transceivers able to increase the capacity of SoA transceivers up to 2× - 4× by exploiting enhanced wavelength/space dimensions while enabling appropriate slice/band/core/fiber selection according to the network path."*

This KPI is classified as **additional**.

Status: Partially achieved.

Section 4.2 investigates resource allocation strategies for multi-band over space-division multiplexing (SDM) optical networks, focusing on the impact of inter-core crosstalk and nonlinear impairments. A novel algorithm (XT-NLI-A-RSA) is developed, using pre-calculated physical layer parameters (GSNR, modulation formats, bandwidth) to meet quality-of-transmission (QoT) requirements. This algorithm uses a two-stage approach: a single-chunk allocation attempt followed by sliced allocation if the first fails. Simulations, using a Python-based SD-EON controller and the US Backbone network topology, compare multi-core fiber and

bundled multi-fiber pair architectures across core counts (4, 7, 13, 19) and band configurations (C, L, S bands). Key performance indicators include blocking probability and modulation format usage. Results reveal that MCF configurations, on average, reduce blocking probability by over 67% compared to BuMFPs across various traffic loads. For 4-core MCFs, the C-band consistently supports higher modulation formats (e.g., up to 64-QAM) compared to the L- and S-bands. The band priority, i.e., BSC approach, on average, reduces blocking probability by approximately 10% compared to the core priority, i.e., CSB approach across different traffic loads. However, as the core count increases (especially above 13), the performance advantage of MCFs diminishes due to increased ICXT. The study lacks a detailed cost analysis (CAPEX and OPEX), that will be presented in deliverable 2.3.

2.4 KPI 4.2

KPI 4.2: *">50% contribution in energy saving via dynamic spatial channels aggregation and deactivation of unused transceivers at the OLT side basing on traffic conditions over total 70% energy saving targeted by [SRIA]."*

This KPI is classified as ***mandatory***.

Status: Partially Achieved, additional studies are in progress to finalize the validation.

The dynamic spatial aggregation architecture developed in SEASON achieves significant energy efficiency improvements by dynamically activating and deactivating spatial lanes in response to real-time traffic demands. As presented in Section 5.1, this approach minimizes power consumption by consolidating low-load traffic onto fewer active OLT ports during off-peak hours while maintaining full operational capacity during peak periods to ensure throughput. Simulation results indicate energy savings between 2% and 38%, depending on the ratio of fixed to variable power consumption and the configuration of spatial lanes. Traffic patterns such as those from Small Office/Home Office (SOHO) scenarios achieve the highest deactivation rates, up to 40%, showcasing the architecture's adaptability to varying demands. Further optimization opportunities include the integration of real-time traffic monitoring and advanced algorithms for ONU handovers. These enhancements aim to maximize the system's energy-saving potential while maintaining high performance, ensuring scalability for next-generation energy-efficient optical networks.

2.5 KPI 4.3

KPI 4.3: "400Gb/s RAN fronthaul ports capacity."

This KPI is classified as ***additional***.

Status: Partially achieved, additional studies and cost model are in progress to finalize the validation.

Section 5.3 outlines the internal structure of the Optical Line System (OLS), highlighting its use of direct, non-selective splitting and the flexibility offered by pluggable EDFAs. This design allows for the dynamic addition or removal of channels, enhancing adaptability and scalability to meet various network demands, with a focus on increasing the capacity of the fronthaul network through 400 Gb/s ports. The system supports oversubscription by managing wavelengths through transceiver laser tuning, enabling more transmitters to connect to a single receiver than with static capacity assignments. The scheme's effectiveness is evaluated in terms of its ability to handle high-speed data transfer, maintain signal strength, and offer flexible wavelength allocation. The open-ring topology with logical full mesh interconnection is analyzed to optimize these high-capacity requirements. Future efforts will focus on quantifying the capacity enhancements and performance benefits achieved with the implementation of 400 Gb/s ports.

2.6 KPI 6.1

KPI 6.1: "*40% CAPEX reduction by collapsing computing, IP networking, and usage of high-speed coherent optical transmission in a single element (i.e., DPU) not designed for the Telecom market but for much wider computing markets and verticals (e.g., automotive).*"

This KPI is classified as ***mandatory***.

Status: Not achieved, a study and the related cost model are in progress to allow the validation.

Chapter 6 includes the description of a study setting regarding a railways 6G coverage use case as additional geotype to the ones defined in D2.1 with the aim to evaluate architectures for the RAN. Such novel architectures rely on DPUs for network layers integration and on P2MP DSCM pluggable transceiver modules for X-haul networking. The purpose of the use case is to compare a baseline scenario employing equipment typical of the legacy (traditional RAN and specialized equipment for optical, packet and compute functions) with innovative solutions as the one enabled by Open-RAN in combination with DPU cards and P2MP DSCM transceivers. The aim of the ongoing analysis the results of which are expected to be published on D2.3 is to analyze under which conditions a 40% reduction in CAPEX can be achieved due to the collapse of optical transport, packet switching and computation capabilities, as required by KPI 6.1.

2.7 KPI 6.2

KPI 6.2: "*>40% reduction of O/E/O conversions in edge-edge and edge-cloud communications by developing smart edges with high-speed coherent intelligent pluggables and by moving 5G functions closer to the cell sites. [SRIA, short/mid-term evo].*"

This KPI is classified as ***mandatory***.

Status: Not achieved, a study and the related cost model are in progress to allow the validation.

The study proposed to validate this KPI is the same of the one set for KPI 6.1 and is described in Chapter 6. For the specific purpose the analysis will be carried out in terms of benefit achievable

with an optical bypass from Far Edge to the Cloud for those traffic flows that do not need to be processed at intermediate sites (this can imply to move the 5/6G functions towards the fare edge, at least for a subset of slices). This bypass and the consequent reduction of O/E/O conversions is possible for example with coherent optics of the P2MP DSCM type given their long reach (200 km and beyond) and networking capabilities. The comparison will be carried out with a baseline solution that uses the typical legacy paradigm based on traditional RAN and with processing of traffic at packet layer performed at the border of each network segment (between far edge and edge, between edge and cloud).

The aim of the ongoing analysis is to analyze under which conditions a 40% reduction in O/E/O can be achieved due to the architecture and technology innovations introduced, as required by KPI 6.2.

2.8 KPI 7.1

KPI 7.1: *"Intelligent data aggregation to provide data compression ratio >90% without significant information loss."*

This KPI is classified as ***additional***.

Status: Achieved.

In Section 7.1, telemetry data compression results that are achieved by the different intelligent data aggregation techniques developed within SEASON project are summarized. Those techniques have been included as part of the distributed telemetry system developed and assessed within WP4/WP5 activities. The techniques are specifically designed for the measurements of larger size, i.e., optical spectrum and IQ constellations, and consist in supervised feature extraction, data compression, and data summarization. Results using openly available datasets show that Intelligent data aggregation provide data compression ratio >90% without significant information loss. In fact, by combining compression and summarization, up to 3 orders of magnitude of data reduction can be achieved compared with baseline telemetry.

2.9 KPI 8.1

KPI 8.1: "*Autonomous operation based on multi-agent systems to reduce >25% OPEX w.r.t. manual/static operation."*

This KPI is classified as ***mandatory***.

Status: Partially achieved, additional studies and cost model are in progress to finalize the validation.

Section 8.1 presents several methods based on multi-agent systems to control point-to-multipoint DSCM-based connections, i.e., to activate/deactivate SCs in order to dynamically adapt the capacity to traffic needs. Moreover, this dynamicity allows deploying systems with

oversubscription, which allows supporting more Txs on a same Rx than a simple static capacity assignment. The different methods are evaluated in terms of effective oversubscription and number of active subcarriers for different traffic scenarios. The latter can be reduced up to 50%, which is a promising value towards the target KPI (Autonomous operation based on multi-agent systems to reduce >25% OPEX w.r.t. manual/static operation). Indeed, we plan to translate these results into OPEX reduction evaluation in D2.3, to quantify the energy consumption savings of both dynamic DSCM allocation and oversubscription, compared to fixed and statically planned operation.

Besides dynamically configuring DSCM-based optical connections, optimizing EDFAs power has been identified as a promising way to minimize energy consumption. In Section 8.2, an optical line system (OLS) automatic setup approach for Access/Aggregation/Metro networks is presented. This method is based on dynamically configuring EDFASs in constant power mode, which is often preferred because it allows direct control over the power levels of each wavelength. The main drawback of this operation mode is that it necessitates precise, real-time knowledge of the number of channels entering the amplifier. A way to efficiently and practically implement automation based on monitoring to achieve constant power mode setup is to use OLCs. The solution relies on the traffic matrix and the network's topology. It begins with an approximate estimate of the span loss, which serves as the initial basis for determining the optimal gain. Additionally, it requires measurements of the received power for all channels at every point where they are added or dropped, using the power monitors available on transceivers. This approach estimates the optimal gain for each amplifier in the network to minimize the difference between the actual and target receiver power for all channels at any drop node. It also ensures that all channels remain within the receiver's acceptable range, with a specified margin. With this method, network operators can achieve a more accurate and automated calibration of amplifier gains, enhancing overall network performance and reliability. This approach reduces the need for manual intervention and allows the network to dynamically adapt to changing conditions, ensuring optimal performance across various network segments.

2.10 KPI 8.3

KPI 8.3: *"Optical layer digital twin for gradual soft-failure detection and localization with at least 1min before major impact on the service. >90% accuracy in soft-failure identification."*

This KPI is classified as ***additional***.

Status: Achieved.

In Section 8.3, several methods for soft-failure management are introduced and its performance presented. The methods are deployed within the OCATA optical digital twin, mainly designed and assessed in WP4/WP5 activities. The results presented in this document illustrate the performance of models and algorithms that exploit IQ constellation features analysis for soft-failure detection, identification, and severity estimation. Considering challenging scenarios where an incipient soft-failure becomes hard failure in the short period of 1 day, different

failures affecting Tx, EDFAs, and WSS are promptly detected (>40 min before hard failure) and localized/identified (>18 min before hard failure). With these results, the target objectives of the KPI (*Optical layer digital twin for gradual soft-failure detection and localization with at least 1min before major impact on the service. >90% accuracy in soft-failure identification*) are clearly achieved.

3 MBoSDM Network Infrastructure from Access to Cloud

3.1 Raman Amplification and Launch Power Optimization in MB Optical Systems

Multi-band transmission systems enhance the data-carrying capacity of optical networks. While spatial-division multiplexing (SDM) is often considered the most future-proof solution for increasing optical network capacity [Win23], there are valuable alternatives. We can broaden the available transmission spectrum by incorporating the longer (L-) and shorter (S-) transmission bands alongside the traditional C-band. It is important to note that multi-band transmission (MBT) and SDM are not mutually exclusive approaches [Nap18]. In future optical networks, MBT will likely optimize transmission capacity per fiber, core, or mode, seamlessly complementing SDM to meet the ever-growing demand for capacity.

Commercial systems already incorporate the L-band, potentially doubling the total system capacity. Researchers actively explore systems with even wider bandwidth, focusing on devices compatible with transmission bands beyond the C- and L-bands. Leveraging the S-band, which shares similar fiber characteristics with the C- and L-bands, holds promise. Numerous studies have already shown the additional capacity made available by integrating the S-band into a C+L-band system [Sem20, Cor21, Ham19].

Optimizing the launch power is crucial for maximizing the capacity of MBT systems. For instance, fine-tuning the average power and power tilt of transmitted channels in a 15-THz S+C+L MBT system enabled improving the generalized signal-to-noise ratio (GSNR) between 0.6 dB to 1.6 dB [Sou22]. However, this optimization task is far from trivial due to several factors. It depends on the stimulated Raman scattering (SRS) effect, which cannot be neglected in MBT systems, the frequency-dependent characteristic of fiber parameters, and the unique features of band-specific devices such as optical amplifiers. Moreover, optimizing the launch power is a nonlinear problem. Recent publications have explored launch power optimization in MBT systems using methods such as explicit enumeration [Vir21, Sad21], iterative algorithms [Ham19, Sou22], or genetic algorithms (GA) [Cor21, Bug21].

Even after proper launch power optimization, performance in the S-band is still worse than in the other two bands. This performance disparity primarily results from power transfer to the C- and L-bands, driven by the SRS effect. Additionally, higher fiber losses and potentially higher noise figures (NF) in S-band amplifiers contribute to the optical performance imbalance across transmission bands. Recent research indicates that selective Raman amplification can enhance S-band performance, bringing it closer to the levels observed in the C- and L-bands. This improvement simplifies service provisioning in optical networks that utilize MBT [Ham19]. However, optimizing Raman pumps remains challenging due to the nonlinear nature of the SRS effect. Various approaches have been proposed to tackle this issue. For instance, Yankov et al. [Yan23] trained separate neural networks (NNs) to predict the Raman gain for forward- and

backwards-propagating pumps, respectively. Then, they optimized the system using a gradient descent algorithm. It is worth noting that this approach relies on the accuracy of the NNs, and their training process may not be straightforward. Furthermore, dedicated NN models are necessary for each specific scenario [Mou21].

Various single-objective evolutionary algorithms have been employed in this context. Among them, the Genetic Algorithm (GA) is one of the most popular choices for ensuring gain-flatness performance and bandwidth optimization in multi-pump Raman amplifiers [Per02, Liu04]. Researchers have also proposed enhancements to the traditional GA, such as the hybrid-GA (HGA) optimization procedure [Liu04-2, Fer11]. Additionally, Jiang et al. introduced the Ant Colony optimization [Jia11] and the Artificial Fish School Algorithm [Jia11-2] to find optimal pump parameters, offering alternatives for designing gain-flattened Raman Fiber Amplifiers (RFAs). Another search method used in RFA design is Particle Swarm optimization, known for its fast convergence and improved computational efficiency [Jia12]. While previous studies often tackled the Raman amplifier design and launch power optimization separately, this work proposes a framework that simultaneously optimizes the launch power and the Raman pumps in MBT systems using a multi-objective GA approach.

We propose an innovative optimization framework using a multi-objective genetic algorithm to simultaneously optimize the launch power profile and design the Raman amplifiers. Its flexibility allows us to find better solutions and reduce the number of Raman pumps (therefore controlling the overall system cost). Moreover, we utilize the framework to compare the potential of four multi-band transmission systems leveraging hybrid fiber amplification. The work is organized as follows. The multi-objective optimization algorithm is described in Section 3.1.1. Section 3.1.2 details the optimization setup and the networks used to obtain the results presented in this work. Afterward, Section 3.1.3 presents and discusses the results and practical considerations when applying the algorithm to commercial networks.

3.1.1 Optimization Framework Description

This work uses the per-channel GSNR as the quality of transmission (QoT) estimator (considering the signal bandwidth as a reference). This QoT metric is given by Eq. 1, where P_i is the power of channel i and P_i^{ASE} and P_i^{NLI} are the power of the Gaussian noise corresponding to the amplified spontaneous emission (ASE) noise and the nonlinear interference due to the self- and cross-channel nonlinear crosstalk at channel i, respectively.

$$GSNR_i = \frac{P_i}{P_i^{ASE} + P_i^{NLI}} \quad \text{Eq. 1}$$

The optimization algorithm aims to maximize the sum of the channels GSNR ($GSNR_{sum}$) and minimize the sum of the per-band GSNR variation ($\Delta\mathrm{GSNR}^b$) of a MBT system considering hybrid amplification. $\Delta\mathrm{GSNR}^b$ is given by the difference between the best and the worst GSNR considering all channels in transmission band b. Figure 3.1-1 depicts a representation of the

optimization variables for a transmission system with three amplification bands and three Raman pumps. The proposed framework optimizes the average channel power (P_b) [dBm] and power tilt (T_b) [dBm/THz] of each band, as well as the pump powers P_p^j. The algorithm considers that the candidate pumps have fixed frequencies (f_p^j).

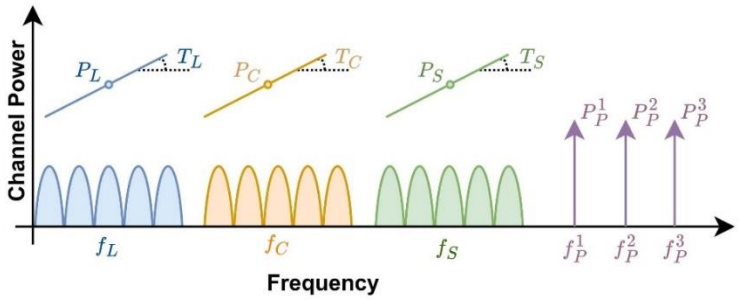

Figure 3.1-1 Representation of optimization variables.

There are two general approaches to multiple-objective optimization. One is to combine the individual objective functions into a single composite function or move all but one objective to the constraint set. The second general approach is to determine an entire Pareto optimal solution set or a representative subset. The concept of a Pareto set of optimal solutions stands for a set of solutions that are non-dominated by each other but are superior to the rest of the solutions in the search space. A solution is called non-dominated if none of the objective functions can be improved in value without degrading some other objective values. Pareto optimal solution sets are often preferred to single solutions because, when considering real-life deployments, the final solution can involve a trade-off [Kon06]. Therefore, we select the Non-dominated Sorting Genetic Algorithm (NSGA-II) multi-objective GA to solve the optimization problem due to its good level of convergence to the true Pareto Front and diversity [Deb02] (the Python library Pymoo [Bla20] was used).

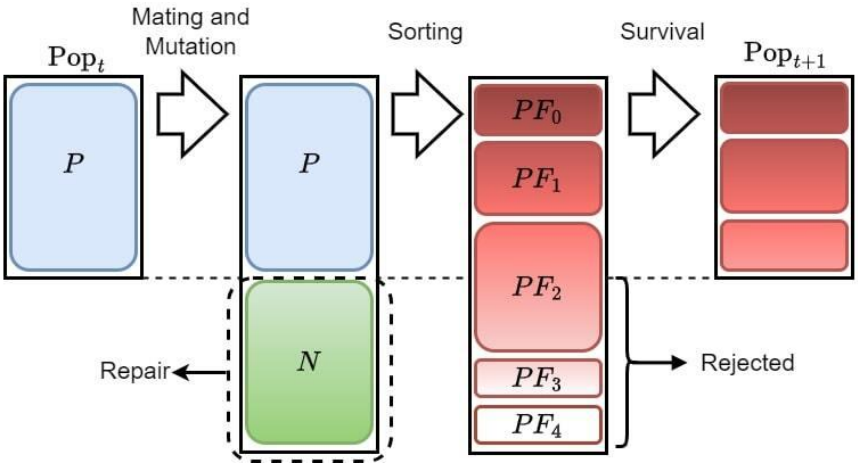

Figure 3.1-2 Multi objective genetic algorithm framework.

Figure 3.1-2 presents the algorithm workflow. The algorithm starts from an initial population of P individuals randomly generated from a uniform distribution. Each individual's chromosomes represent P_b, T_b and P_p^j (float values). Before evaluating each individual's fitness, a repair function [Bla20] guarantees that the sum of the pump powers is smaller than a given value (P_P^{TOT}) for all generated individuals by normalizing the pumps powers if the total pump power is greater than P_P^{TOT}. Afterwards, the fitness of the individuals is evaluated according to Eq. 2 and Eq. 3, where $\mathrm{GSNR_i}$ is the GSNR of channel i and $C(\cdot)$ is the ideal Shannon capacity of channel i, given by Eq. 4 [Pog14], where R_S is the channel baud rate, $\mathcal{B}$ and $\mathcal{C}$ are the sets of amplification bands and channels, N_P^{MAX} is the maximum number of Raman pumps allowed, p is the penalty for every Raman pump exceeding N_P^{MAX}.

$$F_1 = \sum_{i \in \mathcal{C}} C\left(\mathrm{GSNR_i} - p \cdot \min\left(0, N_P - N_P^{MAX}\right)\right) \quad \text{Eq. 2}$$

$$F_2 = \sum_{b \in \mathcal{B}} \left[\Delta GSNR^b + p \cdot \min\left(0, N_P - N_P^{MAX}\right)\right] \quad \text{Eq. 3}$$

$$C(\mathrm{GSNR_i}) = 2 \cdot R_S \cdot log_2(1 + \mathrm{GSNR_i}) \quad \text{Eq. 4}$$

The algorithm aims to maximize F_1 and minimise F_2. Notice that these objectives are concurrent since the highest capacity of a given transmission system is achieved for a given value of GSNR variation [Jia24, Guo24], and some system capacity must be sacrificed to equalize the GSNR further. When evaluating the GSNR, the algorithm only considers pumps with powers higher than a certain threshold (P_P^{TH}).

Next, the offspring of the current population is generated via mating and mutation (N individuals). The same repair function used in the initial population corrects the offspring's chromosomes, and the algorithm calculates their fitness. Afterward, all individuals are sorted in Pareto fronts (PF_i) and according to the crowding distance. The P best individuals survive and are used for the next generation while all others are eliminated.

The value of the penalty (p) may change during the algorithm operation. For example, it may be set to zero for the initial generations. Hence, with an unbiased evaluation, the algorithm searches the entire solution space in the initial phase. It may be set to a different value afterward, so the algorithm evolves towards solutions requiring fewer pumps. We chose to implement the penalization of the number of pumps exceeding N_P^{MAX} as a GSNR penalty for simplicity of the analysis. This way, having the same p value for both fitness functions independently of the transmission system is possible. For example, if we apply a fixed penalty value outside the summation in F_1 instead of inside $C(\cdot)$, it will have different effects in transmission systems with different numbers of channels (higher penalization in systems with lower channel count/total capacity and lower penalization in systems with higher channel count/total capacity). The same effect happens for F_2, but the difference applies to systems with

different numbers of transmission bands. Additionally, F_1 and F_2 would require different p values because of the magnitude difference between the total capacity and the sum of $\Delta GSNR^b$.

Different fitness functions (F_i) may be defined if other optimization objectives are considered more important. For example, if a flat GSNR profile is desired across the entire transmission window instead of a per-band flatness, $\Delta GSNR^b$ may be switched to $\Delta GSNR$ in the fitness function F_2, where $\Delta GSNR$ is given by the difference of the best and the worst GSNR of all transmitted channels (similarly to what we did in [Sou24]). Another possible development of the optimization framework is to include the number of Raman pumps as an objective to be minimized. For example, a third objective may be included with $F_3 = N_P$ and p set to zero in F_1 and F_2. This way, the algorithm finds the Pareto front representing the trade-off between the highest capacity, lowest per-band GSNR variation and lowest number of pumps. However, this solution involves including an additional objective. It could lead to higher convergence times and poorer optimization performance (other evolutionary algorithms, such as the NSGA-III [Deb:14], may perform better than the NSGA-II in this case). Therefore, one should keep in mind the convergence and practicality of the fitness functions; F_1 and F_2 are good examples of fitness functions in the sense that they allow for a good convergence performance while also allowing for the limitation of the number of Raman pumps used. This enables the analysis of the trade-off between the number of pumps, system capacity and per-band GSNR flatness.

3.1.2 Simulation Setup

To give a glimpse of the optimization algorithm's utilization and give examples of its usefulness, we evaluate the performance of an MBT system in the Spanish national reference network, as defined by Telefónica in the IDEALIST project [Sou22-2] (Figure 3.1-3(a)), considering, for simplicity, a fully loaded spectrum and that all spans are 80 km long. The number of 80-km spans in each link is given by $\lceil L\_l/80 \rceil$, where L_l is the link length in kilometres and $\lceil \cdot \rceil$ is the ceiling operator. The Spanish national network has 30 nodes and 435 shortest paths between nodes, with an average length of 834 km and an average link length of 261 km.

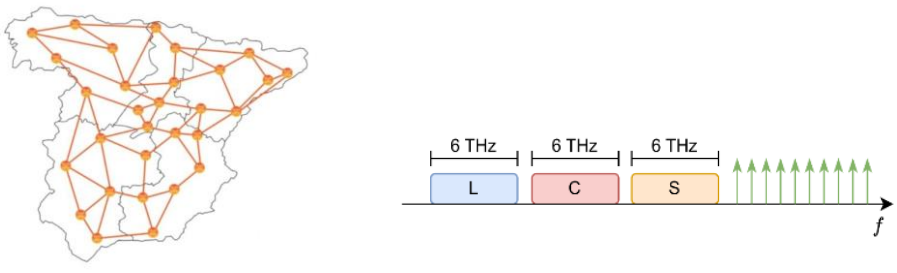

Figure 3.1-3 (a) Telefónica national reference network diagram and (b) frequency spectrum of the S+C+L -band MBT system.

Dissemination Level	SEN (Sensitive - limited under the conditions of the Grant Agreement)

The optical fiber is modelled by a nonlinear coefficient of 1.27 W^{-1}/km, a dispersion parameter of 16.8 ps/nm/km, and a dispersion slope of 0.058 ps/nm^2/km at 1550 nm. The frequency-dependent loss and nonlinearity coefficients and the normalized Raman gain profile of the optical fiber are shown in Figure 3.1-4. Additionally, input and output connector losses of 0.25 dB and splice losses of 0.01 dB/km are assumed. After each fiber span, a band demultiplexer (with a 1-dB insertion loss) separates the transmitted bands and delivers them to the respective optical amplifier. We consider a band demultiplexer based on a band filter and assume its insertion loss will be slightly higher than current commercial C+L-band filters [OFLink]. The lumped optical amplifiers are modelled by a constant noise figure of [6, 6, 7] dB for the L-, C-, and S-bands for gain values larger than 20 dB. For gain values smaller than 14 dB, the amplifiers' NF is 2 dB higher. The NF is linearly interpolated for gain values ranging between 14 and 20 dB. Their gain compensates for the loss of each channel, considering the impact of the SRS effect and the gain already provided by the Raman amplifiers. The power evolution of the signals and pumps across the fiber is calculated by numerically solving the Raman differential equations (using the solver available in GNPy [OOPT-PSE]). Subsequently, the transmitted bands are recombined by an optical coupler (with a 0.5 dB insertion loss).

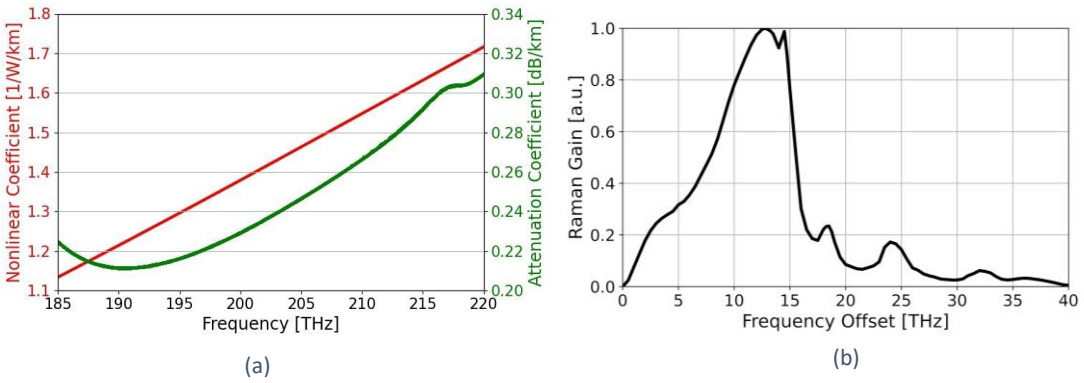

Figure 3.1-4 (a) Frequency-dependent fiber loss and nonlinear coefficient. (b) Normalized Raman gain profile.

We consider the transmission of 120-GBd (R_S) signals in a 150-GHz spectral grid (40 channels per band). Figure 3.1-3(b) shows the S+C+L-band MBT system considered in this work. It employs up to 10 counter-propagating Raman pumps with 1 THz spacing and a minimum guard band of 500 GHz between adjacent bands. We have channels from 184.5 THz to 203.5 THz and pumps from 205 THz to 214 THz. The Raman amplifier is assumed to add an equal amount of noise on both polarizations.

The multi-objective genetic algorithm optimizes the power of the channels and the pumps. The initial population size of the GA is 120, and 60 offspring are generated at each generation, $P_P^{TH} = 50$ mW and $P_P^{TOT} = 1$ W. The algorithm ran until convergence of the hypervolume performance metric [Bla20]. The number and frequencies of the Raman pumps and the maximum total pump power values are selected here just to illustrate the algorithm's utilization. These values correspond to a good trade-off between execution time and capacity of GSNR flattening. Note that an arbitrary number of pumps and pump frequencies can be defined, and the algorithm will

converge to the optimal maximum total pump power and distribution of the available power among the pumps.

After optimization, we evaluate the number of feasible lightpaths and the network-wide average system capacity [Clo16] in the Spanish national network. The five different bit rates considered in this work and their required OSNR and SNR are presented in Table 3.1-1. These values were taken from the OpenRoadm agreement [OpenROADM] for 200 Gb/s, 300 Gb/s and 400 Gb/s formats and scaled up from 64 GBd to 120 GBd to represent a near future optical MBT system (500 Gb/s and 700 Gb/s values were linearly interpolated). The SNR_{req} values are directly calculated from the $OSNR_{req}$ values using the relation given in [Ess12], i.e., $SNR_{req} = OSNR_{req} - 10\log_{10}(R_S/B_{ref})$, with B_{ref} equal to 12.5 GHz.

Table 3.1-1 Required OSNR (defined in 0.1 nm) and SNR for each considered bit rate.

Bit rate [Gb/s]	400	500	600	700	800
$\mathbf{OSNR_{req}}$ [dB]	18.7	21	23.5	25	26.5
$\mathbf{SNR_{req}}$ [dB]	8.9	11.2	13.7	15.2	16.7

For each channel, the GSNR at the end of a lightpath with N spans is given by $\mathrm{GSNR_N} = GSNR - 10\log_{10}(N) - M$, where GSNR is the optimized per-channel and per-span GSNR and M is the system margin defined as $M = 2 + 0.05(N_{OLAs} + N_{ROADMs})$. This margin comprises a fixed 2 dB margin and a variable contribution that depends on the number of traversed optical amplifiers (N_{OLAs}) and ROADMs (N_{ROADMs}). Additionally, we consider a transceiver OSNR of 38 dB and add/express OSNR of 38 dB/37 dB. A lightpath is feasible for a given signal configuration if the required SNR is smaller than $\mathrm{GSNR_N}$.

The network-wide average system capacity metric is used to estimate the impact of the performance of the different transmission systems at the network level. The average system capacity is the sum of the network-wide average channel capacity [Clo16] for all transmitted channels. The average channel capacity is the value of the highest feasible bit rate of a channel, averaged for all the shortest routing paths of the network.

3.1.3 Results and Discussion

3.1.3.1 Fixed Raman Pump Penalty and Variable Pump Limit

In this section, we show how N_P^{MAX} may be used to influence the Raman pump count on the solutions and compare the performance of the proposed framework with an iterative approach based on the weighted sum method [Sou22]. The latter uses a fixed number of pumps (2 pumps) to compute results in a reasonable time frame. Following the same approach as in [Sou23], the iterative algorithm considers pump frequency separations from 1 to 8 THz in steps of 1 THz, and pump power profiles where the optical power of the highest frequency pump is 1, 2, 3 and 4

times higher than the lowest one. It also imposes a maximum total pump power of 1 W. In the GA simulations, N_P^{MAX} is set to 1, 2, 4 or 10 and $p = 2$ (to calculate F_1 and F_2).

Figure 3.1-5 shows the Pareto fronts after convergence and the solution found by the iterative algorithm in terms of the total ideal system capacity, which is obtained by the sum of $C(\mathrm{GSNR_i})$, and the average $\Delta\mathrm{GSNR^b}$ for an 80-km span. By comparing the Pareto fronts, we conclude that using higher N_P^{MAX} leads to flatter GSNR profiles for a given system capacity. However, the highest achievable total capacity remains mostly unchanged, i.e., it is only slightly dependent on N_P^{MAX}, ranging from 137.3 Tb/s for $N_P^{MAX} = 1$ to 138.8 Tb/s for $N_P^{MAX} = 10$. Note that this result is also a consequence of setting a maximum total pump power of 1 W, independently of the number of used pumps. The Pareto fronts are similar for N_P^{MAX} equal to 4 or 10. The front for $N_P^{MAX} = 2$ is close to the previous two for average $\Delta\mathrm{GSNR^b}$ values higher than 2.3 dB, but the difference becomes significant for lower per-band GSNR variation values. By reducing N_P^{MAX} to one, the solutions have higher average $\Delta\mathrm{GSNR^b}$ for the same capacity. For example, the GA with $N_P^{MAX} = 1$ achieved a minimum of $\Delta\mathrm{GSNR^b} = 0.7$ dB at a total ideal capacity of 124 Tb/s. In contrast, the same average $\Delta\mathrm{GSNR^b}$ is achieved with total ideal capacities of 131, 134 and 135 Tb/s for N_P^{MAX} equal to 2, 4 and 10, respectively.

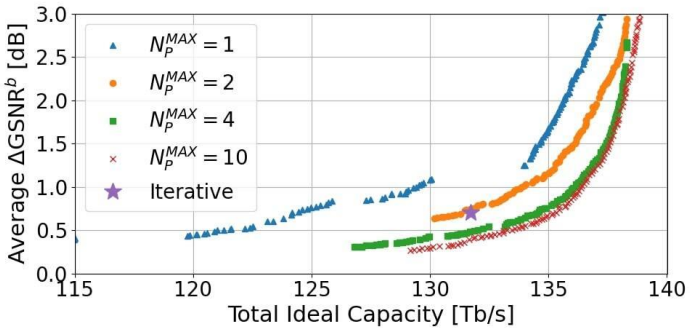

Figure 3.1-5 Non dominated solutions after convergence and best solution using the iterative algorithm.

The behavior of the Pareto fronts results from the number of Raman pumps used. To further clarify this point, Figure 3.1-6(a) and Figure 3.1-6(b) show the pump power distribution for the GA solutions for an average $\Delta\mathrm{GSNR^b}$ of 2.7 and 0.7 dB, respectively, for each value of N_P^{MAX}. For an average $\Delta\mathrm{GSNR^b}$ of 2.7 or 0.7 dB, the solutions use 1, 2, 4 and 10 pumps for N_P^{MAX} equal to 1, 2, 4 and 10, respectively. Moreover, all solutions of the Pareto fronts have a Raman pump count equal to or smaller than N_P^{MAX}. Therefore, using lower N_P^{MAX} effectively reduces the number of Raman pumps and may lead to a more cost-effective solution.

Figure 3.1-6 Raman pump power (in mW) distribution for GA solutions with an average $\Delta GSNR^b$ of (a) 2.7 dB; and (b) 0.7 dB.

For a high value of average $\Delta\mathrm{GSNR}^{\mathrm{b}}$, the GA converges to solutions that use almost all the allowed power for the Raman pumps. The sum of the pump powers shown in Figure 3.1-6(a) are 967, 997, 999 and 1000 mW for N_P^{MAX} equal to 1, 2, 4 and 10. On the other hand, the sum of the pump powers to achieve a lower GSNR variation, shown in Figure 3.1-6(b), are 213, 953, 991 and 996 mW for N_P^{MAX} equal to 1, 2, 4 and 10. Solutions with a single pump tend to have a smaller total pump power when minimizing the average $\Delta\mathrm{GSNR}^{\mathrm{b}}$ because it is harder to get a flat profile with only a small number of pumps, i.e., a single high-power Raman pump would cause a high GSNR variation within a band. On the other hand, using more pumps allows for a better distribution of the available power and a flatter GSNR profile while using a high total pump power.

Moreover, to gain more insight into the impact of using different numbers of Raman pumps, Figure 3.1-7(a) and Figure 3.1-7(b) show the optimum launch power and the corresponding GSNR profile, respectively, for the solution leading to $\Delta\mathrm{GSNR}^{\mathrm{b}} = 2.7$ dB. As expected, since the total ideal system capacity is very similar for the 4 considered cases, the launch power and, consequently, the $GSNR_i$ values are very similar regardless of the number of Raman pumps used. On the other hand, if we aim at a low average $\Delta\mathrm{GSNR}^{\mathrm{b}} = 0.7$ dB, whose corresponding results are depicted in Figure 3.1-8, the curves for N_P^{MAX} equal to 4 and 10 are very similar whereas reducing N_P^{MAX} causes a reduction in the average GSNR, particularly in the S- and C-bands. This result highlights that using more Raman pumps is an effective approach to improve the average GSNR while keeping the per-band GSNR variation reduced.

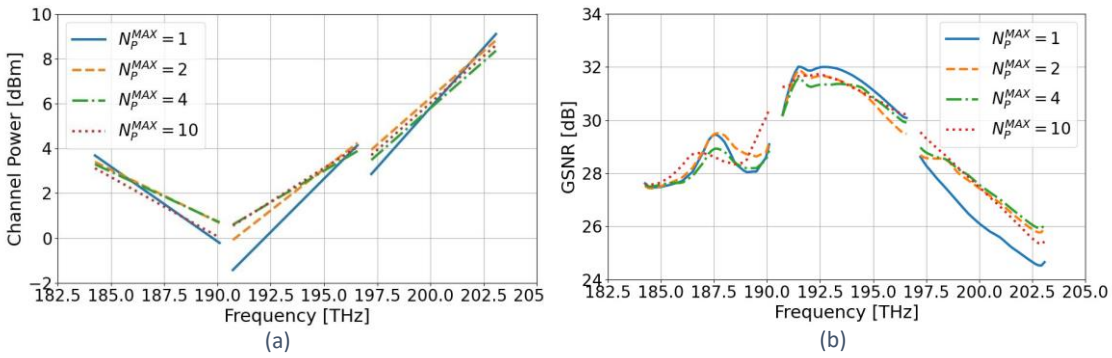

Figure 3.1-7 (a) Launch power and (b) corresponding GSNR profile for GA solutions with an average $\Delta GSNR^b$ of 2.7 dB.

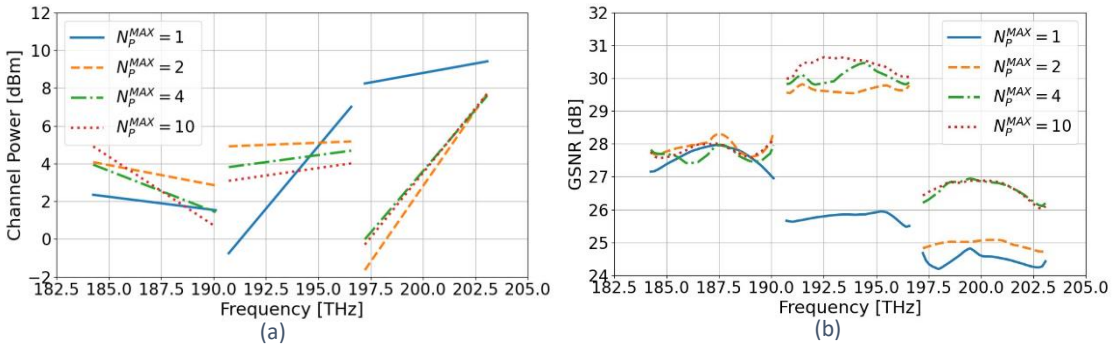

Figure 3.1-8 (a) Launch power and (b) corresponding GSNR profile for GA solutions with an average $\Delta GSNR^b$ of 0.7 dB.

Looking back at Figure 3.1-5, we see that the iterative algorithm converges to a solution similar to the Pareto front with $N_P^{MAX} = 2$. This similarity is expected since the same number of Raman pumps is used. However, the iterative algorithm only converges to a single solution. On the other hand, the proposed framework offers a broader set of solutions, e.g., with higher average GSNR (at the cost of a higher per-band GSNR variation) or smaller average $\Delta\mathrm{GSNR^b}$ (at the expense of a lower average GSNR). Moreover, the iterative algorithm also took longer to reach a solution, even with a limited set of Raman pump counts, profiles, and channels power tested. Both algorithms were implemented in Python and ran in a single 2.2-GHz core. The iterative algorithm took an average of 8 hours to run the optimization, whereas the GA only required an average of 5 hours, i.e., an average computation time reduction of 37%.

3.1.3.2 Influence of the Raman Pump Penalty Value

Because of the value of p used in the previous section ($p = 2$), all solutions of the Pareto fronts presented have a Raman pump count equal to or smaller than N_P^{MAX}. However, the algorithm may converge to solutions with more pumps than N_P^{MAX} for lower Raman pump penalty values, potentially leading to better performance results.

Figure 3.1-9(a) shows the Pareto fronts after convergence for an 80-km span for different values of p and $N_P^{MAX} = 1$. The figure shows that reducing p improves the Pareto fronts by relaxing the

requirement of using a single Raman pump. In the limit, i.e., for $p = 0$, the algorithm behaves exactly as when $N_P^{MAX} = 10$, yielding the best results.

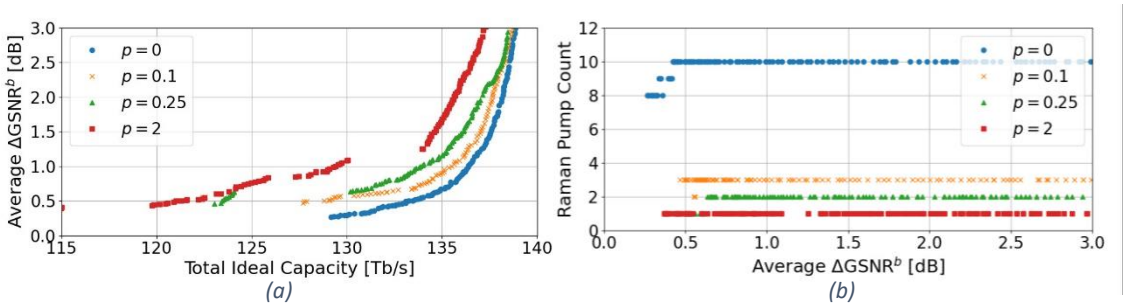

Figure 3.1-9 (a) Optimal non-dominated solutions and (b) Raman pump count as a function of the average $\Delta GSNR^b$ of solutions.

Carefully selecting the Raman pump penalty value allows obtaining solutions that perform better at the cost of having more pumps than N_P^{MAX}. Figure 3.1-9(b) shows the Raman pump count for different values of p versus the average $\Delta\mathrm{GSNR^b}$. The improvement in the system capacity observed in this case for the same average $\Delta\mathrm{GSNR^b}$ when compared with the previous results is due to using more Raman pumps. The best solutions are found when $p = 0$, i.e., when there is no restriction on the number of Raman pumps used in the solutions (up to 10 pumps may be used). For higher values of p, the solutions tend to use fewer Raman pumps and perform worse. For example, for an average $\Delta\mathrm{GSNR^b} = 0.7$ dB, the solution on the Pareto front when $p = 2$ achieves 124.5 Tb/s with a single pump. For $p = 0.25$, the total capacity increases to 131.5 Tb/s with two pumps; for $p = 0.1$, the total capacity is 133.6 Tb/s with four pumps; and for $p = 0$, the total capacity is 135.3 Tb/s with ten pumps being deployed. In summary, the Raman pump penalty p controls the algorithm's flexibility to search solutions which may not be limited to N_P^{MAX}, thus allowing to find better-performing solutions for each region of the Pareto front. However, if a strict limitation of the number of Raman pumps is desired, a high p value should be used.

3.2 Node Architectures for High-Capacity MBoSDM Optical Networks

This research explores the evolution of optical networks, and the increasing challenges associated with managing optical signal switching, particularly in multi-band over spatial division multiplexing (MBoSDM) systems. We propose three innovative node architectures, each analyzed for complexity and compared with a standard node architecture, providing valuable insights into potential future obstacles in optical networks.

Additionally, the study delves into the benefits of fiber-core switching, a technique that leverages the existence of multiple spatial paths between the same nodes. This method can potentially eliminate the need for individual channel demultiplexing/multiplexing at every network node, depending on traffic volume. The findings not only deepen our understanding of node architectures and fiber-core switching but also pave the way for more efficient and robust optical communication networks.

The architectures proposed in this work include the high-capacity node prototypes developed in SEASON project (MBoSDM node prototype and multi-granular optical node prototype describe in deliverable 3.2 [SeaD3.2]) by varying the size of the WSS. The results presented in this section are preliminary techno-economic results, showing the benefits of the proposed architectures in terms of system complexity reduction. A more complete analysis, considering equipment cost, will be performed as future work.

3.2.1 Description of the Node Architectures

The motivation for using novel MBoSDM nodes, a detailed description of the proposed nodes, as well as the reference node architecture, and an initial optical performance estimation are given in Deliverable 3.2 [SeaD3.2].

The Reference node configuration uses a single-band matrix-switch to construct an MBoSDM node [Sah17], as depicted in Figure 3.2-1(a). The node structure is presented for a single amplification band, and identical schemes are used for the other bands. This reference architecture serves as a benchmark for subsequent comparisons.

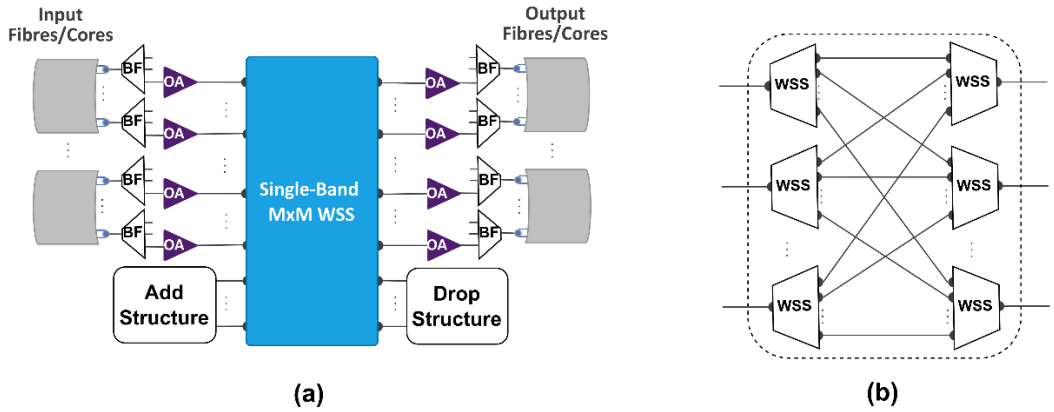

Figure 3.2-1 (a) Reference architecture: single-band matrix-switch-based MBoSDM node. The node structure is presented for a single amplification band, and identical schemes are used for the other bands. (b) Route and Select (R&S) implementation of an MxM WSS.

The three proposed architectures rely on fiber-core switching using a spatial cross-connect (S-OXC) or direct and fixed core/fiber connections (core/fiber switching) to avoid the scalability issues of the reference architecture concerning the increasing spectral and spatial dimensions. Figure 3.2-2 depicts the three architecture proposals (#1, #2 and #3).

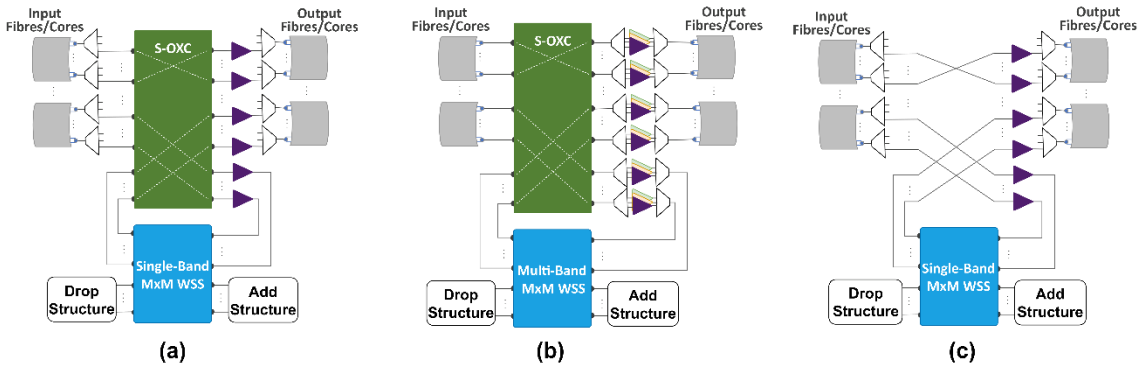

Figure 3.2-2 (a) Node architecture proposal #1: single-band matrix-switch-based MBoSDM node with a S-OXC. (b) Node architecture proposal #2: multi-band matrix-switch-based MBoSDM node with a S-OXC. (c) Node architecture proposal #3: single-band matrix-switch-based MBoSDM node without a S-OXC.

3.2.2 Ports and Components Count

The proposed architectures offer different balances between complexity, flexibility, and cost. Table 3.2-1 illustrates the component count and port requirements for the considered node architectures. For simplicity, we assume an equal number of bands per core (B) and fiber cores per degree (C). Here, D represents the nodal degree, N_C denotes the number of core pairs directly switched, and $N_{A/D}$ indicates the number of ports of the WSSs connected to the Add/Drop (A/D) structure. It is worth noting that these figures exclude the A/D structure since the same one can be employed independently of the node architecture.

Table 3.2-1 Number of components and port count for the different node architectures.

Component	**Reference Architecture**	**Architecture #1**	**Architecture #2**	**Architecture #3**
S-OXC Count	0	B	1	0
S-OXC Port Count	--	$4CD - 2N_C$		--
MxM WSS Count	B		1	B
MxM WSS Port Count	$2(CD + N_{A/D})$	$2(CD - N_C + N_{A/D})$		
Optical Amplifier Count	$2BCD$	$2BCD - N_C$		
Band Filter Count	$2CD$		$2(2CD - N_C)$	$2CD$

The analysis of Table 3.2-1 shows that each directly switched core pair saves two ports on the MxM WSS and one optical amplifier. Furthermore, the only distinction between architectures #1 and #3 lies in the absence of a S-OXC in the former. Architecture #2 shares the same number of S-OXC ports, WSS ports and optical amplifiers as the other two proposed architectures but employs only one wideband S-OXC and WSS, along with a higher number of band filters. This design capitalizes on the predicted lower complexity and cost-effectiveness of producing wideband WSSs compared to multiple lower-bandwidth components [Roo24] and the cost reduction associated with integrated amplifiers and band filters.

The MxM WSS can be realized through a Route and Select (R&S) switch configuration comprising multiple 1xM WSSs [Sah17] (see Figure 3.2-1(b)). This configuration maintains a simple two-stage structure and achieves similar performance metrics in terms of insertion loss (IL), filtering bandwidth, and crosstalk as conventional R&S WSSs, provided that high port-count WSSs exhibit comparable IL, filtering bandwidth, and crosstalk as their traditional counterparts. However, the increased number of WSS ports necessitates high-port-count WSSs and intricate control and adjustment of optical signals. Alternatively, constructing a high-port-count 1xM WSS by concatenating smaller WSSs reduces the port requirement of a single WSS but significantly increases the cost, insertion losses, optical filtering effects, and in-band crosstalk associated [Niw17].

When using traditional R&S architectures to implement the MxM WSS, a simple reduction of two ports decreases the WSS count by two. For instance, consider connecting 16 input/output (I/O) core pairs with one amplification band. The reference design requires one 16x16 WSSs and 32 optical amplifiers. Assuming a fixed WSS size of 1x20, the implementation necessitates 32 1x20 WSSs. Conversely, if one core pair is directly switched ($N_C = 1$) using one of the proposed architectures, only 30 1x20 WSSs and 31 amplifiers are required. With higher core-switching ratios, the node's complexity is progressively reduced. For instance, directly switching 10 of the 16 core pairs would necessitate 12 1x20 WSSs and 22 optical amplifiers in the same scenario. Figure 3.2-3 illustrates the evolution of WSS and optical amplifier counts for an increasing number of directly switched core pairs and various numbers of I/O core pairs.

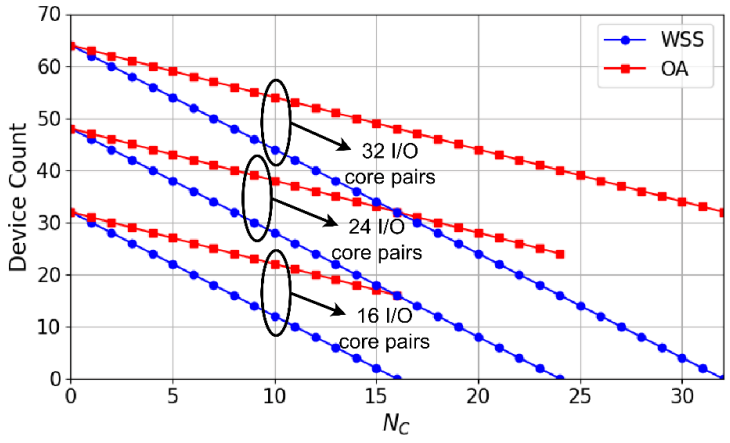

Figure 3.2-3 Evolution of WSS and optical amplifier count for an increasing number of directly switched core pairs (N_C) and different numbers of in/out core pairs.

3.3 TECHNO-ECONOMIC STUDY ON THE BENEFITS OF OPEN COHERENT PLUGGABLES IN MB OVER SDM ARCHITECTURES

3.3.1 Introduction

The continuous growth of traffic led by video streaming, cloud computing and AI applications is pushing optical network infrastructure to the adoption of new technologies. Multi-band and multi-core fiber (MB/MCF) technologies are promising solutions which can increase spectral and spatial capacity. For near-term capacity growth, multi-band has been adopted over the past few years. Although in the longer term, the combination of both MB and MCF technologies, referred to as multi-band over spatial division multiplexing (MBoSDM), will be needed [Arp24]. Within this context, there is an ongoing debate between the use of IP+WDM vs IP-over-WDM (IPoWDM) in optical metro/core networks [Mar24].

The traditional architecture of IP+WDM in metro/core networks connects IP routers to the ROADM node via transponders or an OTN switch, decoupling IP traffic from optical wavelengths. Instead, an IPoWDM architecture uses coherent pluggables to provide direct router-to-router connections, having IP routing over optical wavelengths. Nevertheless, ROADM nodes can be still needed to perform optical switching and regeneration, if pluggables have not enough optical reach (Figure 3.3-1) [Dav24]. Several factors have contributed to making IPoWDM a viable alternative. For example, the traffic evolution. Traffic has shifted to higher client speeds and increased the hub and spoke instead of any to any traffic. This change reduces the advantages of OTN and supports the adoption of IPoWDM. Additionally, advances in router silicon technology now enable capacities of hundreds of Tb/s per router [Faz23]. Coherent pluggables have reached capacities of up to 800 Gb/s and extended their maximum optical reach to thousands of kilometers [Par24].

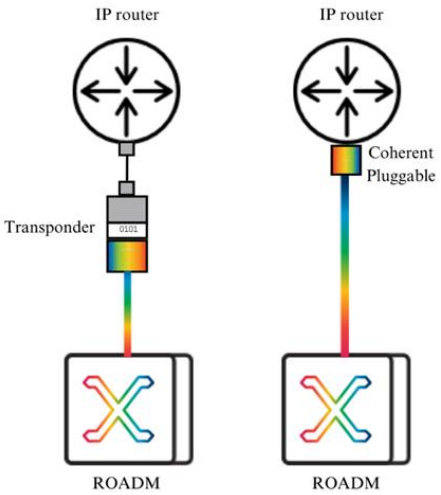

Figure 3.3-1 IP+WDM vs IPoWDM architectures.

The deployment of IP+WDM and IPoWDM in MBoSDM environments is still unexplored and introduces new challenges for network planning. In addition to spectral efficiency, factors such as energy efficiency and cost-per-bit optimization must also be considered. This study aims to perform a techno-economic comparison to provide guidelines for future network design. It will propose a network planning strategy which accounts for uncertainty in the traffic growth over multiple years.

3.3.2 State of the Art

IP+WDM and IPoWDM both have advantages and disadvantages. In the IP+WDM architecture, there is a clear demarcation between IP and optical layers, which can facilitate the operation and maintenance of the network due to fault isolation. As a drawback, the separation of these layers involves more equipment, increasing capital and operational expenditures. In the IPoWDM architecture, IP routing and optical transport are integrated into a single device, which simplifies the network design, reduces latency and lowers costs. Nevertheless, IPoWDM provides less scalability.

Coherent pluggables have evolved with the years, resulting in standardizations like 100ZR, 400ZR/ZR+, 400G Ultra Long Haul, 800ZR/ZR+. They present an increase in capacity and in maximum optical reach, while maintaining a low power consumption [Now24]. Recent techno-economic studies have compared IP+WDM and IPoWDM architectures in optical networks [Gum23, Dav24, Chr22]. In [Gum23], results indicate lower costs when using IPoWDM in access/metro networks but higher costs when applied to core networks compared to IP+WDM. [Dav24] concludes that the optimal choice depends on the bandwidth and the topology, emphasizing that as bandwidth increases, optical express architectures achieve lower costs compared to hop-to-hop architectures. Furthermore, [Chr22] states that the lowest costs are obtained when implementing a hybrid architecture. However, these studies focus mainly on single-band, single-core networks.

To the best of our knowledge, only one study has included multi-band technology, specifically in [Pat23]. This study concludes that IP+WDM achieves up to 12% lower costs compared to IPoWDM. However, with the application of the current coherent pluggable portfolio, these results could vary. Therefore, we consider that there is a research gap in the evaluation of the cost-efficiency of these architectures when combining them with MBoSDM environments. Addressing this gap can help us understand the trade-offs and guide the design of future optical core networks. Based on the research studies and trends, we expect IPoWDM to demonstrate lower cost per bit and energy consumption due to the absence of transponders. Nevertheless, this research work aims to provide the best solution for traffic uncertainty. Therefore, IP+WDM may prove to be a more cost-efficient approach for long-term adaptability, given its higher data rates over longer distances and better thermal management.

3.3.3 Proposed Solution

This research proposes an analysis of IP+WDM and IPoWDM architectures for MBoSDM networks. The study will consider traffic models and topologies focusing on metro/core networks. The network planning stage will incorporate Flexible Engineering Design to address the traffic uncertainty over time.

Current techno-economic solutions consider a traffic model to act as the ground truth, not taking into account alternative scenarios where the traffic may behave differently. In contrast, Flexible Engineering Design is an approach that integrates uncertainty together with economic performance. It is based on a Flexibility Decision Rules (FDR) formulation that can identify when it is adequate to apply flexibility or not [Cap21]. For example, in the case of traffic uncertainty, we can formulate rules that decide whether we allocate more capacity or not, based on the deployment's effects on the final cost. This way, the solution accounting flexibility can reduce the costs of network adaptation in the long term.

The FDRs can be applied via stochastic programming or robust optimization. However, recent studies highlight Reinforcement Learning (RL) as an emerging alternative to expand the exploration and alternative solutions [Cap21]. Therefore, this research will consider an RL-based solution to optimize network upgrades over time for both IP+WDM and IPoWDM architectures. The solution will employ a Graph Neural Network (GNN) to represent the state of the network. The RL agent will make sequential decisions regarding demand upgrades for each year, resulting in a multi-year optimization. The approach is generalized to different networks and demand patterns by considering the components in Figure 3.3-2.

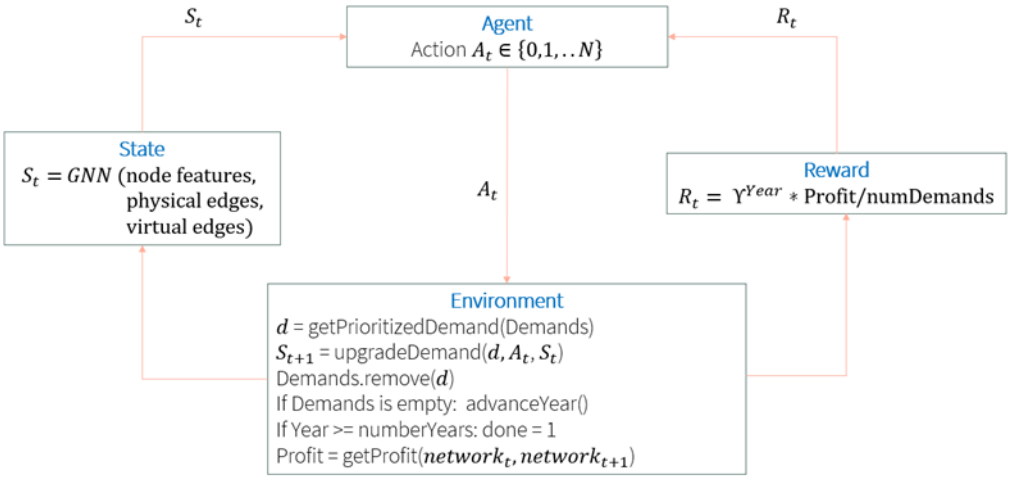

Figure 3.3-2 Problem formulation.

The components of the approach shown in Figure 3.3-2 are explained below.

- Environment: We consider a single environment with an architecture flag to differentiate between IP+WDM, IPoWDM or hybrid design approaches. The environment runs for a

period of years and several demands. To be able to apply our solution to different network sizes with various numbers of demands, we employ an attention mechanism to prioritize the demands at each step. The environment selects the demand with the highest priority and according to the action of the agent, does not upgrade or upgrade in a certain capacity. The upgrade will consider a routing, modulation, spectrum, and core assignment (RMSCA) algorithm, which incorporates the Gaussian noise model and inter-core crosstalk calculations. Once all demand upgrade decisions are applied for a given year, the environment advances to the next year, updating the requested traffic for each demand.

- State: A GNN-based state representation is used to adapt to different network topologies. The state will consider three key components: node features, physical edges and virtual edges. Node features capture information on the node characteristics, e.g. the number of slots/ports used and available. Physical edges represent WDM links and store information regarding link length, capacity and utilization. Virtual edges represent the demands and contain information regarding the capacity requested, capacity provisioned, path selected, and amount of different coherent pluggables/transponders added at each time-period.
- Action: The same action space is applied to both architectures. The action space specifies how to upgrade a demand, where **0** indicates no upgrade, and **N** represents an upgrade of N×100 Gbps.
- Reward: The reward function will consider the discounted profit of the decision divided by the number of demands. The discount factor ensures the multi-year optimization, while the profit reflects cost efficiency. The profit is equal to the revenue of the allocated bandwidth requested by the client, minus the Total Cost of Ownership (TCO). Furthermore, normalizing the reward by the number of demands prevents larger networks from dominating the learning process.

3.3.4 Expected Results

In short, the expected results of this study are as follows.

- The techno-economic analysis will consider a baseline solution for comparison: single-band architecture with parallel fibers, IP+WDM approach and deterministic traffic.
- Following KPI 2.2, a 50% CAPEX reduction can primarily be achieved through the optimization in fiber resources when employing MBoSDM compared to parallel-fibers single-band solutions.
- For the IP+WDM approach with MBoSDM and FDRs, further CAPEX and OPEX reduction in long term is expected mainly due to the employment of FDRs.
- For the IPoWDM approach with MBoSDM and FDRs, further CAPEX and OPEX reduction is expected to be mainly due to the elimination of aggregation layers and low power consumption from coherent pluggables.

3.4 COMPARISON OF DIFFERENT TRANSPORT SOLUTIONS FOR FH IN THE RAN IN DIFFERENT GEOTYPE SCENARIOS AND DIFFERENT TIME HORIZONS

With the evolution towards 6G, the fronthaul segment is expected to become even more bandwidth demanding. As such, coherent technologies are promising candidates to deliver the required levels of bandwidth. However, adopting traditional Point-to-Point (P2P) and Wavelength Division Multiplexing (WDM) approaches can prove costly and inflexible when scaling to meet the increasing demands of 6G networks. The goal of Point-to-Multipoint (P2MP) is to provide a flexible, scalable and efficient solution for network segments where traffic aggregation is essential, in contrast to the traditional approach of mapping the networks solely through P2P networking [Wel21]. Due to its inherent nature, P2MP is well-suited for the RAN to accommodate the fronthaul traffic flows, where multiple Radio Units (RUs) need to be connected to a site hosting the centralized Distributed Unit (DU). In fact, by leveraging Digital Subcarrier Multiplexing (DSCM), P2MP can dynamically allocate bandwidth across multiple nodes, providing improved scalability and resource utilization while reducing the number of required transceivers and fiber links [Her23]. Recent advancements in coherent technologies and DSCM have enabled the development of P2MP transceivers and node solutions capable of supporting high-capacity, cost-effective fronthaul solutions [Tor24, Chr24]. These transceivers utilize DSCM to subdivide the wavelength spectrum into multiple digital subcarriers, each independently managed and allocated, which allows for flexible bandwidth distribution and efficient traffic aggregation. This capability makes P2MP an attractive option for next-generation mobile transport networks, especially in urban and suburban environments where traffic demands are highly variable and an easy reconfigurability of circuit data rates can lead to significant advantages. DSCM transceivers used for P2MP networking is also considered in other studies included in the of this document, such as the one on robust network design reported in subsection 3.7 and the one on power consumption reported in subsection 5.2. Both the studies presented in subsections 3.7 and 5.2 concern the metro aggregation segment, while the one presented in this subsection is related to the access and, as said above, more in specific to the RAN.

As P2MP is still an emerging technology, there is a need to evaluate its techno-economic applicability for fronthaul deployment in next-generation mobile networks where the cost of transport can compromise economic sustainability. This study aims to assess the feasibility and benefits of adopting P2MP in comparison with traditional P2P and WDM approaches across various deployment scenarios, including dense urban, urban, suburban, and rural environments in line with what has been defined in the project deliverable D2.1 [SeaD2.1] as geotype reference scenarios. As a preview of the obtained results, we can anticipate that while the migration towards P2MP requires limited effort in terms of Capital Expenditure (CAPEX), it introduces significant reductions in energy consumption, demonstrating that P2MP can provide a cost-effective alternative to conventional transport solutions for the fronthaul with the possibility to maintain a high level of performance.

3.4.1 Architecture Description

Figure 3.4-1 shows the reference architectural solutions considered in this analysis. This architecture is related to the scenario for the medium term, for the long term the architecture is similar, but the systems and the capacity involved are increased as shown in Figure 3.4-2. The network architecture used for this evaluation consists of four different configurations: Point-to-Point (P2P), Wavelength Division Multiplexing (WDM), Point-to-Multipoint (P2MP), and Point-to-Multipoint with Pre-Aggregation (P2MP-WP). Each configuration is applied to the four distinct geotypes as defined in [SeaD2.1]: dense urban, urban, suburban, and rural. Here, we consider the transport solutions for realizing the fronthaul of the mobile network, i.e., interconnecting RUs with heterogeneous capacity to DUs, either physical or virtual (vDUs), located at a Central Office (CO) site.

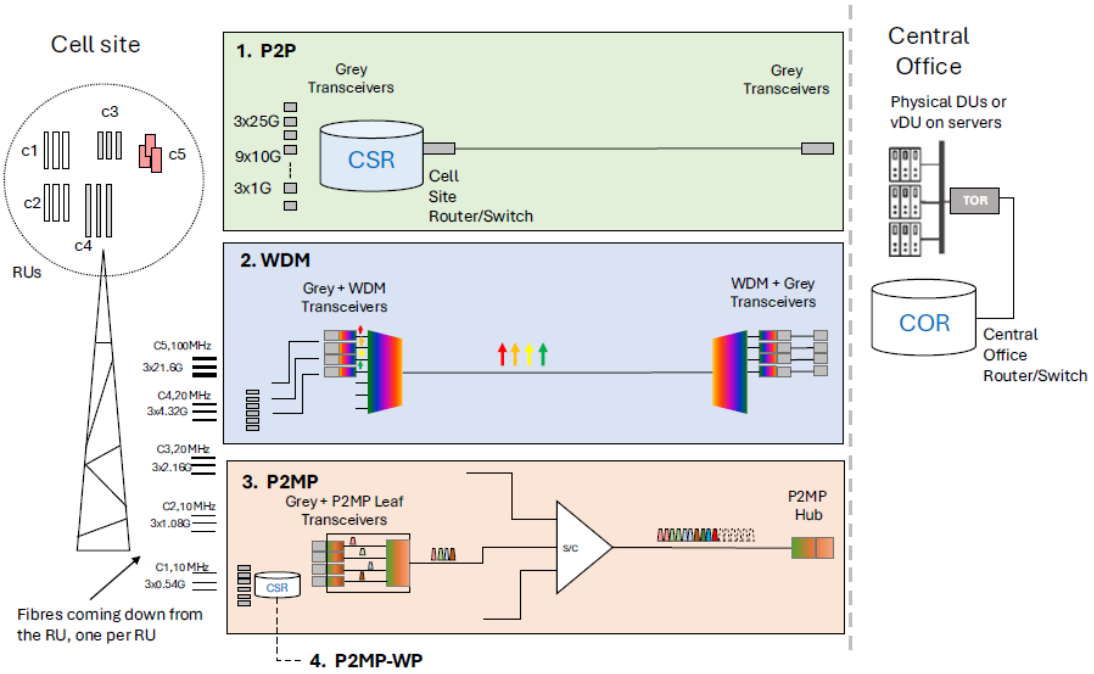

Figure 3.4-1 Reference Architectural Solutions (Medium term).

In the P2P configuration (upper part of Figure 3.4-1), RUs are connected to a Cell Site Router/Switch (CSR) via Short Reach grey transceivers. The traffic is aggregated by the CSR and sent to the CO using a dedicated fiber link and Long Reach Grey transceivers. The traffic is then disaggregated at the CO by a Central Office Router/Switch (COR) equipped with high capacity Grey transceivers. This architecture provides high reliability and capacity but may result in high Operational Expense (OPEX) due to the need for power-consuming high-capacity switches in the cell sites.

The WDM architecture shown in the middle part of Figure 3.4-1 introduces wavelength multiplexing to aggregate multiple RUs on a shared fiber using different wavelengths. 10G-400G grey transceivers (on RUs) are used in combination with WDM transponders (grey at tributary

RU side, colored at line side toward the Central office) and multiplexing equipment (both at the base of the trellis where RUs are mounted) to achieve wavelength multiplexing, allowing multiple signals to be transmitted simultaneously over the same fiber. Although this architecture enables efficient fiber usage, it requires complex and costly hardware, which could significantly impact CAPEX.

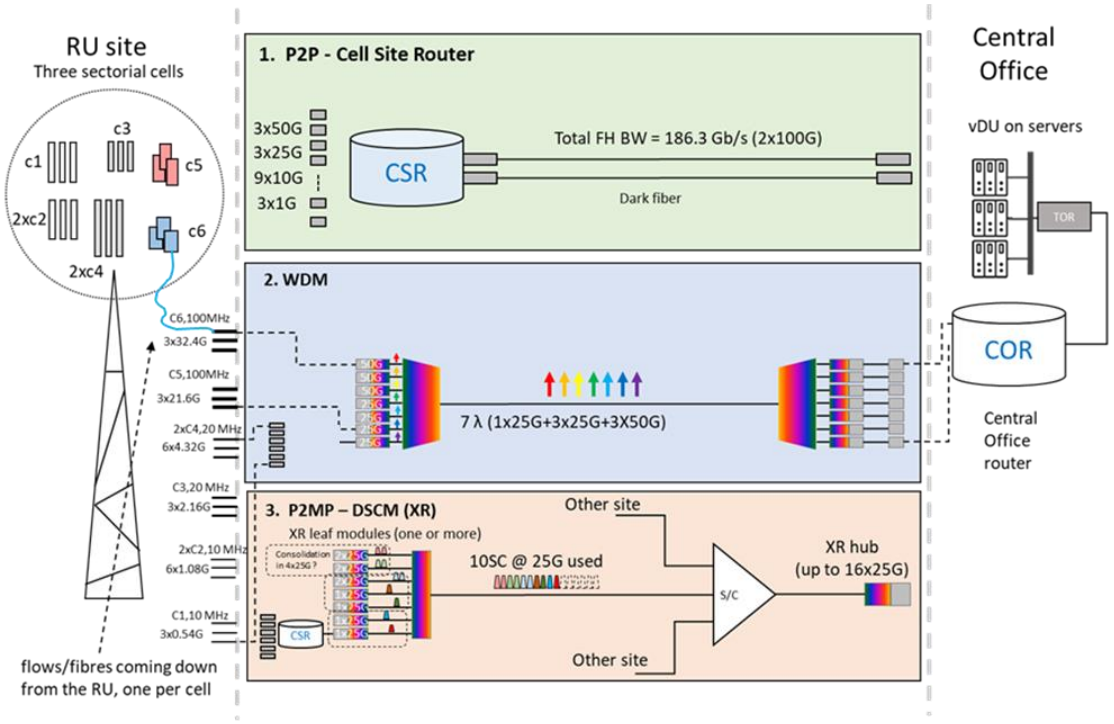

Figure 3.4-2 Reference Architectural Solutions (Long term).

By employing DSCM, the P2MP architecture leverages a shared optical link to connect multiple RUs to the CO as depicted in the lower part of Figure 3.4-1. Each cell site is equipped with demarcation units, each of which hosting grey transceivers with a minimum granularity of 25G, which are conveyed onto digital subcarriers via P2PM Leaf pluggable modules. The FH flows sent by the leaves in the cell sites are aggregated at the CO by P2MP hub modules with up to 16×25G capacity. While enabling fiber link sharing, this approach, thanks to its ability to aggregate multiple subcarriers, reduces the need for switches at the cell site, making it a promising cost-effective solution. Since the P2MP has a minimum granularity of 25G, fronthaul segments requiring low data rate (as the ones with carrier width of 20 MHz or less) may lead to inefficient utilization of DSCM. The P2MP-WP configuration extends the P2MP architecture by incorporating a packet pre-aggregation level via a low-capacity CSR responsible for packing multiple low-capacity fronthaul segments onto a single DSCM channel. The P2MP-WP solution enhances the resource efficiency of P2MP at the cost of introducing an additional switching level. The advantage in this case (i.e., P2MP-WP) is that, unlike the P2P architecture explained before, the switch can be of much smaller capacity (a few tens of Gb/s instead of hundreds of Gb/s).

We considered four different deployment scenarios to evaluate the proposed fronthaul solutions. They are the four geotypes defined in [SeaD2.1]: dense urban, urban, suburban, and rural environments. The area sizes for these scenarios range from 0.64 to 163.84 square kilometers. The different geotypes correspond to unique topologies and compositions of macro and small cell sites, each with distinct radio deployments involving multiple radio bands and bandwidths, reflecting Medium Term (MT) and Long Term (LT) capacity requirements.

Table 3.4-1 Radio Layers Parameters for macro cell sites of an Urban geotype for Medium Term period.

Carrier	Bands range [GHz]	Carrier width [MHz]	Num. of bands	FH capacity [Gb/s]	Num. of carriers
C1	Sub GHz	10	4	4.32	8
C2	1 to 3	20	4	8.64	8
C3	3 to 7	100	2	21.6	4

In Table 3.4-1 the radio layers parameters and the required FH capacities of the cells for macro cell sites of an Urban geotype in the Medium Term are reported. Three type of radio layers are present, of which only one (C3) is high FH data rate demanding. Different multiplicity of bands and carriers are considered per radio layer. Here, we assume all the radio elements supporting 4 MIMO Layers. Concerning the small cell site, for Urban geotype in the Medium Term the site is equipped with two layers within a single cell (instead of three of the layers in macro cell sites). Small cell site is equipped with 3-7 GHz and 24-26 GHz band range with 100 MHz and 200MHz channel width, respectively. This results in a FH data rate requirement up to 43.2 Gb/s per radio equipment.

FH requirements of RU cells of macro cell sites of an Urban geotype for Long Term is given in Table 3.4-2. In Long Term macro cell sites are equipped with 8 radio layers with two very high FH data rate demanding layers. Small cell sites are equipped with three layers, i.e., 3-7 GHz, 7-15 GHz and 24-26GHz bands.

Table 3.4-2 Radio Layers Parameters for macro cell sites of an Urban geotype for long term period.

Carrier	Bands range [GHz]	Carrier width [MHz]	Num. of bands	FH capacity [Gb/s]	Num. of carriers
C1	Sub GHz	10	4	4.32	12
C3	1 to 3	20	4	8.64	16
C5	3 to 7	100	2	21.6	8

Macro cell sites are assumed to offer three cells connectivity while only one is assumed for the small cell site. In summary, for the Urban geotype, the total cell site fronthaul required capacity spans from 43.2 Gbps for small cells in the MT to 272 Gbps for macro cells in the LT. FH flows data rates for Dense Urban geotype are similar while for the Suburban and Rural geotypes values for total FH data rates are lower. It is worth mentioning that the adopted modelling can be flexibility customized to evaluate fronthaul requirements of different radio scenarios, e.g., varying numerology and MIMO layers.

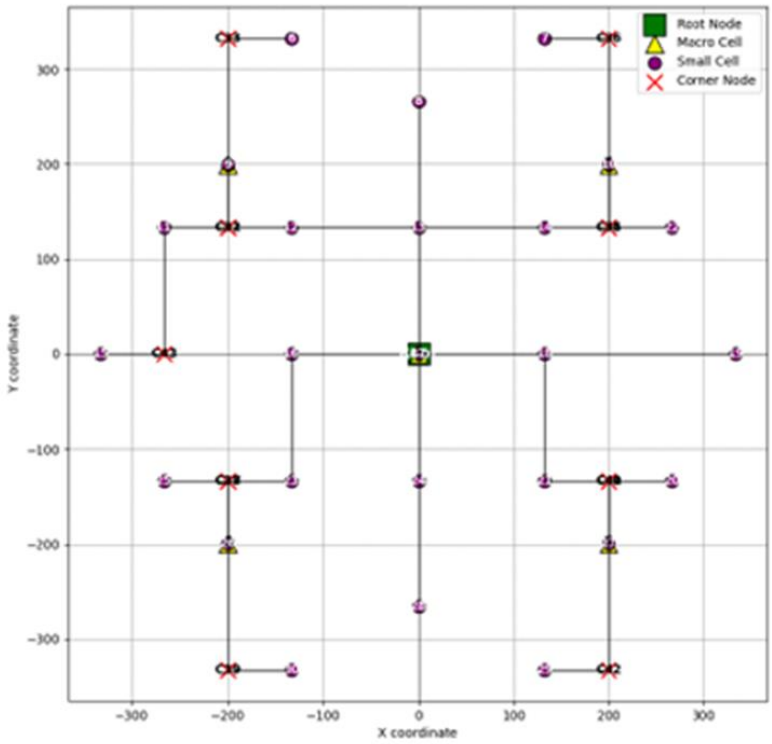

Figure 3.4-3 Example of topology of the three collecting FH small and macro cell sites FH flows over the physical fiber layout in a Dense Urban geotype.

Figure 3.4-3 shows the considered fiber footprint in a dense Urban geotype and how FH flows are collected in small and macro cell sites to convey them to the Central office. The figure shows how the macro sites (yellow triangles) and small sites (purple circles) are connected with a tree structure obtained on the geotype grid towards the root constituted by the central office (green square). On the tree it is assumed that there is sufficient fiber availability to implement the applied transport solution (one of those illustrated above). Note the corner nodes (red crosses) which are points in the physical topology where, using splitter and combiner devices, the topological branches coming from single or aggregation of cells can be joined, allowing efficiency and fiber savings.

3.4.2 Cost Model

For the CAPEX calculation and comparison and for each scenario examined, we include the cost of all components required for implementing the network infrastructure between the RUs and DUs.

For this purpose a cost model has been defined: it is based on costs found on public sites for mature and widespread devices (i.e., IMDD transceivers, grey or WDM, of different reach (Short reach (SR, 100 m), Extended reach (ER, 30 km), WDM mux/demux, routers of different sizes), while for devices that are under R&D or pre-commercial phase (i.e., coherent DSCM P2MP hub and leaf modules) the costs have been obtained by commercial products made with comparable

technology and performances, adding a small surcharge motivated by additional features. While we recognize the inherent limitations of this approach, it provides a useful and meaningful basis for comparison.

Table 3.4-3 Cost and power consumption parameters of grey and WDM transceivers.

Device	Data Rate	Reach	Normalized price (UC)	Power consumption [W]
Grey Transceiver	1G	SR (100 m) MMF	0.002	1.0
	10G	SR (100 m) MMF	0.004	1.0
	25G	SR (100 m) MMF	0.008	1.0
	50G	SR (100 m) MMF	0.054	1.5
	100G	SR (100 m) MMF	0.020	2.5
	400G	SR (100 m) MMF	0.080	10.0
	1G	LR/ER (30/40 km) SMF	0.010	1.0
	10G	LR/ER (30/40 km) SMF	0.020	1.0
	25G	LR/ER (30/40 km) SMF	0.080	1.5
	50G	LR/ER (30/40 km) SMF	0.200	4.0
	100G	LR/ER (30/40 km) SMF	0.300	4.5
	400G	LR/ER (30/40 km) SMF	1.000	10.0
WDM transceivers	1 G	LR/ER (30/40 km) SMF	0.020	1.0
	10G	LR/ER (30/40 km) SMF	0.050	1.6
	25G	LR/ER (30/40 km) SMF	0.160	2.0
	50G	LR/ER (30/40 km) SMF	0.360	4.5
	100G	LR/ER (30/40 km) SMF	0.500	4.5
	400G	LR/ER (30/40 km) SMF	1.800	10.0

Table 3.4-4- Cost and power consumption parameters of DSCM XR modules.

Device	Type	Note	Normalized price (UC)	Power consumption [W]
XR 100 G module	pluggable	coherent DSCM ≈ 200 km reach	0.60	3.5
XR 200 G module	pluggable	coherent DSCM ≈ 200 km reach	1.00	4.5
XR 400G module	pluggable	coherent DSCM ≈ 200 km reach	2.20	8
Media Converter 100G	box	for client-XR module adaptation	0.40	2
Media Converter 200G	box	for client-XR module adaptation	0.60	3
Media Converter 400G	box	Usually not necessary	1.00	5

Table 3.4-5 Cost, power consumption and other parameters of WDM devices.

Device	Mux/Demux channels	Insertion loss / Attenuation (split)	Normalized price (UC)	Power consumption [W]
CWDM mux/demux	8	5.5 dB	0.160	1.0
WDM mux/demux	40	3.2 dB	0.240	1.0
Splitter/combiner	1:2	3.5 dB	0.020	0.0
Splitter/combiner	1:4	7 dB	0.020	0.0

Table 3.4-6 Cost, power consumption and other parameters of packet switching equipment.

Device	Equipment size	Capacity [Gb/s]	Normalized price (UC)	Power consumption [W]
Switch/Router (total capacity at bid. interfaces)	Small	400	0.60	250.0
	Medium	1600	1.60	350.0
	Large	3200	2.80	460.0
	Extra Large	6400	4.80	620.0

The cost parameters used in the study are differentiated in four sections: transceivers (Table 3.4-3), DSCM XR modules (Table 3.4-4), WDM devices (Table 3.4-5) and packets switching equipment (Table 3.4-6). Prices are normalized given in unit of cost (UC) where a unit of UC correspond to the cost of an extended reach (ER, 40 km) gray transceiver.

For devices that are still in R&D or pre-commercial phases (e.g., coherent DSCM P2MP modules), we assume a 35% cost increase over an equivalent-capacity grey transceiver, reflecting the surcharge for additional advanced features.

The tables also include the power consumption of devices (in Watts). Value of power consumption are the typical one for Transceiver, XR and WDM equipment. For routers power consumption values in table are maximum values. For routers it is assumed that the values in the table are for the full load condition while in an idle state (very low or no traffic) the router consumes half of the maximum value.

3.4.3 Results

The results of the technical-economic analysis conducted with the hypotheses presented above are reported in Figure 3.4-4 where the CAPEX evaluations are reported in the upper part (insets (a) to (d)) and the energy consumption in the lower part (insets (f) to (h)). As shown in Figure 3.4-4(a-d), in the CAPEX evaluation we distinguish between switching and transmission equipment costs. Since TCO is significantly impacted by OPEX, and energy represents the main OPEX contributor among the different architectural solutions, we also analyze the annual energy consumption of the deployed equipment as it is shown in Figure 3.4-4(f-h).

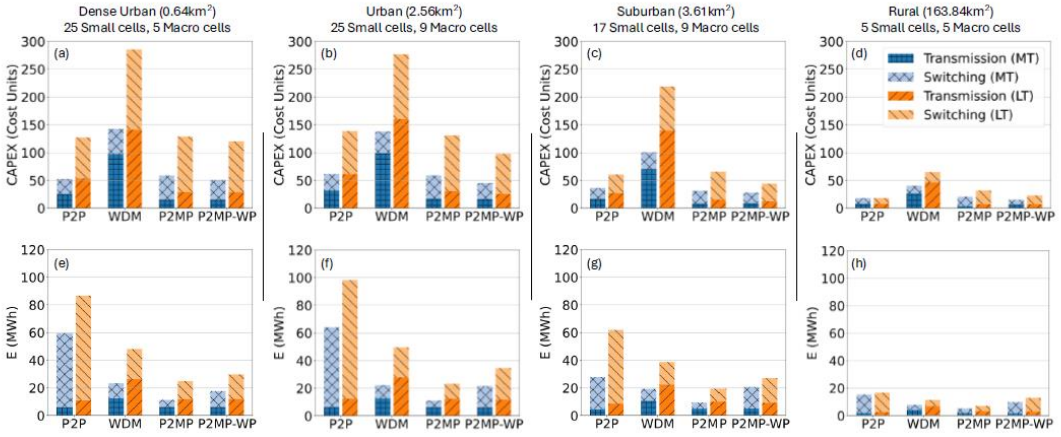

Figure 3.4-4 Summary of results of techno economic analysis on FH transport solutions comparison: (a) to (d) CAPEX; and (e) to (h) energy consumption.

Results on CAPEX show that WDM is the most expensive solution due to the complexity of the transmission equipment required, leading to a CAPEX increase of up to 125% compared to P2P across all scenarios. P2MP generally demonstrates viable CAPEX performance, offering a lower overall expenditure compared to WDM and a competitive position relative to P2P, particularly when considering P2MP's potential to reduce OPEX. Specifically, in the urban scenario, where the combination of fronthaul flows allows for a reduction in the number of transmission devices used, P2MP-WP can even achieve a CAPEX reduction of up to 10% in the medium and long term.

As far as concern energy consumption, insets (e) to (h) of Figure 3.4-4 report the annual energy consumption (E) for the transmission and switching components. The annual consumption for P2MP and P2MP-WP architectures is significantly lower compared to P2P and WDM. For instance, in dense urban areas, P2MP solutions consume up to 70% less energy compared to P2P solutions, highlighting the efficiency of P2MP in managing both MT and LT power requirements. Similar trends are observed in suburban and rural scenarios, where the P2MP and P2MP-WP configurations demonstrate better energy efficiency, making them more sustainable for long-term deployment. The annual consumption for P2MP and P2MP-WP architectures is significantly lower compared to P2P and WDM due to the substantial reduction of switching devices. It is worth mentioning that P2MP-WP offers higher efficiency in terms of resource utilization at the cost of increased hardware complexity and energy consumption.

Summarizing, in the study presented in this subsection of the deliverable the techno-economic performance of coherent P2MP as a fronthaul solution for next generation mobile networks has been performed. It is worth noting that, while energy estimation parameters are less subject to uncertainty, CAPEX evaluation is more affected by market dynamics. However, this does not alter the overall validity of P2MP's ability to offer significant potential for OPEX reduction while requiring only a reduced CAPEX difference compared to traditional approaches. The results demonstrate that P2MP solutions offer a cost-effective and energy-efficient alternative to

traditional P2P and WDM architectures, making them a promising choice for diverse deployment scenarios.

3.5 Coordination of Radio Access and Optical Transport Operation to Reduce Optical Capacity Overprovisioning

The advent of B5G/6G will revolutionize the way RAN will be operated. Expected massive small cell deployments and features, such as an adaptive functional splitting, are expected to change not only the volume but also the requirements of the traffic to be supported by the fixed transport network. This section presents an insight into smart RAN operation, focusing on how such operation will impact the autonomous operation of the fixed network. Based on tailored traffic models, a preliminary numerical analysis is done to highlight that smart and dynamic RAN operation lead to sharp fixed network traffic changes that require from coordination RAN-fixed transport coordination to achieve efficient use of optical capacity resources while guaranteeing e2e QoS.

This section is divided in the following subsections:

- The reference e2e scenario is firstly presented.
- Then, smart RAN operation is sketched and its impact on the fixed transport network anticipated.
- Traffic models to compute the aggregated traffic in both access and metro segments are presented.
- Using the models, some numerical scenarios are reproduced and the impact of traffic changes in optical transport due to smart RAN operation is evaluated.
- Conclusions raise the need of coordination of RAN and fixed optical networks operation to achieve e2e optimal use of capacity resources. Further directions are pointed out, whose main achievements and results will be presented in D2.3.

3.5.1 Reference Scenario

In the RAN, we assume that a cell consists of a single macro base station (MBS) and a number of micro-BSs (µBSs). MBSs provide full coverage within their cells and provide the minimum capacity to absorb users' traffic, whereas µBSs complement the capacity of the MBS within a limited area of the cell. We assume that µBSs provide two operational modes: (*i*) *active*, where the µBS is switched on and fully operational, and (*ii*) *sleep*, where the µBS is switched off. Without loss of generality, we assume that the radio units (RUs) on both the MBS and the µBSs provide support for e2e traffic flows. RAN cells provide radio connectivity to the UE and require one of the following main service classes [Sul22]: (*i*) enhanced mobile broadband (eMBB), (*ii*)

ultra-reliable low-latency communications (URLLC), or (*iii*) massive Internet of Things (mIoT). It is worth mentioning that eMBB typically requires a large capacity (~150 Mb/s per UE and service) with relaxed e2e latency requirements (~4 ms from the UE to the core). Conversely, the URLLC service has very stringent latency requirements (~1 ms) and reduced capacity. Finally, mIoT is typically highly distributed, which entails the management of a large amount of UE injecting moderated bandwidth (in the order of tens of Mb/s) with intermediate target e2e latency assurance (~2 ms)

Figure 3.5-1a illustrates the 5G high-level reference architecture considered in this work, where the traffic generated by the UE in a cell sequentially traverses a number of functions, namely RU, DU, and CU, until reaching the UPF that serves as a breakout point of the 5G core [Gav21]. Thus, the resultant *graph* can be split into four different *slice links*, characterized by the RAN segment, i.e., radio (between UE and RU), F-H (between RU and DU), M-H (between DU and CU), and B-H (between CU and UPF). All these functions can be virtualized and run on the computing resources (servers, virtual machines, or containers) that are available at the different sites of the network. The B5G architecture is supported by resources in the fixed network infrastructure, for both connectivity, i.e., capacity and ensured latency, and computing. The e2e B5G reference topology considered in this work is depicted in Figure 3.5-1b, where the main network segments connecting the sites and the central offices (COs) are sketched. This topology is based on the reference high-level topology from the major European network operators presented in [Rui23]. Therefore, the traffic of a cell enters the fixed network. Specifically, an access optical network connects the cell sites with their reference *access CO* (ACO). Typically, the distances between the RAN cells and their ACO site are short, i.e., from a few to tens of km. In addition to their optical transport and switching capabilities, ACO sites have small datacenters equipped with computing and storage resources that enable the deployment of virtualized DU/CU functions, as well as other UPF functions. Typically, ACOs aggregate traffic from various RAN cells in the nearby area, as well as from other access technologies, such as residential gateways or customer edge premises. ACOs are interconnected with each other and with *regional COs* (RCO) by metro aggregation networks. RCOs are further from the UE (around hundreds of km) and larger and more complex than ACOs; hence, they can host more virtualized functions and achieve higher efficiency. Finally, RCOs are interconnected with *national COs* (NCO) by means of a meshed metro core network, which provides large computational capabilities and serves as a gateway to other networks.

Figure 3.5-2 illustrates the overall architecture considered in this work, including the control and orchestration planes; this architecture is an adapted version of the O-RAN architecture [Ora25]. The main entity responsible for RAN domain management is the RAN intelligent controller (RIC) that is in charge of a wide set of actions, such as QoS-based resource optimization, traffic steering, and RAN energy efficiency, just to mention a few. The RIC is divided into the near real-time RIC and non-real-time RIC. The near real-time RIC controls the RAN elements and their resources by means of local control loops that typically run in the range of 10 ms to 1 s; it receives policies from the non-real-time RIC that runs in the service management and orchestration system, which enables wide control loops that require an execution time of more

than 1 s. For the sake of simplicity, we hereafter refer to the unified RAN control entity that combines near real-time and non-real-time operation as simply the RIC. Specifically, we assume that the RIC deals with cell configuration, e.g., BS on/off switching, and that it manages the DU/CU placement for each slice [Sar21]. The core network orchestrator is responsible for the core functions; specifically, we assume that it manages the UPF placement for each slice. A slice manager is in charge of making decisions related to the configuration of each slice for service level agreement assurance. Finally, in the transport network domain, the orchestrator coordinates actions with the SDN control plane. It is worth noting that the orchestrator layer provides O-Cloud functionality [Ora25], i.e., it manages the computing nodes running in each site, as well as the connectivity between sites [Cas18].

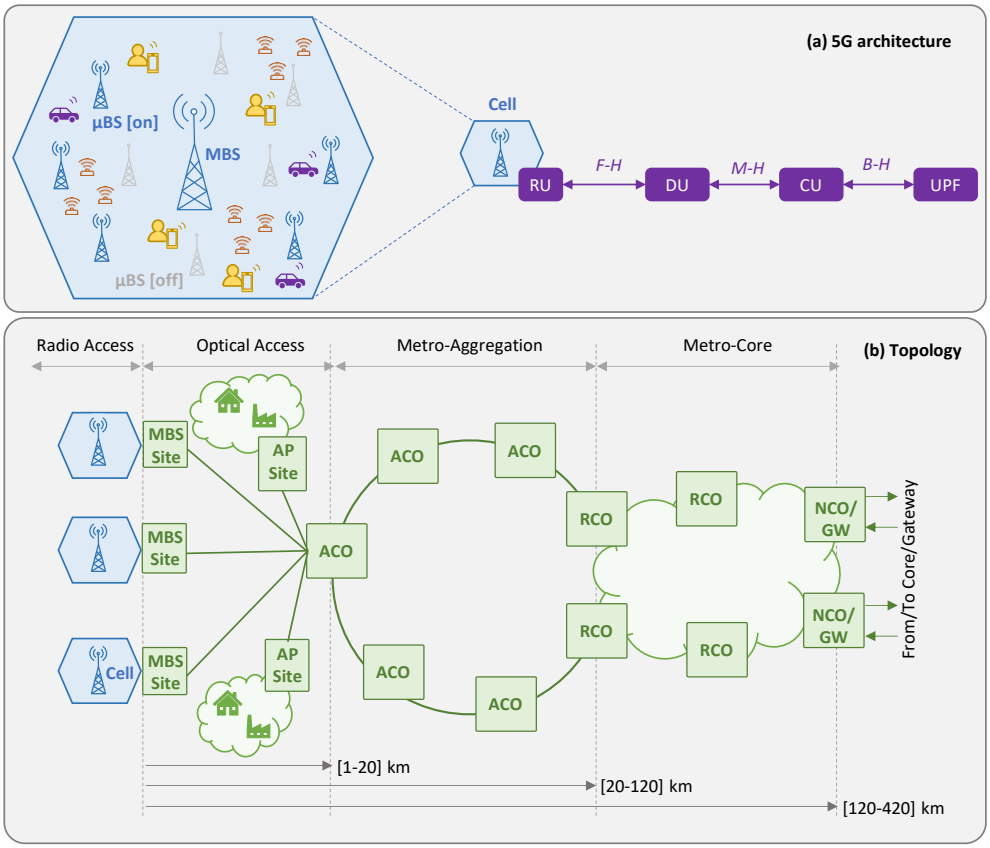

Figure 3.5-1 Reference 5G architecture (a) and topology (b).

Without loss of generality and in line with [Rui23], the sites are equipped with optical transponders (TP) that allow their connection to remote sites by establishing an optical connection. In addition, in this paper we consider DSCM TPs, which can allocate a variable number of sub-carriers to adapt the capacity to the traffic needs.

The mapping of the slice links connecting functions onto optical connections depends on the slice configuration (capacity and placement of virtual functions) managed by the slice manager, which, in turn, consumes resources (computing and connectivity). Note that the placement of

the functions cannot be conducted in any potential location site due to the constraints of each RAN segment, such as distance between sites and latency requirements [Ets22].

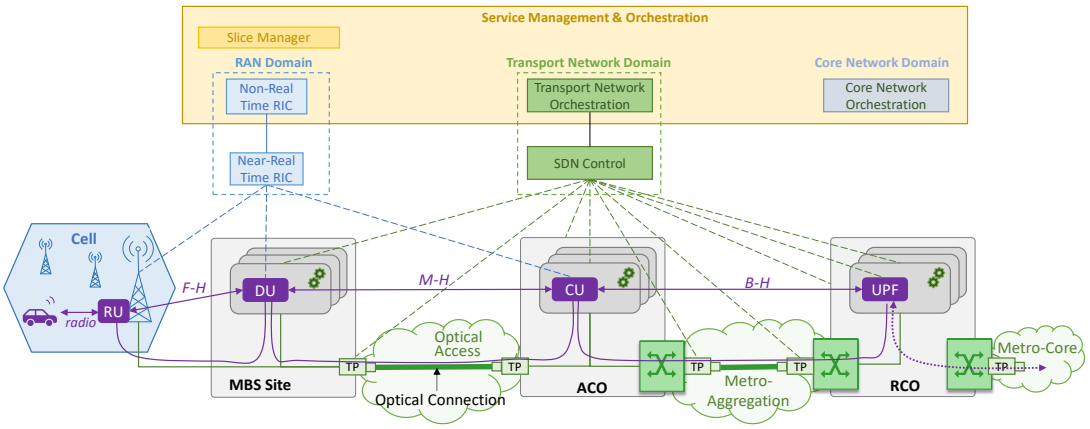

Figure 3.5-2 High-level architecture.

Table 3.5-1 summarizes the mapping of the virtual functions and site types, based on a typical network operator configuration [Rui23]. In the case of DU and assuming split 7.2 for F-H, only MBS and ACOs are suitable for its deployment. However, M-H latency can be relaxed by means of split 2, which allows the extension of its placement to RCO if suitable, i.e., for eMBB services. Regarding UPFs, without loss of generality, we assume that they consist of processes that require more intensive computation and centralization than those of DU/CU. Therefore, due to the very limited availability of resources at the MBS, the placement of such functions is avoided at the very edge of the network. In addition, although function placement is allowed in ACOs, their computational resources are reserved for URLLC and mIoT services due to their limited capacity.

Table 3.5-1 Virtualized function placement constraints.

Function	MBS	ACO	RCO	NCO
DU	Yes	Yes	Yes (eMBB)	No
CU	Yes	Yes	Yes	No
UPF	No	Yes (URLLC, mIoT)	Yes	Yes

3.5.2 Smart RAN Operation

Smart slice operation is built upon three main pillars: *(i) dynamic µBSs management*, by switching the µBSs on and off , with the objective of reducing energy consumption in the RAN, while ensuring the minimum capacity needed to support UE traffic; *(ii) dynamic RAN capacity slicing*, with the aim of managing physical radio blocks (PRBs) to assign resources to each of the different slices in order to provide the required QoS; and *(iii) flexible functional split operation*, where the placement of virtual functions (DU/CU) is adapted to match the requirements of the UE served by each BS in a cell. In this section, we aim to illustrate how that smart slice operation

dramatically affects the traffic supported by the underlying transport network in each of the segments of the reference topology.

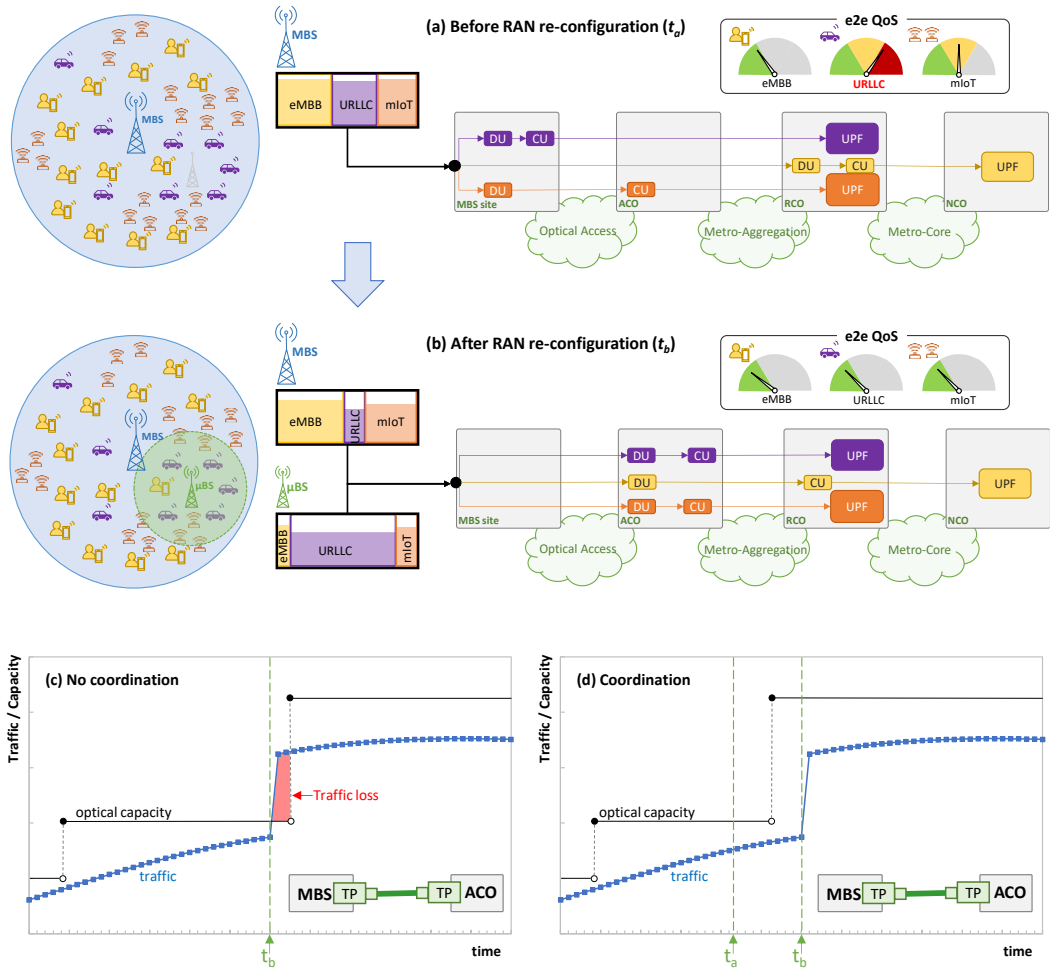

Figure 3.5-3 Example of RAN reconfiguration before (a) and after (b) BS activation and function placement reconfiguration. Capacity allocation in optical access without (c) and with (d) RAN-fixed network coordination.

Figure 3.5-3a shows the RAN state at a given time t_a of an example consisting of one cell with one active MBS that provides connectivity to a mix of UE from different services. For the sake of simplicity, we assume that one slice per service type is deployed. Let us assume that the core network orchestrator decides, at the slice provisioning time, the placement of UPF according to slice type and QoS requirements. This UPF placement remains fixed during the slice's lifetime. Moreover, each slice has its own placement of DU/CU along the different CO sites (see Figure 1b). In this case, DU/CU placement can be dynamically reconfigured by the slice manager according to current and expected UE traffic conditions to guarantee that e2e latency (i.e., from UE to UPF) meets the requirements of the slice service type. The figure also shows a simplified view of the PRBs used by each of the slices. Table 3.5-2 shows the RAN segment per service class that is transported in each of the network segments. Note that the traffic in each segment is a heterogeneous mix of F-H, M-H, and B-H traffic, depending on the slice configuration. The selected time instant t_a illustrates a scenario in which the radio resources are reaching a point

of saturation that is negatively affecting the e2e service QoS (represented by colored gauges). In particular, the URLLC service is strongly affected by such saturation, even when the DU/CU functions are currently placed as close as possible to the UE to reduce e2e latency. In view of this, let us imagine that such QoS degradation is detected by the slice manager and that, after analysis, some *slice reconfigurations* have been identified; consequently, there are several actions to be performed. First, the slice manager triggers the activation of an available µBS (in light grey in Figure 3.5-3a). Due to the physical location of the antenna and its proximity to the majority of the URLLC UE, the activation of this new antenna relieves the MBS from having to serve most of the URLLC traffic. Figure 3.5-3b shows the RAN state after the activation of such a µBS at time instant t_b. As the activated µBS (now in green) captures most of the URLLC traffic, the overall RAN load is reduced and, consequently, the delay introduced by the RAN segment [Ber20], which in turn makes the e2e QoS of all the services reach the desired target performance.

Table 3.5-2 Network traffic before reconfiguration (time t_a).

Service Class	MBS <-> ACO [Optical Access]	ACO <-> RCO [Metro Aggregation]	RCO <-> NCO [Metro Core]
URLLC	B-H	B-H	-
eMBB	F-H (7.2)	F-H (7.2)	B-H
mIoT	M-H (2/4)	B-H	-

Nonetheless, smart slice operation goes beyond µBS activation. For instance, to reduce the cost associated with virtual function placement, URLLC and mIoT functions can be now located far from the edge (where the available resources are typically cheaper) without major impact on the QoS of those services. This action might require the reallocation of some of the functions of the other slices, for the sake of global optimization (as illustrated with the reallocation of the eMBB functions). Therefore, because of this smart slice reconfiguration (of both µBS activation and virtual function reallocation), the traffic supported in the fixed network segments sharply changes. Table 3.5-3 updates Table 3.5-2 after slice reconfiguration, where we observe segments that are greatly affected, e.g., the traffic in the optical access sharply increases due to the addition of large F-H traffic volumes.

Table 3.5-3 Network traffic after reconfiguration (time tb). Changes w.r.t Table 3.5-2 are in boldface.

Service Class	MBS <-> ACO [Optical Access]	ACO <-> RCO [Metro Aggregation]	RCO <-> NCO [Metro Core]
URLLC	**F-H (7.2)**	B-H	-
eMBB	F-H (7.2)	**M-H (2/4)**	B-H
mIoT	**F-H (7.2)**	B-H	-

3.5.3 Traffic model for analysis purposes

The proposed model aims at characterizing, for every time t, the access and metro traffic flow components (variables y_{cat} and z_{amt}, respectively), as a function of input traffic at every BS (variables x_{bt}). This model considers the aggregated traffic from all slices of different services. We assume that a given RAN cell $c \in C$ connects to one single access site $a \in A$ and metro site $m \in M$ and, consequently, all BS $b \in B$ in cell c have the same reference access and metro sites. Independently of where DU and CU functions are placed, the traffic generated from BS b will traverse the fixed access segment until reaching reference access site a and then, will traverse the fixed metro segment from a to reference metro site m. Table 3.5-4 summarizes the used notation.

The traffic flow model is defined through the following equations. Eq. 5 models the traffic that a given BS b injects into the access network (y_{bt}). The value is zero if the BS is not active; otherwise, it can be F-H, M-H, or B-H depending on the placement of DU/CU functions. Similarly, Eq. 6 characterizes the traffic injected into the metro network (z_{bt}). Note that these two variables do not depend on the actual network configuration, e.g., where a given function is placed. The output is the expected F-H or M-H capacity for each cell i for the next period, $z_i(\mathrm{t}+1)$, which depends on the functional split and $y_i(\mathrm{t}+1)$ be the traffic monitored at time t. The generic model for split s, based on models in [Per18], is defined in Eq. 7, and where $\eta_{ij}^{s}(\mathrm{t}+1) \in [0,1]$ is a factor that scales the component K_j^sthat accounts for the F-H traffic that cell j injects at maximum load when split s is used. The scaling factors η for the considered splits in this work are in Eq. 8 and Eq. 9. At the same time, C_j is the maximum RAN capacity of cell j. From Eq. 8 and Eq. 9, we clearly observe how F-H traffic in split 7.2 scales proportionally to user traffic, whereas split 2/4 produces a constant F-H traffic per BS. In addition, although component K depends on multiple BS parameters, such as the number of antennas, layers, and chosen modulation format (see [Per18] for further details), $K_{2/4}^{j} > K_{7.2}^{j}$ for any BS j. Eq. 10 and Eq. 11 compute the target access and metro traffic flow components, respectively. For a given pair cell-access site $< c, a >$ and pair access-metro site $< a, m >$, y_{cat} and z_{amt} aggregate the components of every BS that is in cell c and has assigned the access site a and metro site m as reference ones.

Table 3.5-4 Parameters and variables.

ρ_b: 1, if BS b is active	δ_{bc}: 1, if BS b is in cell c	x_{bt}: User traffic in BS b at time t [Gb/s]
k_b: Capacity of BS b [Gb/s]	δ_{ba}: 1, if BS b sends to access site a	y_{bt}: Access traffic by BS b at time t [Gb/s]
du_b: Position of DU of BS b [site type]	δ_{bm}: 1, if BS b sends to metro site m	z_{bt}: Metro traffic by BS b at time t [Gb/s]
	fh_b: Max F-H traffic of BS b [Gb/s]	y_{cat}: Traffic in pair <c, a> at time t [Gb/s]
cu_b: Position of CU of BS b [site type]	mh_b: Max M-H traffic of BS b [Gb/s]	z_{amt}: Traffic in pair <a, m> at time t [Gb/s]

Eq. 5

$$y_{bt} = \rho_b \cdot \begin{cases} x_{bt}, & if\ cu_b == "cell" \\ mh_b, & if\ cu_b \neq "cell"\ \&\ du_b == "cell" \\ x_{bt} \cdot \dfrac{fh_b}{k_b}, & otherwise \end{cases}$$

$$z_{bt} = \rho_b \cdot \begin{cases} x_{bt} \cdot \dfrac{fh_b}{k_b}, & if\ du_b == "metro" \\ mh_b, & if\ du_b \neq "metro"\ \&\ cu_b == "metro" \\ x_{bt}, & otherwise \end{cases} \quad \text{Eq. 6}$$

$$z_i(t+1) = \sum_{j=0..N} y_{ij}(t+1) \cdot \eta_{ij}^{s}(t+1) \cdot K_j^S \quad \text{Eq. 7}$$

$$fh_{b_{7.2}}(t+1) = \frac{x_{ij}(t+1)}{C_j} \quad \text{Eq. 8}$$

$$\eta_{ij}^{2/4}(t+1) = 1 \quad \text{Eq. 9}$$

$$y_{cat} = \sum_{b \in B} \delta_{bc} \cdot \delta_{ba} \cdot y_{bt} \quad \text{Eq. 10}$$

$$z_{amt} = \sum_{b \in B} \delta_{bc} \cdot \delta_{bm} \cdot z_{bt} \quad \text{Eq. 11}$$

3.5.4 First results

For numerical evaluation purposes, we have built a Python-based flow-based simulator that reproduces the e2e B5G scenario presented in Figure 3.5-1. To simplify the analysis of access and metro traffic components, we configured a scenario consisting of one dense RAN cell with 1 MBS and 64 µBS, one access site, and one metro site. We consider typical configurations for MBS (2x2 MIMO, 20 MHz bandwidth) and µBSs (8x8 MIMO, 100 MHz bandwidth).

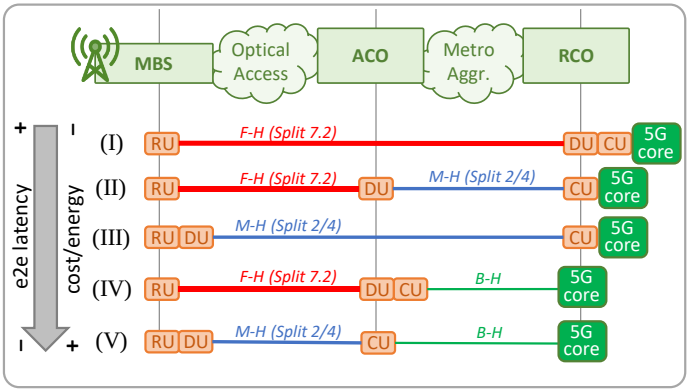

Figure 3.5-4 Functional split options.

The maximum F-H and M-H for every BS for different splits in Figure 3.5-4 was computed from the models in [Lag21]. User traffic was generated following realistic daily patterns and scaled according to [Eri22] to emulate a medium-term scenario with traffic peaks of 60 Gb/s for the whole cell.

With the configuration above, two different RAN operation policies were evaluated: i) *static*, where all µBS are always active and all BSs implement the same functional split option; ii) *dynamic*, where the split is still fixed but capacity is dynamically adapted by switching on/off µBSs according to actual traffic needs.

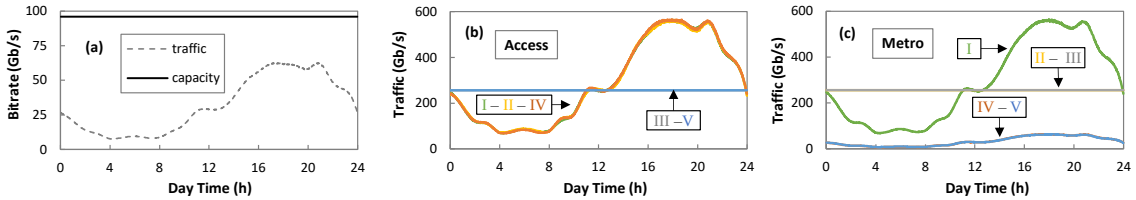

Figure 3.5-5 Static RAN operation.

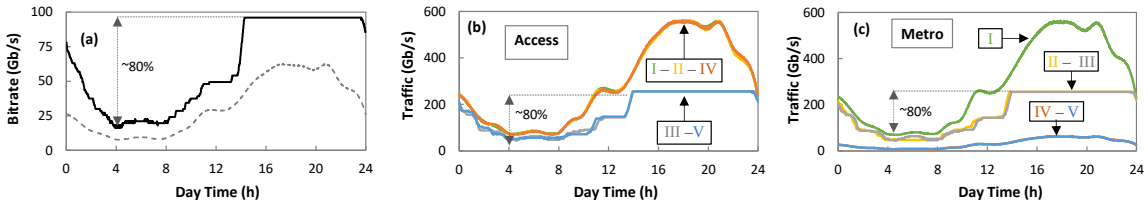

Figure 3.5-6 Dynamic RAN operation.

Figure 3.5-5 shows the performance under static RAN operation policy. Figure 3.5-5 shows an example of one-day total user traffic and the total capacity, i.e., aggregating MBS and active µBSs. Note that the total capacity remains constant at 96 Gb/s and the traffic usage of UEs is fluctuating with the time of day. Under this configuration, Figure 3.5-5(b) and Figure 3.5-5(c) show the traffic at access and metro network, respectively generated with every functional split option. We observe that this policy results in either predictable time-variant traffic (closely correlated with input traffic) or constant traffic, depending on the different functional split options. Additionally, it is worth noting that the traffic volume is dramatically affected by the chosen split, e.g., metro traffic of I and V follow a similar daily pattern but with a largely different magnitude. Moreover, access and metro traffic remain constant in options I and III, whereas drastically vary for the rest of options. In consequence, under key functional splits foreseen for B5G scenarios, metro traffic does not correspond to the aggregated access traffic, which is against the assumptions of typical traffic models and motivates the proposed ones clearly.

Regarding the *dynamic* policy (Figure 3.5-6), we have implemented µBSs switching on/off based on simple threshold-based criteria. Specifically, two rules were implemented at every µBS b: *i*) when the load (input traffic over capacity) of b exceeds 0.6, then the closest to b inactive µBS is switched on; *ii*) when the load of b drops below 0.3 and the closest neighboring µBS is active, b

is switched off. These rules provided committed users QoS (no loss) during the whole simulation. Figure 3.5-6(a) shows that capacity savings up to 80% can be achieved when user traffic is minimum (i.e., only 11 out of 64 µBSs are active). In addition, we observe that those options that provided constant traffic in static operation are sensitive to RAN capacity changes, i.e., options III and V in access (Figure 3.5-6(b)) and II and III in metro (Figure 3.5-6(c)). In fact, traffic reduction in both segments is equivalent to RAN capacity reduction, which is an outstanding feature of those split options, e.g., to minimize optical capacity requirements and reduces energy consumption. This comes at the cost of added unpredictability to access and metro traffic since constant periods are combined with varying periods, which hinders those widely used traffic forecast models based on short-term past windows predictors.

In summary, smart RAN operation in B5G/6G scenarios will induce access and metro network smart operation to implement novel solutions to manage unprecedented variables and sharply changing traffic flows. Autonomous fixed network operation in tight coordination with RAN control is foreseen as a key challenge to achieve target e2e requirements. In this regard, we identify the need of RAN controller to periodically collect user traffic monitoring data gathered from different cells and perform traffic prediction to estimate the expected traffic to be required for the next time interval. Note that this prediction is necessary for deciding which µBSs need to be powered on/off. Then, RAN controller need to be extended with additional modules to perform estimation of the traffic injected in the fixed network, which will depend on both users demand and functional split implemented, as well as on RAN operation approach. That estimation is necessary to allow optical capacity setup, i.e., dynamic allocation of optical SCs based on traffic monitoring and capacity forecasting to be performed autonomously in the optical node agent. This optical capacity update needs to ensure both RAN traffic requirements and local capacity prediction forecasts.

3.6 Low-Nonlinearity-Margin Design of Filterless Horseshoe-and-Spur Networks

Horseshoe topologies are well-suited for resilient hub-and-spoke traffic patterns. Filterless architectures, coupled with coherent-based point-to-multipoint (P2MP) transceivers (using digital-subcarrier-multiplexing, DSCM), offer cost-effective, efficient all-optical aggregation of traffic flows destined for the same hub node. While these technologies hold promise for long-term scalability and resource utilization, network reconfiguration remains a challenge when accommodating dynamic changes like adding a new leaf node. Recent research [Hos24] proposed a scalable horseshoe-and-spur optical network architecture to minimize reconfiguration and operational costs while enabling long-term traffic growth as shown in Figure 3.6-1(a). By decoupling the design of the static horseshoe from the dynamic spurs (trees), the network can adapt to changing traffic demands without disrupting the core infrastructure.

To enhance network performance and reduce operational costs, this work relaxes the stringent nonlinearity constraints that typically limit amplifier gain. By allowing the use of higher-gain amplifiers, we significantly increase the available power budget, thereby decreasing the required number of amplifiers.

To ensure the feasibility of operating with lower margins, we developed a specialized nonlinear noise modeling tool based on the split-step Fourier method (SSFM) considering unequal span/amplifier gain and DSCM (see Figure 3.6-1(b)). This tool is tailored to the unique challenges of this problem, enabling accurate prediction of system performance under nonlinear conditions as a post-analysis.

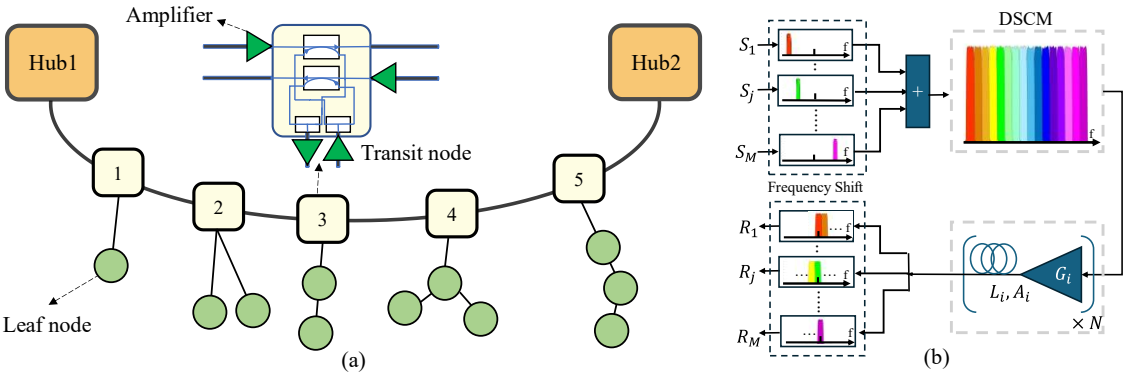

Figure 3.6-1(a) Illustration of a typical horseshoe-and-spur topology and (b) the simulation schematic.

To optimize the network design, we utilize an ILP framework. Numerical simulations based on the Manakov equation and SSFM will be employed to validate the feasibility and the impact of optical nonlinearity on link performance.

3.7 Robust Optimization of Filterless Networks with Physical Layer Uncertainties

Optical network planning and optimization present significant challenges. Traditionally, optical communication systems have relied on conservative design with large margins in key parameters to guarantee acceptable Quality of Transmission over the network's lifetime. While effective in maintaining QoT, this approach often incurs substantial costs.

To address this, recent efforts have focused on improving QoT predictions and optimizing resource allocation, reducing the need for excessive margins. However, these approaches neglect the impact of uncertainties, such as variations in link parameters, which can lead to infeasibility or losing optimality under real operational conditions. Uncertainty can be managed through several strategies. Stochastic optimization leverages probabilistic models to optimize expected outcomes. When precise modeling is challenging, robust optimization offers a more

practical approach. By adopting a worst-case perspective, it seeks solutions that remain feasible across a range of uncertain parameter values within defined uncertainty sets. Sensitivity analysis helps assess the impact of parameter variations on network design and performance.

We employ the robust optimization framework outlined in [Ber03] to adapt the integer linear programming (ILP) model originally proposed in [Hos23] for filterless horseshoe networks as presented in Figure 3.7-1(a). This approach has previously been successfully applied to address traffic uncertainty and failure handling. To the best of our knowledge, this is the first time it has been applied to the design of filterless optical networks.

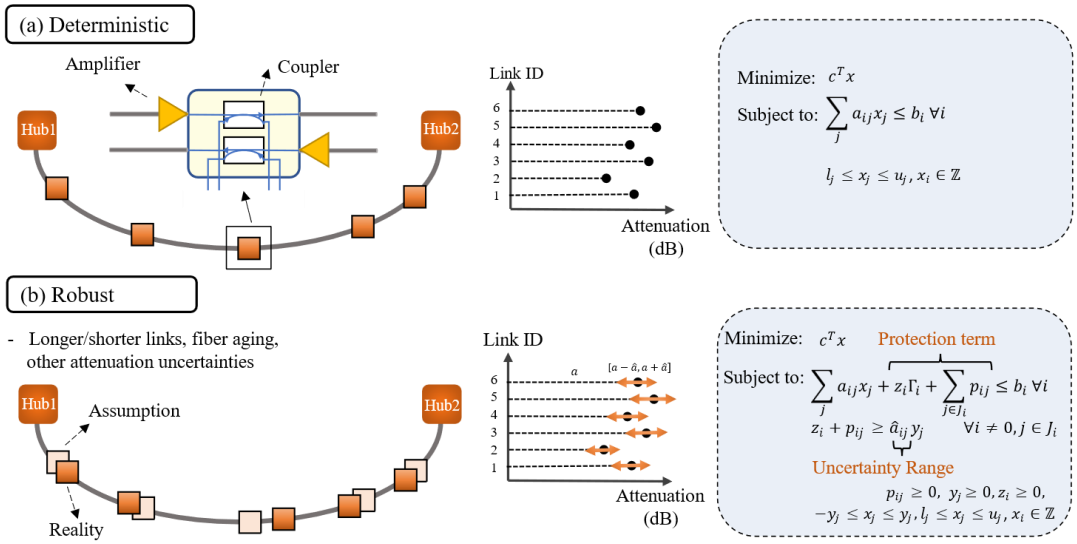

Figure 3.7-1 Horseshoe topology, leaf node architecture and (a) deterministic ILP formulation, and (b) robust ILP formulation in the presence of links attenuation uncertainties.

We propose a robust optimization approach to address uncertainties in link attenuation, which can impact the network's performance. This approach ensures that the network remains feasible under all potential uncertainties, even if it may lead to a less optimal solution. As shown in Figure 3.7-1(b), the robust ILP formulation considers uncertainty in link attenuation coefficients and introduces a protection level to account for different levels of uncertainty. This allows for a balance between robustness and optimality and feasibility.

P2MP transceivers employing dual-polarization 16-QAM modulation were considered in a 400G module with 16 subcarriers (SCs) at 4 GBd. A minimum receiver input power of -24 dBm per SC was set, while the launch power for leaf and hub nodes was fixed at -12 dBm per SC. To ensure a negligible impact of fiber nonlinearities, the launch power threshold was set to -8 dBm per SC, with a maximum allowable SC power difference at the hub's receiver of 8 dB. A total of 100 8-leaf networks were assumed in which all links were composed of single-mode fiber pairs with a loss of 0.24 dB/km and an average length of 12 km. Available coupler ratios included the set of [70/30, 90/10]% and the set of [10/90, 20/80,..., 50/50]% (All). The amplifiers' minimum and maximum gains were set to 10 dB and 20 dB, respectively. We model link attenuation

uncertainty as a uniform distribution with a range of 10% and 15%. Taking 10% as an example, links attenuation could be randomly up to 10% higher or lower than the estimated value.

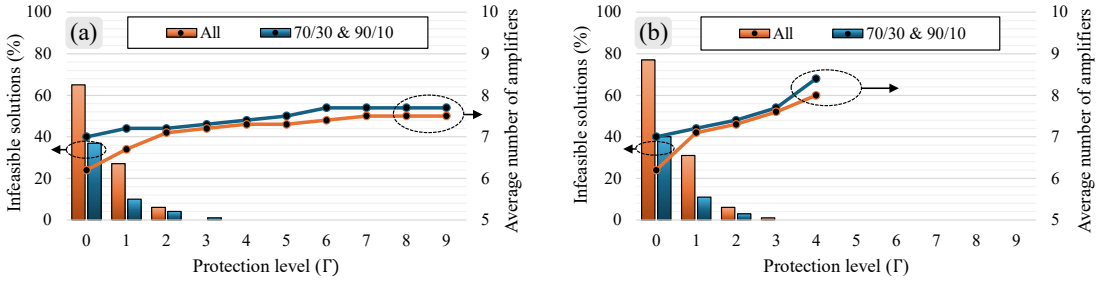

Figure 3.7-2 Infeasible solutions percentage versus the protection level for "All" and "70/30 & 90/10" coupler ratios for (a) 10% and (b) 15% uncertainty ranges.

Figure 3.7-2 shows the infeasible solutions in percentage and the average number of amplifiers obtained by simulating and optimizing 100 networks for “All” and “70/30 & 90/10” coupler ratios when the protection level increases from the minimum of $\Gamma = 0$ to a maximum of $\Gamma = 9$. For each network, we optimize it and then evaluate its performance with randomly changing attenuation values within the defined ranges of uncertainty. If the solution meets all the required conditions, we consider it feasible; otherwise, it is not. Figure 3.7-2(a) assumes 10% uncertainty while Figure Figure 3.7-2(b) considers a 15% uncertainty. The infeasibility rate rapidly decreases as the protection level increases, approaching zero for $\Gamma \geq 4$ (note that we simulated 100 networks, increasing the number of simulations to 1,000 or even 10,000 would allow for a more precise characterization of even the smallest percentages). The average number of amplifiers rises by 1 to 2 amplifiers. The “All” coupler configuration offers a wider range of possibilities and generally leads to better control over power distribution and more optimal outcomes. Nevertheless, the relative advantage over “70/30% & 90/10%” decreases with higher protection levels due to its increased sensitivity to uncertainties in the network. In the case of 15% uncertainty, the robust model cannot generate a feasible solution for $\Gamma \geq 4$. However, given the significantly larger uncertainty range, the likelihood of this worst-case outcome is extremely low and infeasibity rate already is extremely low.

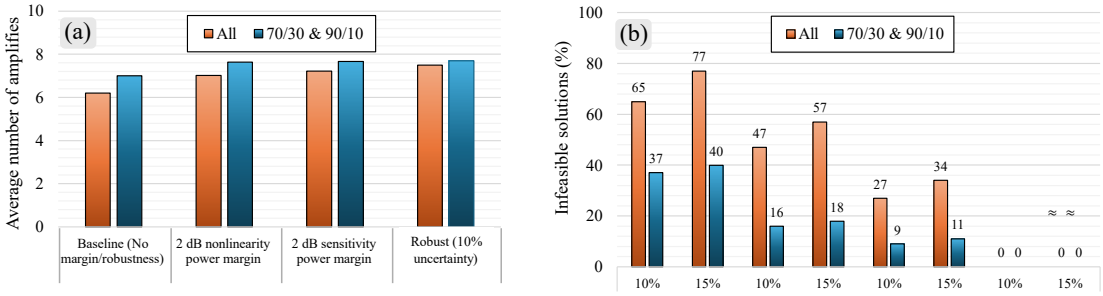

Figure 3.7-3 (a) Average number of amplifiers for four different optimization approaches in the presence of uncertainty and (b) their corresponding infeasible solutions rate.

Figure 3.7-3 compares the robust design approach with the traditional margin-based method. Considering no margin and no robustness (baseline) provides the most optimal solutions in terms of the number of amplifiers (Figure 3.7-3(a)) but the chance of infeasibility is as high as 80% with 15% uncertainty range and "All" coupler ratios (Figure 3.7-3(b)). With a 2-dB nonlinearity power margin or sensitivity power margin, the chance of infeasibility decreases to a minimum of 9% but the number of amplifiers rises to a level offered by the proposed robust approach with zero or near-to-zero infeasibility probability.

4 NOVEL OPTICAL SYSTEMS AND SUBSYSTEMS FOR MBOSDM.

4.1 ULTRA-HIGH-CAPACITY BAND AND SPACE DIVISION MULTIPLEXING BACKBONE EONS: MULTI-CORE VS. MULTI-FIBER

Band Division Multiplexing (BDM) and Space Division Multiplexing (SDM) are advanced techniques aimed at addressing the growing demand for network capacity in optical communication systems. BDM expands the transmission spectrum by utilizing multiple wavelength bands, such as C-, L-, and S-bands, effectively increasing the available bandwidth while optimizing spectral efficiency. This approach enables seamless scaling of network capacity without requiring significant changes to existing fiber infrastructure. On the other hand, SDM focuses on exploiting parallel spatial channels within a single optical fiber, such as multiple cores in multi-core fibers (MCFs) or bundle of multi-fiber pairs (BuMFPs). By leveraging these spatial dimensions, SDM dramatically enhances the overall capacity of the optical system while maintaining high energy efficiency. Together, BDM and SDM present a complementary solution for scaling network capacity in multi-dimensional elastic optical networks, enabling future-proof network architectures that cater to the demands of next-generation applications like 6G and beyond.

Conducting a techno-economic study for emerging technologies is crucial for assessing their viability and guiding their integration into existing networks. Such studies enable operators to evaluate the cost-effectiveness and scalability of new solutions, ensuring a smooth transition that aligns with both performance goals and budgetary constraints. Migration studies play a vital role in this process by identifying challenges and opportunities associated with upgrading from current infrastructure to advanced architectures, such as multi-band and space-division multiplexing systems. To achieve accurate evaluations, a comprehensive understanding of data plane issues and physical layer parameters is essential. For instance, assessing signal quality through metrics like signal-to-noise ratio (SNR) is critical to estimating channel capacity and determining the feasibility of new modulation formats or routing strategies. This granular insight ensures that both the economic and technical dimensions of network evolution are effectively addressed, enabling informed decision-making and optimizing long-term investments.

Therefore, in this section, we present a comprehensive analysis of the physical layer by accounting for NLI and crosstalk impairments in MBoSDM systems, considering real-world multi-core fibers. We propose an accurate SNR calculation model and compare the performance of MCFs against bundled multi-fiber pair solutions, focusing on their impact on overall network capacity.

4.1.1 Nodal Architecture

Figure 4.1-1 illustrates the nodal architecture of BSDM-enabled Elastic Optical Networks (EONs) considered in this study.

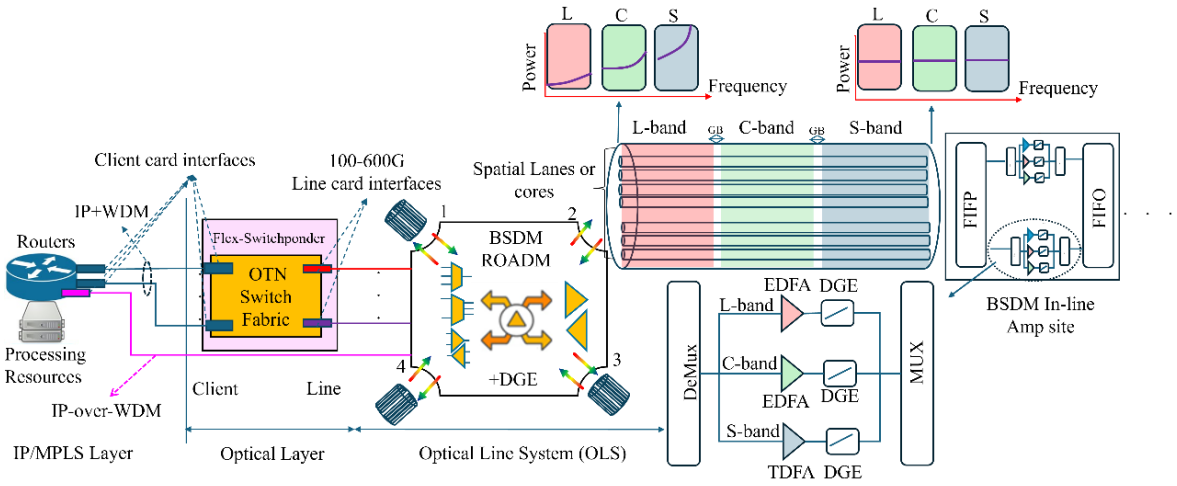

Figure 4.1-1 Architecture of the nodes in MBoSDM EONs.

The network is based on a multi-layer optical transport network (OTN) switching framework over WC-MCFs or bundled multi-fiber pairs, utilizing C+L+S-band technology to provide approximately 20 THz of bandwidth. The modulation format of the line cards is dynamically adapted to the GSNR, as outlined in [Bos19]. Due to the inter-core crosstalk (ICXT) and inter-channel stimulated Raman scattering (ISRS) in BSDM systems, the GSNR for each (channel, core) pair varies, affecting the modulation format and transmission bit rate of each line card. For instance, as shown in Figure 4.1-1, line card bit rates can range from 100 Gbps to 600 Gbps depending on the channel and core assignments. The Internet Protocol/Multiprotocol Label Switching (IP/MPLS) traffic is groomed via the OTN switch matrix and mapped onto idle line cards to construct lightpaths (LPs). Alternatively, an IP-over-WDM approach, bypassing the optical terminal, may also be implemented, as illustrated in Figure 4.1-1. The established LPs are optically switched through a BSDM colorless, directionless, and contentionless (CDC) ROADM and transmitted over WC-MCFs or BuMFPs. For simplicity, we assume that spatial lane (core/fiber) switching is not permitted. The CDC BSDM ROADM is equipped with advanced telemetry modules, including optical channel monitoring (OCM), optical time-domain reflectometer (OTDR), and optical supervisory channel (OSC) [Msa24, Inf21].

While the optimal design for such ROADMs remains an open research area, proof-of-concept architectures have been explored in the literature [Mar17]. The ROADM also incorporates a dynamic gain equalizer (DGE) to equalize launch power, pre-amplifiers, and post-amplifiers. A software-defined networking (SDN) orchestrator oversees routing, modulation format selection, grooming, spectrum assignment, and switching based on the GSNR for each (channel, core) pair.

The in-line amplifier sites in the BSDM system include DGEs and doped fiber amplifiers (DFAs) specific to each band and core. Erbium-doped fiber amplifiers (EDFAs) are used for the C- and L-bands, while thulium-doped fiber amplifiers (TDFAs) amplify signals in the S-band. The DGEs are calibrated using the hyper-accelerated power optimization (HPO) strategy proposed in [Arp24-4]. This approach enhances the capacity of multi-band optical systems by compensating for ISRS effects through optimized power adjustments. By applying higher launch powers to higher-frequency channels more affected by ISRS, a flat optical signal-to-noise ratio (OSNR) is achieved at the end of each span, enabling better network management and service monitoring. While this method optimizes span capacity, it does not aim for a uniform GSNR profile, as a uniform profile may not be optimal for capacity maximization. Additional details on the HPO strategy and its benefits, including accelerated power optimization, can be found in [Arp24-4].

The architecture of in-line amplifier sites is based on the framework discussed in [Fer19], though the application of DGEs depends on the network scale. The schematic diagram of the BSDM CDC ROADM, depicted in Figure 4.1-2, shows a four-degree node with spatial lanes and multiple bands. Each LP is represented by different colors, indicating its destination degree. For instance, the red LP is routed from degree 1 to degree 3 in the L-band of spatial lane 1 (SP1), while the yellow LP is dropped at a left-side line card connected to degree 1. Since neither band nor spatial lane switching is allowed, no additional pass-through LPs can be established at this node.

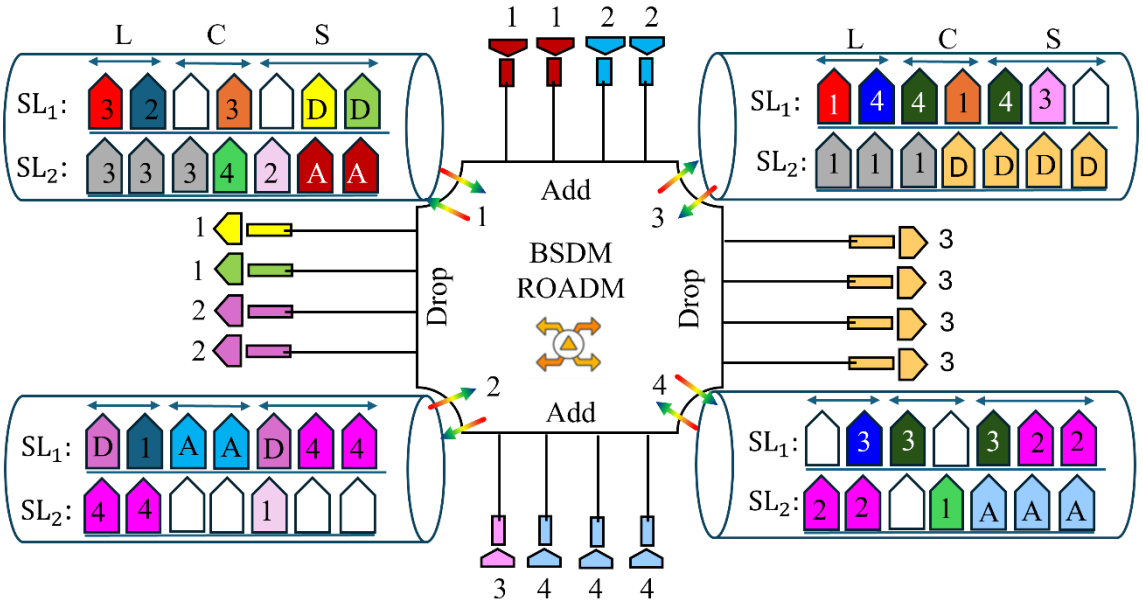

Figure 4.1-2 Band and space division multiplexing (BSDM) colorless, directionless, and contentionless (CDC) reconfigurable add-drop division multiplexing (ROADM).

4.1.2 Physical Layer Modeling for MBoSDM EONs

To mitigate crosstalk and enhance core density in multi-core fibers (MCFs), trench-assisted weakly coupled MCFs (TAWC-MCFs) have been introduced. Figure 4.1-3 provides a

representative cross-sectional view of a fabricated TAWC-MCF with a homogeneous core arrangement. In this design, identical cores with a low-index trench profile are arranged in a hexagonal or square configuration. As shown in the figure, each core is surrounded by a trench area with a lower relative refractive index (Δ_2) compared to the cladding, characterized by a trench width w_{tr}.

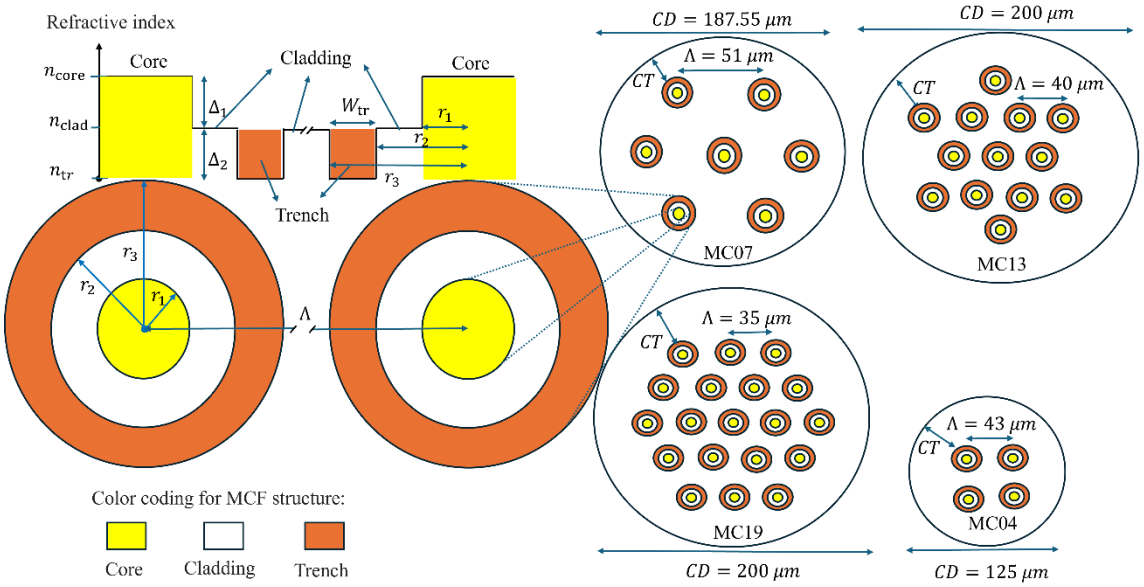

Figure 4.1-3 Trench-assisted weakly coupled multi-core fiber layout, 7-core fiber (MC07) with cladding diameter 187.5 µm, 13-core fiber with cladding diameter 200 µm, 19-core fiber with cladding diameter 200 µm, 4-core fiber with cladding diameter 125 µm.

The inter-core crosstalk (ICXT) in TAWC-MCFs is influenced by fiber parameters such as the relative refractive index difference between the trench and cladding, the trench width, and the core pitch r_1. While ICXT also depends on the optical frequency, this effect is negligible in C-band optical networks. However, as demonstrated later in this study, frequency-dependent ICXT becomes significant in multi-band systems like the C+L+S-band technology analyzed in this work.

In this study, we analyze four different trench-assisted weakly coupled multi-core fiber (TAWC-MCF) variants, each representing state-of-the-art technology: (1) MC04, with four cores and a standard cladding diameter (CD) of 125 µm; (2) MC07, with seven cores and a non-standard CD of 181 µm; (3) MC13, with thirteen cores and a non-standard CD of 225 µm; and (4) MC19, with nineteen cores and a non-standard CD of 225 µm. These MCF types were selected to compare the capacity performance of TAWC-MCFs with standard CD against those with non-standard CD, as well as to evaluate the effect of increasing the number of cores in non-standard CD TAWC-MCFs on network capacity performance. Further analysis and results are presented in Section 4. All TAWC-MCFs used in this study have been fabricated under real-world conditions.

To estimate the inter-core crosstalk of trench-assisted weakly coupled multi-core fibers, several studies in the literature have proposed numerical simulations and experimental measurements [Tek11, Hay12, Hay14]. Additionally, the authors in [Ye14] presented an analytical closed-form

model to calculate the mode coupling coefficient for TAWC-MCFs. Within this framework, the ICXT of a TAWC-MCF can be determined using Eq. 12.

$$\mu_{ICXT}(f^i) = \frac{N_{AC} - N_{AC}\exp[-(N_{AC}+1)\Omega(f^i)L]}{1 + N_{AC}\exp[-(N_{AC}+1)\Omega(f^i)L]} \quad \text{Eq. 12}$$

Furthermore, the power coupling coefficient (PCC), denoted as $\Omega(f^i)$, is given by Eq. 13, where κ, r_b, c, Λ, L, n_{core}, f^i and N_{AC} represent the mode coupling coefficient (MCC), bending radius, propagation velocity, the distance between the centers of two adjacent cores (or core pitch), transmission distance, effective refractive index of the core, channel's center frequency, and the number of lit adjacent cores of the channel under test, respectively.

$$\Omega(f^i) = \frac{c\kappa^2 r_b n_{core}}{\pi f^i \Lambda} \quad \text{Eq. 13}$$

Moreover, the MCC is calculated using Eq. 14, where r_1 is the core radius and the other variables used are given by Eq. 15 to Eq. 19.

$$\kappa(f^i) \cong \frac{\sqrt{\Gamma\Delta_1}}{r_1}\frac{U_1^2(f^i)}{V_1^3(f^i)K_1^2(W_1)}\frac{\sqrt{\pi r_1}}{W_1\Lambda}\exp\left(-\frac{W_1\Lambda + 1.2\left(1+V_1(f^i)\right)w_{tr}}{r_1}\right) \quad \text{Eq. 14}$$

$$\Gamma(f^i) = \frac{W_1}{W_1 + \frac{1.2(1+V_1(f^i)w_{tr})}{\Lambda}} \quad \text{Eq. 15}$$

$$V_1(f^i) = \frac{2\pi f^i r_1 n_{core}\sqrt{2\Delta_1}}{c} \quad \text{Eq. 16}$$

$$K_1(W_1) = \sqrt{\frac{\pi}{2W_1}}e^{-W_1} \quad \text{Eq. 17}$$

$$U_1^2(f^i) = \left[\frac{2\pi f^i r_1}{n_{core}c}\right](n^4 - 1) \quad \text{Eq. 18}$$

$$W_1|_{\frac{\Delta_2}{\Delta_1}} = 1.143V_1(f^i) - 0.22 \quad \text{Eq. 19}$$

The Gaussian-noise (GN) model [Pog14] is utilized to examine the effects of both linear factors, such as loss and chromatic dispersion, and non-linear interference (NLI) effects such as self-phase modulation (SPM), cross-phase modulation (XPM), multi-channel interference (MCI), and ISRS, on the optical signals' amplitude and/or phase modulation as they propagate through an optical fiber medium. Since we have considered the standard single-mode fiber (SSMF) and we are not working in zero or very low fiber dispersion regimes, the MCI is negligible [Ran20]. Consequently, the computation of GSNR (denoted as Γ) for a specific channel i within span s on link l is achieved using Eq. 20 and Eq. 21, where N_s^l represents the number of spans in link l, while N_L denotes the link number of the corresponding lightpath.

$$\Gamma^{l,s,i} \cong \frac{P}{P_{ASE}^{l,s,i} + P_{NLI}^{l,s,i}} \quad \text{Eq. 20}$$

$$P = \begin{cases} P^{l,s+1,i}(z=0);\ if\ s < N_s^l, \\ P^{l+1,1,i}(z=0);\ if\ s < N_s^l, l < N_L, \\ P^{l,s,i}(z=0);\ if\ s < N_s^{N_L}, \end{cases} \quad \text{Eq. 21}$$

Utilizing the incoherent GN model for long enough spans, the value of the overall GSNR for a LP on channel i can be obtained from Eq. 22, where various parameters contribute, such as the power evolution profile (PEP) of each span ($A = P^{l,s,i}(z), 0 < z < L_s^{l,s}$), the length of span s in link l ($L_s^{l,s}$), the noise power caused by the optical amplifier ($P_{ASE}^{l,s,i}$ calculated from Eq. 23), and the noise power stemming from NLI ($P_{NLI}^{l,s,i}$), including SPM, XPM, and ISRS. The details regarding computing ($P_{NLI}^{l,s,i}$) is discussed in the next section.

$$\Gamma_{LP}^{i}|_{dB} = 10\log_2\left[\left(\sum_{l=1}^{N_L}\sum_{s=1}^{N_s^l}\frac{1}{\Gamma^{l,s,i}} + \Pi_{TRx}^{-1}\right)^{-1}\right] - \Pi_{Pen_{fil}}|_{dB} - \Pi_{Pen_{gen}}|_{dB} \quad \text{Eq. 22}$$

$$P_{ASE}^{l,s,i} = n_F h f_i (G^{l,s,i} - 1) R_{sym,i} \quad \text{Eq. 23}$$

In Eq. 23, $n_{F,}, h, f_i, G^{l,s,i}, and\ R_{sym,i}$ are the noise figure of doped fiber amplifier, Plank's coefficient, channel frequency, the gain of DFA, and channel symbol rate, respectively. Additionally, Π_{TRx}, $\Pi_{Pen_{fil}}|_{dB}, and\ \Pi_{Pen_{gen}}|_{dB}$ represent the transceiver SNR, SNR penalty due to wavelength selective switches filtering, and SNR margin due to aging, respectively [Bug22,Seq18,Ped22]. Furthermore, the channel bandwidth ($B_{Ch,i}$) and bit rate of each channel with modulation cardinality m ($R_{ch,(i,m)}$) are calculated from $B_{Ch,i} = \left\lceil \frac{R_{sym,i}(1+\rho_i)}{B_{base}} \right\rceil$, and $R_{ch,(i,m)} = mR_{sym,i}(1+\rho_i)(1-\theta_i)$, respectively. Here, parameters like the symbol rate of the channel ($R_{sym,i}$), the roll-off factor (ρ_i), the forward error correction (FEC) overhead (θ_i), and the bandwidth of a base frequency slot (B_{base}) are involved. Moreover, the GSNR threshold for each modulation format level depends on the pre-FEC bit error rate (BER) and can be determined using (7) in [Arp24-2]. It is assumed that the booster gain at the add and pass-through directions are $G^{l,s}$= 20 dB, and the pre-amplifier can completely compensate for the fiber loss of the link and the QoT degradation caused by ISRS. Thus, for the pre-amplifiers and in-line amplifiers, Eq. 24 can be written, where P (see Eq. 21) and $P^{l,s,i}(z = L_s^{l,s})$ are the powers of channel i just after and before the corresponding amplifier, respectively.

$$G^{l,s,i} = \frac{P}{P^{l,s,i}(z = L_s^{l,s})} \quad \text{Eq. 24}$$

For instance, consider the flat launch power (FLP) mode in span 1, as illustrated in Figure 4.1-1. In other words, based on Eq. 23 and Eq. 24, the $P_{ASE}^{l,s,i}$ depends on the PEP. As shown later in Eq. 30, the PEP is influenced by ISRS, where higher-frequency channels transfer power to lower-

frequency channels. Therefore, the ASE noise is dependent on ISRS through the amplifier's gain profile. In this regard, in-line amplifier (ILA) sites are equipped with DGE to balance the power/gain profile based on the received power at the ILA input and the launch power profile at its output. The DGE could be implemented using wavelength-selective switches (WSS) and variable optical attenuators, which adaptively adjust the power of each wavelength based on the input and output power, as shown in Figure 4.1-1. Finally, to create a practical model for the optical line system penalties, we applied a range of factors: randomly assigning connector losses between 0.2 to 0.5 dB, factoring in ROADMs' polarization dependent loss at 0.5 dB per node along the lightpath, and randomly accounting for splice losses in the range of 0.01 to 0.06 dB/km. The average length of the fusion splicing sections is considered 2 km [Zha23].

Acquiring precise values for all parameters in GSNR calculation is often complex and sometimes unfeasible. Nevertheless, through the application of state-of-the-art telemetry and AI-based approaches [Lun21, Tan21], we can characterize physical layer parameters such as the noise figure of the amplifiers, ROADM's filtering penalty, and SNR_{TRx}. Assuming we possess acceptable knowledge of these physical layer parameters, the most challenging aspect of GSNR estimation for MB-EONs lies in estimating $P_{NLI}^{l,s,i}$ and $P_{ASE}^{l,s,i}$, with the ISRS effects playing a predominant role. However, while the NLI models in the time-frequency domain offer the highest accuracy, they rely on solving complex integrals and are unsuitable for online or offline network planning tools [Pog24]. The computational time needed by models like the split-step Fourier method, integral-based GN model, and enhanced GN model (EGN) is excessively high [Pog17]. Furthermore, they are too complex to adequately account for the add/drop effect modeling in network-wide level studies. Consequently, over the past several years, several closed-form transmission models (CFMs) (e.g., [Sem19]) and semi-CFMs (e.g., [Bug23], [Ran20]) have been developed to estimate NLI. CFMs provide closed-form formulas for PEP and NLI but rely on specific assumptions for each model, e.g., triangular shape for Raman gain profile [Sem19]. If the system model does not align with these assumptions, the model's accuracy diminishes. Semi-CFMs, on the other hand, calculate PEP and loss coefficients using fitting approaches, allowing for flexibility in ignoring certain assumptions. Additionally, the generalized GN model (GGN) is a well-known GN integral-based QoT estimator widely used in DWDM systems, offering acceptable accuracy but lacking modulation format correction terms crucial for MB-EONs [Ami22]. Four fast CFMs have recently surfaced in the literature, as discussed in [Sem19, Uzu21, Sou23, Las23].

The authors of [Sou23] compared the models proposed in [Sem19] and [Uzu21] with the GGN model [Ami22], which is utilized in GNPy [Cur22]. They found that the model presented in [Sem19] demonstrates the highest accuracy for LCS1-band scenarios, particularly when additional correction forms are incorporated. However, their investigation primarily focused on Gaussian-shaped signals. Conversely, the authors of [Jia23] introduced a CFM that considers Raman windowing sweeping across the frequency axis to enhance the accuracy of the model proposed in [Sem19], specifically for LC-band scenarios. Two semi-CFMs introduced in [Ran20] and [Bug23] offer adequate accuracy for EONs beyond 15 THz, i.e., the C+L+S1-band. In this paper, we employ the model in [Pog22], [Ran20] that uses the most advanced techniques, which

is a machine learning (ML)-based GN/EGN model that has been validated through both the split-step Fourier method and experimental testing [Jia23], [Jia23-2]. In addition, it incorporates essential features such as dispersion and modulation format correction terms, striking a fine balance between accuracy and speed. Therefore, $P_{NLI}^{l,s,i}$ is estimated from Eq. 25, where $\psi_{i,j,p,k}$ is computed with Eq. 26 and other variables are defined from Eq. 27 to Eq. 29. With $\delta_{i,j}$ equal to 1 if $i = j$ and 0 otherwise, N_{ch} the number of WDM channels, and ρ_j as the machine-learning-based correction term (see [Pog22] for details).

$$P_{NLI}^{l,s,i} = \frac{16}{17} P_{tx}^{l,s+1,i} \sum_{\substack{1\le j\le N_{ch} \\ 0\le p\le 1 \\ 0\le k\le M \\ 0\le q\le M}} \left[\frac{\rho_j (\gamma_{i,j})^2 (P_{tx}^{l,s+1,j})^2 (2-\delta_{i,j})(-1)^p e^{\left(-\frac{4\alpha_1(f_j)}{\sigma(f_j)}\right)}}{2(R_{sym,i})^2 k!\, q! \left(4\alpha_0(f_j) + (k+q)\sigma(f_j)\overline{\beta}_2(f_j)\right)} \times \left(\frac{2\alpha_1(f_j)}{\sigma(f_j)}\right)^{k+q} \psi_{i,j,p,k} \right] \quad \text{Eq. 25}$$

$$\psi_{i,j,p,k} = \operatorname{asinh}\left[\frac{\pi^2 \overline{\beta}_2(f_j) R_{sym,i}\left(f_j - f_i + (-1)^p\right) \frac{R_{sym,j}}{2}}{2\alpha_0(f_j) + k\alpha(f_j)} \right] \quad \text{Eq. 26}$$

$$\gamma_{i,j} = \frac{2\pi f_i}{c} \frac{2n_2}{A_{eff}(f_i) + A_{eff}(f_j)} \quad \text{Eq. 27}$$

$$\overline{\beta}_2(f_j) = \beta_2 + \pi\beta_3(f_i + f_j - 2f_0) + \frac{2\pi^2}{3} \times \beta_4[(f_i - f_0)^2 + (f_i - f_0)(f_j - f_0) + (f_i - f_0)^2] \quad \text{Eq. 28}$$

$$M = MAX\left[10 \times \left|\frac{2\alpha_1(f_j)}{\sigma(f_j)}\right|\right] + 1 \quad \text{Eq. 29}$$

To estimate the $\Gamma^{l,s,i}$ of each span, we follow the methodologies outlined in [Pog22], utilizing from Eq. 20 to Eq. 29. The process involves the following steps:

Step 1: Numerically calculate the PEP by solving a system of coupled differential equations, i.e., Eq. 30. This calculation requires the launch power profile, the fiber loss coefficient profile, and the ISRS gain profile function. Notably, the ISRS gain depends on factors such as the pump channel frequency, the frequency difference between pump and signal channels, and fiber parameters like effective area, dispersion coefficient, and numerical aperture.

$$\frac{\partial P_{tx}^{l,s,i}(z)}{\partial z} = \kappa P_{tx}^{l,s,i}(z) \left[\sum_{\forall j \in C} \xi\left(\frac{f_i}{f_j}\right) C_r\left(f_j, f_j - f_i\right) P\left(f_j, z\right) - \alpha(f_i) \right], \forall i \in C \quad \text{Eq. 30}$$

Step 2: Estimate auxiliary loss coefficient profiles, i.e., $\alpha_0(f)$, $\alpha_1(f)$, and $\sigma(f)$ by fitting the power evolution profile obtained in Step 1 to the approximately closed-form formula (equation (13) in [Ran20]). The frequency-dependent fiber loss can be loosely modeled by Eq. 31, where z is the signal propagation distance, and the index i represents the channel's frequency f_i.

$$\alpha(z, f_i) = \alpha_0(f_i) + \alpha_1(f_i) \exp\{\sigma(f_i)z\} \quad \text{Eq. 31}$$

This model indicates that the observed loss coefficient in MB systems differs from the loss coefficient used in C-band systems. In this context:

- $\alpha_0(f_i)$: Fiber loss without ISRS.
- $\alpha_1(f_i)$: Loss modification due to ISRS at the span's onset.
- $\sigma(f_i)$: rate at which ISRS diminishes along the span with decreasing optical power.

Once these parameters are assigned, the NLI calculation becomes closed form. However, assigning auxiliary loss coefficient profiles remains semi-closed form to avoid excessive errors. Equations (30.1) and (30.2) in [Ran20] provide a closed-form best fit for $\alpha_1(f_i)$ and $\alpha_0(f_i)$ given $\sigma(f_i)$. Optimizing $\sigma(f_i)$ numerically ensures the best fit for all parameters. For illustration, Figure 4.1-4 shows the observed loss for a 70 km span in a fully loaded link with a flat launch power of 0 dBm. The results, based on parameters outlined in this section, highlight differences between the observed and expected loss curves due to ISRS effects in MB-EONs. These differences become more pronounced as additional bands are introduced.

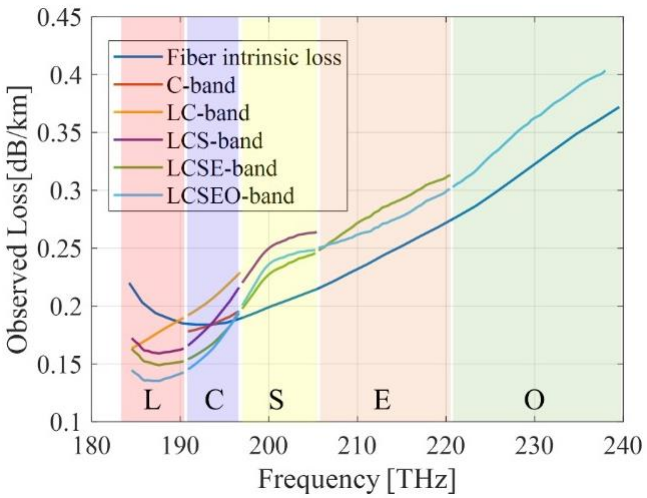

Figure 4.1-4 ISRS effect on the fiber intrinsic loss for different multi-band systems. Span length = 70 km, launch power = 0 dBm, Fiber type: standard single mode fiber zero-peak water.

Step 3: Calculate $G^{l,s,i} = \frac{P}{P^{l,s,i}(z=L_s^{l,s})}$ to derive $P_{ASE}^{l,s,i}$.

Step 4: Compute the parameter M (see Eq. 29).

Dissemination Level	SEN (Sensitive - limited under the conditions of the Grant Agreement)

Step 5: Determine the effective dispersion profile (see Eq. 28). Here, f_0 denotes the frequency reference corresponding to the wavelength 1550 nm, and β_2, β_3 and β_4 are measured values.

Step 6: Establish the frequency-dependent non-linearity coefficient ($\gamma_{i,j}$). This involves the nonlinear Kerr refractive index (n_2) and effective area ($A_{eff}(f_i)$) (see Eq. 27).

Step 7: Finally, calculate $P_{NLI}^{l,s,i}$ from Eq. 25.

By substituting $P_{NLI}^{l,s,i}$ and $P_{ASE}^{l,s,i}$ for each span into a Light Path (LP), the total end-to-end GSNR can be calculated using Eq. 22. This ensures that ISRS effects on ASE, NLI, and the loss coefficient, as represented from Eq. 20 to Eq. 29, are accurately accounted for.

To calculate the power of ICXT caused by the coupling of adjacent cores in MCFs, Eq. 32 can be used, where $P_{ICXT}^{s,i}$ represents the ICXT power, $\mu_{ICXT}^{s,i}$is the ICXT coefficient, and $P_{xt}^{s+1,i}$ is the transmitted power from the adjacent core.

$$P_{ICXT}^{s,i} = \mu_{ICXT}^{s,i} P_{xt}^{s+1,i} \quad \text{Eq. 32}$$

A MBoSDM-EON over MCFs does not require MIMO-DSP-equipped transceivers if the accumulated ICXT penalty on the SNR is ≤1 dB [Hay14, Win13, Sak13]. The ICXT threshold for each modulation format, based on the acceptable bit error rate (BER) and the corresponding GSNR threshold (G_{th}) in dB, can be calculated using Eq. 33. Here, $\mu_{ICXT_{th}}^{m}$ represents the acceptable ICXT threshold for modulation format m, Γ equals 1 dB denotes the acceptable QoT penalty, and χ^m= [0.5,1,3.41,5,10,21] [Hay14].

$$\mu_{ICXT_{th}}^{m} = 10log_2\left(\frac{1-10^{(\frac{-\Gamma}{10})}}{\chi^m \times 10^{(\frac{G_{th}}{10})}}\right) \quad \text{Eq. 33}$$

4.1.3 Simulation Setup and Numerical Results

Initially, we present a study on the TAWC-MCFs. Subsequently, we analyze the network performance for the two SDM scenarios, i.e., MCFs and BuMFPs.

4.1.3.1 ICXT Analysis in BSDM EONs

As shown in Figure 4.1-3, four real-world TAWC-MCFs are considered for the BSDM EON: MC04, MC07, MC13, and MC19. Additionally, standard single-mode fibers (SSMFs) are employed in the BuMFPs strategy. The physical parameters of the optical fibers are listed in Table 4.1-1. These MCFs have been selected as they are currently manufactured and represent state-of-the-art technology in their respective categories. For instance, among the standard CD TAWC-MCFs, the four-core lattice design is considered optimal for minimizing ICXT. Regarding non-standard TAWC-MCFs, hexagonal close-packed MCFs have demonstrated better efficiency due to their higher core density and reduced ICXT. Accordingly, MC07, introduced in [Hay12], has been

adopted for its low ICXT. Furthermore, MC13 and MC19 are based on the MCF designs proposed in [Sai13] and [Sak13], respectively. Unlike previous studies in the literature, our analysis incorporates frequency-dependent values for parameters such as the loss coefficient, effective area, and effective dispersion coefficient. This approach ensures that both the GSNR and ICXT of each channel are frequency dependent. Recent advancements in MCF manufacturing focus on developing ultra-low ICXT and low-loss fibers capable of operating across multiple bands, from the C-band to the L-band [Hay19]. The primary motivation for implementing ultra-low ICXT and low-loss TAWC-MCFs, especially in long-haul networks, is to enhance transmission bit rates while reducing network planning complexity.

In the ultra-low ICXT and low-loss regime, the ICXT across all channels and cores remains below the threshold for the highest modulation format (i.e., 64QAM) over long distances (up to 10,000 km), with a loss coefficient lower than that of SSMFs [Hay19]. To illustrate this, we analyze ICXT in terms of the power coupling coefficient and mode coupling coefficient as functions of the trench width-to-core radius ratio. Figure 4.1-5(a) shows the PCC as a function of frequency across the C+L+S bands, calculated using Eq. 13. It is evident from Figure 4.1-5 that the PCC varies significantly with frequency. Hence, assuming a single value for PCC at 1550 nm in a multi-band system oversimplifies the analysis and may result in inaccuracies. Furthermore, the ICXT is influenced by the trench width-to-core radius ratio (w_{tr}/r_1).

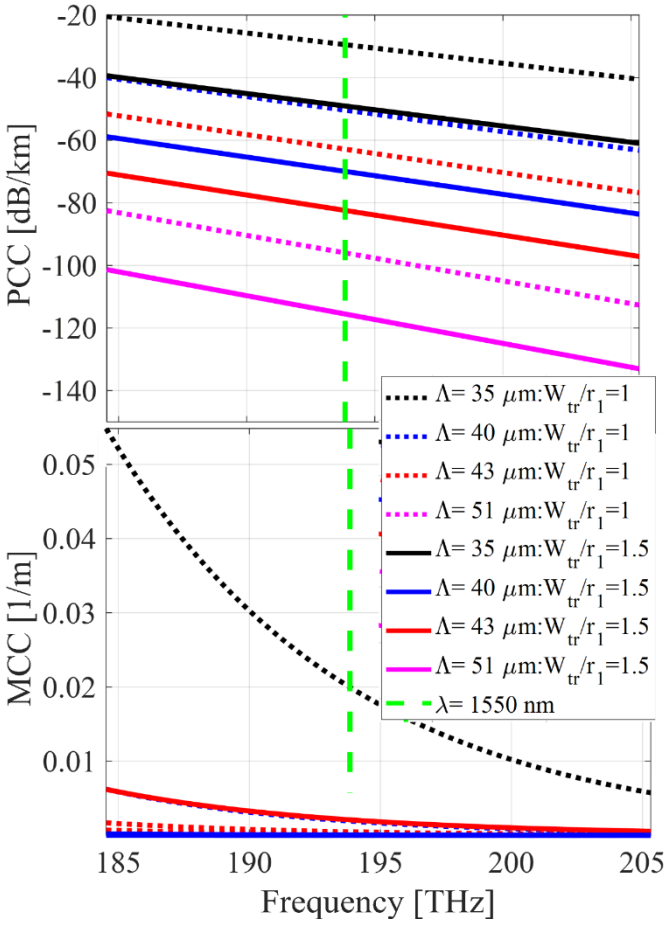

Figure 4.1-5 (a) Power coupling coefficient (PCC) and (b) mode coupling coefficient (MCC) versus frequency for different values of the ratio of trench width to core radius, i.e., wtr/r1 for four-core MCF (MC04) with Λ =43 μm, seven-core MCF (MC07) with Λ = 51 μm, thirteen-core MCF (MC13) with Λ = 40 μm, and nineteen-core MCF (MC19) with Λ = 35 μm.

An increase in this ratio reduces the ICXT, but it cannot be increased indefinitely. The distance between adjacent trenches must be less than 3 μm [Tak11]. Based on Figure 4.1-1, this constraint allows us to derive Eq. 34.

$$R_{tr} \leq \frac{\Lambda - 3}{2r_1} - 2 \qquad \text{Eq. 34}$$

For instance, in the case of MC19, the trench width-to-core radius ratio (w_{tr}/r_1) cannot exceed 1.5. To ensure a fair comparison, we adopt w_{tr}/r_1 = 1.5 for the remainder of this paper. As expected, the PCC of MC19 is higher than that of other MCFs due to its smaller core pitch. Specifically, the ICXT of MC19 is 22 dB/km higher than MC13, 34 dB/km higher than MC04, and 55 dB/km higher than MC07, corresponding to core pitch differences of 5 μm, 8 μm, and 16 μm, respectively. Increasing the trench width-to-core radius ratio (R_{tr}) by 50% results in an approximate 20 dB reduction in ICXT. The MCC values for various w_{tr}/r_1 ratios, calculated using Eq. 14, are shown in Figure 4.1-5(b). The results indicate that increasing w_{tr}/r_1 from 1 to 1.5 in MC19 leads to a significant reduction in MCC. However, further increases in w_{tr}/r_1 beyond 1.5 have negligible impact. For the other MCFs, variations in w_{tr}/r_1 do not substantially affect the

MCC. As previously discussed, in the ultra-low ICXT and loss regime, the ICXT for all (connection, channel, core) tuples must remain below the crosstalk threshold of the highest modulation format level in the network, i.e., $\mu_{ICXT_{th}}^{m=6} > \mu_{ICXT}^{s,i}$. According to Eq. 33, the crosstalk thresholds $\mu_{ICXT_{th}}^{m=6}$ for different modulation formats are as follows: -10.58 dB, -13.59 dB, -18.93 dB, -20.58 dB, -23.59 dB, and -26.82 dB for m = 1-6, corresponding to GMI values from 2 to 12 related to the m=1-6 (see Figure 4.1-6). These values correspond to the pre-forward error correction (FEC) bit error rate (BER) of 1.5×10^{-2} and a quality of transmission (QoT) penalty $\Gamma = 1$ dB. The soft decision FEC with a maximum overhead of 20%–30% is employed [Bos19]. Additionally, the GSNR threshold for each modulation format level m is determined by the pre-FEC BER and can be obtained from Eq. (7) in [Arp24-2]. The GSNR thresholds are 3.71 dB, 6.72 dB, 10.84 dB, 13.24 dB, 16.16 dB, and 19.01 dB for the pre-FEC BER of 1.5×10^{-2}. The ICXT, calculated using Eq. 12, is simulated for transmission distances ranging from 500 km to 9,000 km, using the parameters listed in Table 4.1-1. The results, presented in Figure 4.1-6, lead to several key observations.

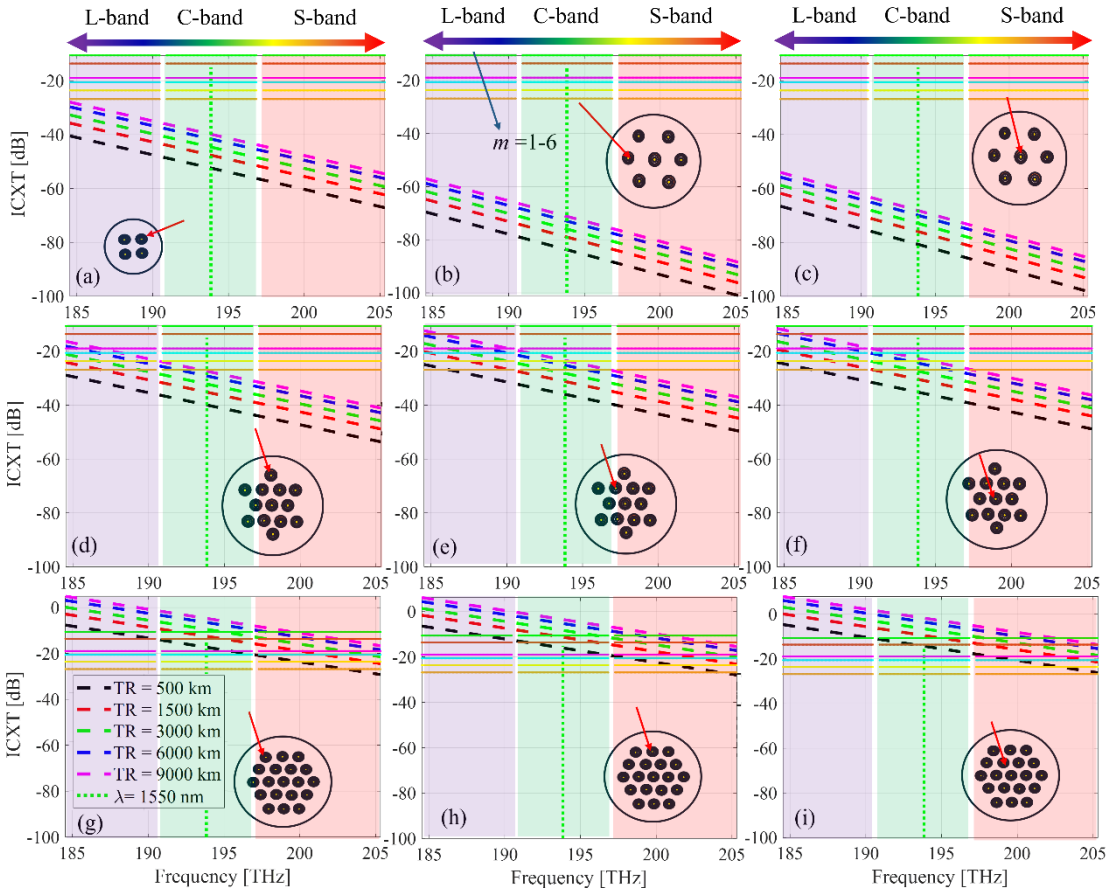

Figure 4.1-6 Inter-core crosstalk (ICXT) for: (a) MC04; (b)-(c) MC07; (d)-(f) MC13; and (g)-(i) MC19 over transmission reaches of 500 km to 9000 km.

Firstly, the ICXT of a channel is influenced not only by the transmission distance but also by factors such as frequency, the physical configuration of the MCF, the number of neighboring cores, and the core pitch. For instance, consider MC04 with a core pitch of 43 µm, as shown in

Figure 4.1-6(a). Each core in MC04 has two neighboring cores, making it an ultra-low ICXT MCF. However, from Figure 4.1-6(a) and Figure 4.1-5(a), it is clear that with wtr/r1= 1, MC04 does not qualify as an ultra-low ICXT MCF. Despite this, the ICXT in MC07 cores is lower than in MC04 (see Figure 4.1-6(b) and (c)). While MC07 features two types of cores—inner ones with six neighbors and outer ones with three neighbors—the primary determinant of ICXT is the core pitch, which is set at 51 µm in MC07. Thus, MC07 qualifies as an ultra-low ICXT MCF. Both MC04 and MC07 are also ultra-low loss MCFs, with loss coefficients lower than those of standard single-mode fibers (SSMFs), as reported in [Tak20] and [Hay12].

Table 4.1-1 Physical parameters of the optical fibers.

Parameter	Symbol	MC04	MC07	MC13	MC19	SSMF
Core counts	n_c	4	7	13	19	1
Cladding diameter [µm]	CD	125	187.5	200	200	125
Cladding thickness [µm]	CT	40	40	35	30	40
Core radius [µm]	r_1	4.5	4.5	4.1	3.6	9
Core-trench radius	r_2	$2r_1$	$2r_1$	$2r_1$	$2r_1$	-
Trench's width	w_{tr}	(1, 1.5) r_1	(1, 1.5) r_1	(1, 1.5) r_1	(1, 1.5) r_1	-
Effective area	A_{eff} (f^i)	[Tak20]	[Hay12]	[Sai13]	[Sak13]	[Pog22]
Loss coefficient	$\alpha(f^i)$	[Tak20]	[Hay12]	[Sai13]	[Sak13]	[Pog22]
Effective dispersion coefficient	β_{eff} (f^i)	[Tak20]	[Hay12]	[Sai13]	[Sak13]	[Pog22]
Core pitch [µm]	Λ	43	51	40	35	-
Core's refractive index	n_{core}	1.44	1.44	1.44	1.44	1.44
Bending radius [mm]	r_b	144	144	140	140	140

Increasing the core count from 7 to 13 results in an increase in ICXT due to the reduction in core pitch. Figure 4.1-6(d)-(f) show the variation in ICXT for MC13, which, as observed, does not qualify as an ultra-low ICXT MCF. For certain (channel, core) pairs, particularly those in the L-band and the lower frequencies of the C-band, the modulation format level may need to be reduced to $m = 6$ in some transmission scenarios. This results not only in a decrease in transmission bit rate but also in more complex service provisioning, especially in ICXT-aware planning strategies. In the worst-case scenario, i.e., the lowest frequency with the highest transmission reach, certain (channel, core) pairs may only support data transmission with $m = 1$. However, this situation does not occur for MC19. Indeed, Figure 4.1-6(g)-(i) show that by increasing the number of cores and reducing the core pitch to 35 µm in MC19, data transmission becomes impractical for certain (channel, core) pairs at higher transmission reaches, particularly in most of the C- and L-band resources. This challenge is exacerbated as core pitch decreases. This challenge is more pronounced for (channel, core) pairs in the L-band. Therefore, MCFs with core pitch lower than 43 µm are not good candidate for the MBoSDM EONs such as MC13 and MC19.

4.1.3.2 Comparison of Metro-Core Backbone Networks Performance: MCFs vs. BuMFPs

In this section, we evaluate two BSDM strategies, namely MCFs and BuMFPs. Inspired by previous discussions, the focus is on TAWC-MCFs. Three networks (see Figure 4.1-7) of varying sizes are considered for this study:

USB6014: The United States of America backbone network consists of 60 nodes and 79 links. It emphasizes traffic exchange among 14 core nodes (Figure 4.1-7). The remaining nodes are equipped with optical cross-connects, with add/drop functionality restricted to the core nodes. Key network parameters include:

- Average nodal degree: 2.63
- Average link distance: 447 km
- Maximum lightpath (LP) distance for the k=5 shortest paths: 6,493 km

SPNB3014: The Spanish backbone network comprises 30 nodes and 56 links. Key parameters are:

- Average nodal degree: 3.73
- Average link distance: 148.5 km
- Maximum LP distance for the k=10 shortest paths: 1,044 km

JPNB4812: The Japanese backbone network includes 48 nodes and 56 links. Key parameters are:

- Average nodal degree: 3.41
- Average link distance: 153.7 km
- Maximum LP distance for the k=10 shortest paths: 2,292 km

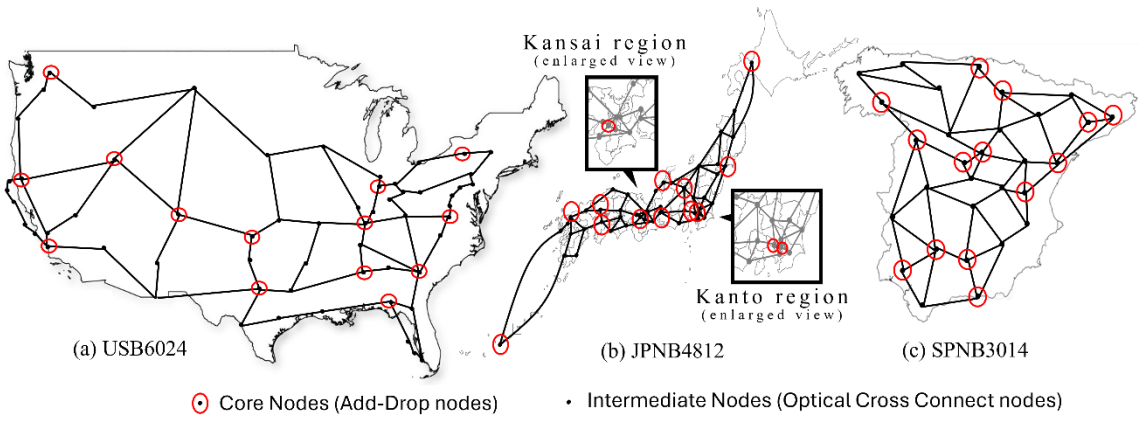

Figure 4.1-7 Network topology of (a) United State backbone (USB6014), (b) Japan backbone (JPN4812), and (c) Spanish backbone (SPNB3014).

Dissemination Level	SEN (Sensitive - limited under the conditions of the Grant Agreement)

For USB6014, the transmission bit rates were calculated for all tuples of (connection, channel, core) across the C+L+S-band, utilizing 268 channels with a bandwidth of 75 GHz each. This analysis spans 92 connections within the network. Key assumptions and parameters include:

- **Maximum span length**: 100 km per link
- **Symbol rate per channel**: 64 GBd
- **Transmission bit rates**: Varying between 100 Gbps and 600 Gbps, based on the GSNR of each channel, calculated using Eq. 20 for the k=1 shortest path of each connection
- **DFA amplifier noise figures**:
  - C-band: 4.5 dB
  - L-band: 5 dB
  - S-band: 6 dB
- **Launch power**: Optimized using the hyper-accelerated scheme introduced in [Arp24-4].

The modulation format profiles for all tuples of (connection, channel, core) are shown in Figure 4.1-8 and Figure 4.1-9 for BuMFP-based and MCF-based BSDM, respectively. The modulation format is determined by Eq. 35, where m_{GSNR} is the modulation format level satisfying the GSNR threshold and $m_{ICXT-1dB}$ is the modulation format satisfying the ICXT threshold with a 1 dB penalty.

$$min\{m_{GSNR}, m_{ICXT-1dB}\} \quad \text{Eq. 35}$$

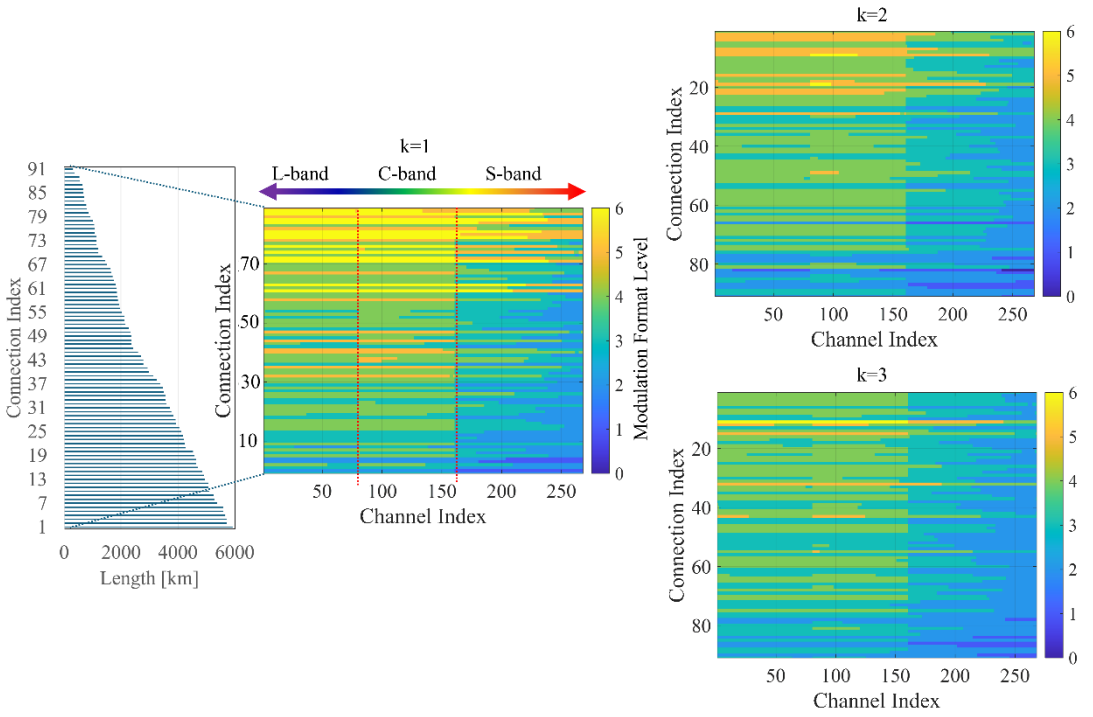

Figure 4.1-8 Modulation format level profile (right), and the connection length (left) for USB6014 in the BuMFP scenario and k=1,2, and 3.

Dissemination Level	SEN (Sensitive - limited under the conditions of the Grant Agreement)

The comparison between Figure 4.1-8 and Figure 4.1-9 shows that MC04 and MC07, with lower loss coefficients, achieve higher modulation format levels.

The GSNR profiles for all connections in the three backbone networks were pre-calculated, considering k=5 for USB6014 (due to its longer distances) and k=10 for SPNB3014 and JPNB4812. Due to space constraints, only the results for USB6014 with k=1 are reported here. The complete dataset, including GSNR profiles for all k values, is publicly available in [Arp24-3] for further research.

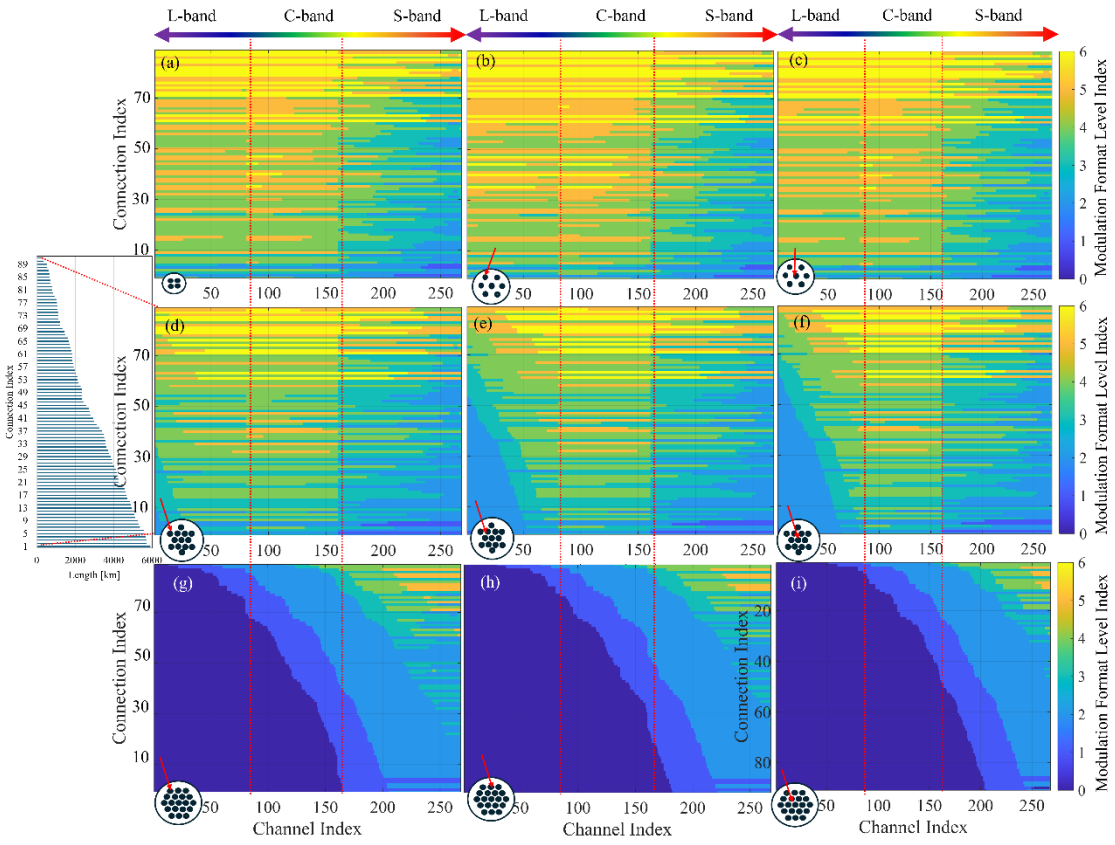

Figure 4.1-9 Modulation format level profile for USB6014 in the MCF-based scenario: (a) MC04, (b)/(c) MC07, for cores with 3/6 adjacent neighbors, (d)/(e)/(f) MC13, for cores with 2/5/6 adjacent neighbors, (g)/(h)/(i) MC19, for cores with 3/4/6 adjacent neigh bours.

The results reveal that the loss coefficient plays a more significant role than the low ICXT, particularly in the C- and L-bands. Increasing the core pitch results in higher modulation format levels and bit rates, as observed in the performance of MC07 compared to other configurations. Moreover, the influence of core pitch outweighs that of the number of adjacent cores. For instance, a comparison of Figure 4.1-9(b) and Figure 4.1-9(c) with Figure 4.1-9(a) highlights this dominance. Reducing the core pitch in MC13 leads to lower modulation format levels, which decreases the capacity per core, as shown in Figure 4.1-9(d)–(f). This effect is even more pronounced in MC19, where the modulation format level index becomes zero. This indicates no

feasible modulation format can be selected, rendering most C- and L-band channels practically unusable (see Figure 4.1-9(g)–(i)).

To provide deeper insights into the capacity performance of MCF-based and BuMFP-based BSDM, Figure 4.1-10 illustrates the cumulative throughput of each connection in both scenarios. The results show that ultra-low ICXT and low-loss TAWC-MCFs outperform the BuMFPs. The difference is particularly noticeable when comparing MC04 with MF04 (a BuMFP with 4 SSMF pairs) and MC07 with MF07 (a BuMFP with 7 SSMF pairs). This is attributable to the lower loss coefficients of state-of-the-art ultra-low ICXT and low-loss MC04 and MC07. The extent of this performance difference depends on the transmission reach and the number of hops per connection. Increasing the number of cores and decreasing the core pitch enhances the performance of BuMFP-based BSDM. However, the loss coefficients of MC13 and MC19 are not lower than those of SSMFs due to their reduced cladding thickness. While throughput degradation in MC13 is relatively minor, thanks to its 40 µm core pitch, the degradation is significant for MC19, where the core pitch is 35 µm, leading to higher ICXT.

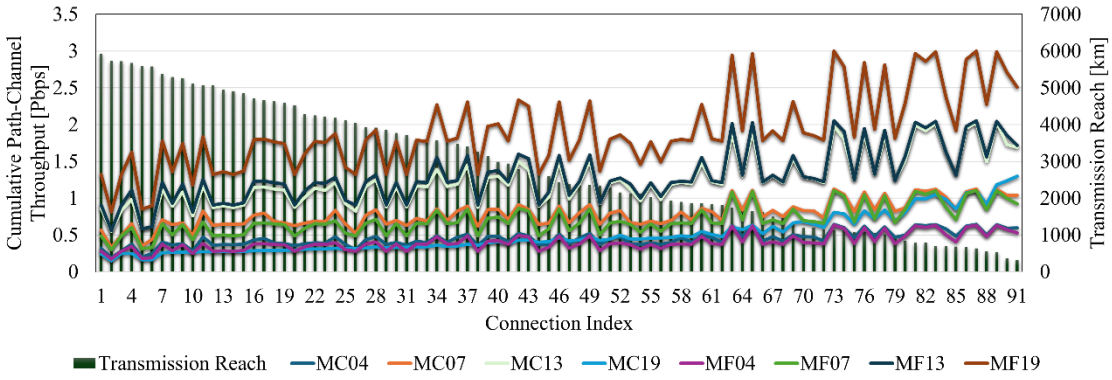

Figure 4.1-10 Cumulative (channel-core) throughput [Pbps] in terms of the connections in USB6014 for both BSDM scenarios, i.e., MCF-based (MC04,07,13,19) and BuMFPs-based MF04,07,13,19).

Simulation results for JPNB4812 and SPNB3014, while not included here due to space constraints, exhibit similar behavior to the USB6014 results shown in Figure 4.1-8, Figure 4.1-9 and Figure 4.1-10. The average bit rates per channel for JPNB4812 and SPNB3014 are higher than those for USB6014, attributed to the longer-distance connections in the US network. In the case of MC19, the number of unfeasible L-band channels for SPNB3014 is lower than for JPNB4812, and for both networks, it is lower than for USB6014. The total network capacity for the three topologies is depicted in Figure 4.1-11. The results show a consistent trend across all networks:

- Increasing the number of cores from 4 to 13 leads to a linear increase in network capacity.
- For higher core counts, capacity decreases significantly due to increased ICXT.

For USB6014, MC04 and MC07 exhibit 11% and 14% higher total capacity compared to MF04 and MF07, respectively. In contrast, for MC13 and MC19, the total capacity is 4%|73% lower than MF13|MF19, respectively. Similar trends are observed for JPNB4812 (2%|60%) and

SPNB3014 (1%|55%). For scenarios with a core pitch exceeding 40 µm, MCF-based approaches are comparable to BuMFPs. However, such configurations increase network planning complexity, necessitating ICXT-aware service provisioning (see Figure 4.1-6). Conversely, in ultra-low ICXT scenarios with a core pitch exceeding 43 µm, modulation format levels for all (connection, channel, core) tuples are independent of ICXT. In such cases, ultra-low ICXT and loss ensure all tuples are feasible for data transmission, with the transmission dependent only on GSNR thresholds, enabling MIMO-free transmission. The combination of ultra-low ICXT and loss positions MCFs as a promising candidate for next-generation BSDM backbone elastic optical networks. By mitigating ICXT penalties and ensuring high GSNR, MCFs provide robust and efficient solutions for data transmission across multiple bands.

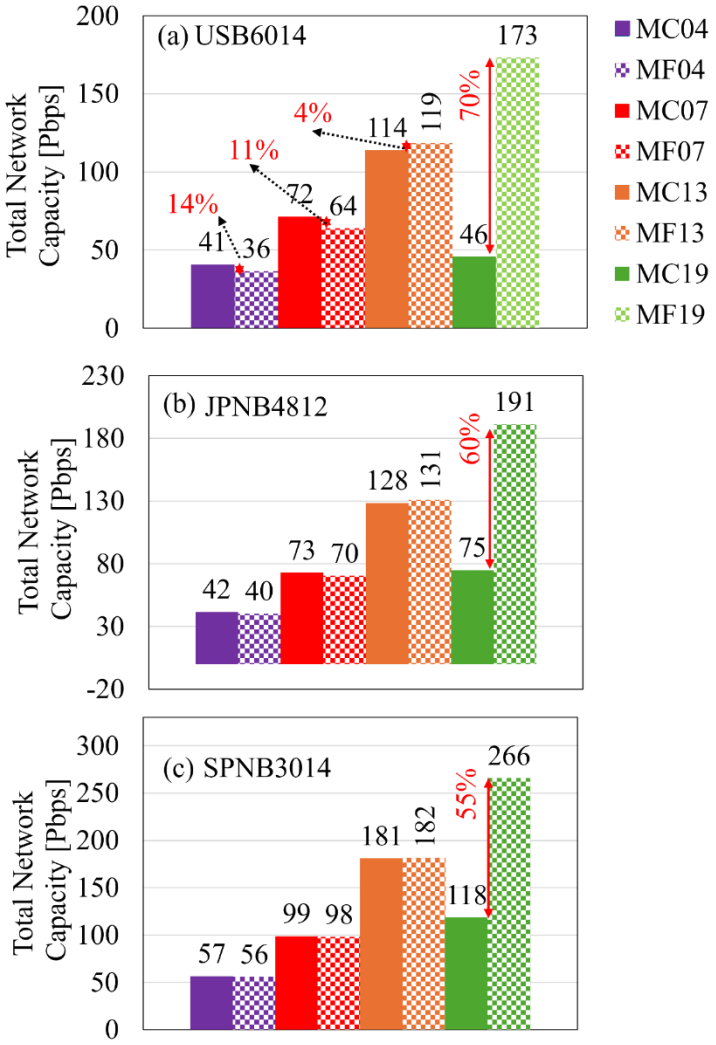

Figure 4.1-11 Total network capacity [Pbps] in (a) USB6014, (b) JPNB4812, (c) SPNB3014 for both BSDM scenarios, i.e., MCF-based (MC04, 07, 13, 19) and BuMFPs-based (MF04, 07, 13, 19).

In conclusion, we have demonstrated that MCF-based MBoSDM-EONs, operating in the ultra-low inter-core crosstalk (UL-ICXT) and low-loss regime, can achieve up to 14% greater network throughput compared to bundled multi-fiber pairs (BuMFPs). By carefully designing the physical

structure of TAWC-MCFs, it is feasible to achieve comparable total network capacity to BuMFPs, even with thirteen cores and a core pitch of 40 µm. Our results indicate that increasing the number of cores beyond thirteen with limited cladding diameters significantly reduces the total network capacity compared to BuMFPs. Furthermore, we found that the L-band is not a favorable option for core pitches below 43 µm, even in smaller networks like the Spain backbone. In contrast, the C+S-band combination demonstrates greater potential for next-generation BSDM EONs. Overall, TAWC-MCFs with core pitches exceeding 40 µm exhibit promising performance and represent a viable alternative to BuMFPs in broadband optical communication systems. Finally, future research should include comprehensive techno-economic studies to identify the optimal strategies for upgrading or deploying new optical networks. These studies should consider both ultra-low-loss SMFs and ultra-low-loss ICXT MCFs, as MCF technology continues to evolve.

4.2 Channel-based ICXT and NLI-Aware Service Provisioning for Multi-band Over Space Division Multiplexed Optical Networks

In this section, we highlight two major service provisioning approaches within MBoSDM systems: Core-Spectrum-Band (CSB) and Band-Spectrum-Core (BSC). These approaches are evaluated based on blocking probability, average GSNR, and lightpath distance, with specific results presented for 4-core MCFs (Multi-Core Fibers) with a standard cladding diameter.

Moreover, contrary to the distance-adaptive approach, which considers the worst-case channel based on GSNR and calculates the maximum reach distance for each modulation format using that value, we adopt a channel-based approach for modulation format selection. This method allows for more efficient resource utilization by dynamically selecting the modulation format for each channel based on its individual GSNR. Figure 4.2-1 provides an illustrative explanation of the BSC and CSB approaches. In the CSB approach, service provisioning starts with the C-band, as it is the conventional band widely used in legacy networks. We assume that the existing optical spectrum primarily utilizes this portion. If no space is available to establish a new lightpath within the C-band of a core, the control plane selects C-band channels in another core until all C-band channels are fully occupied.

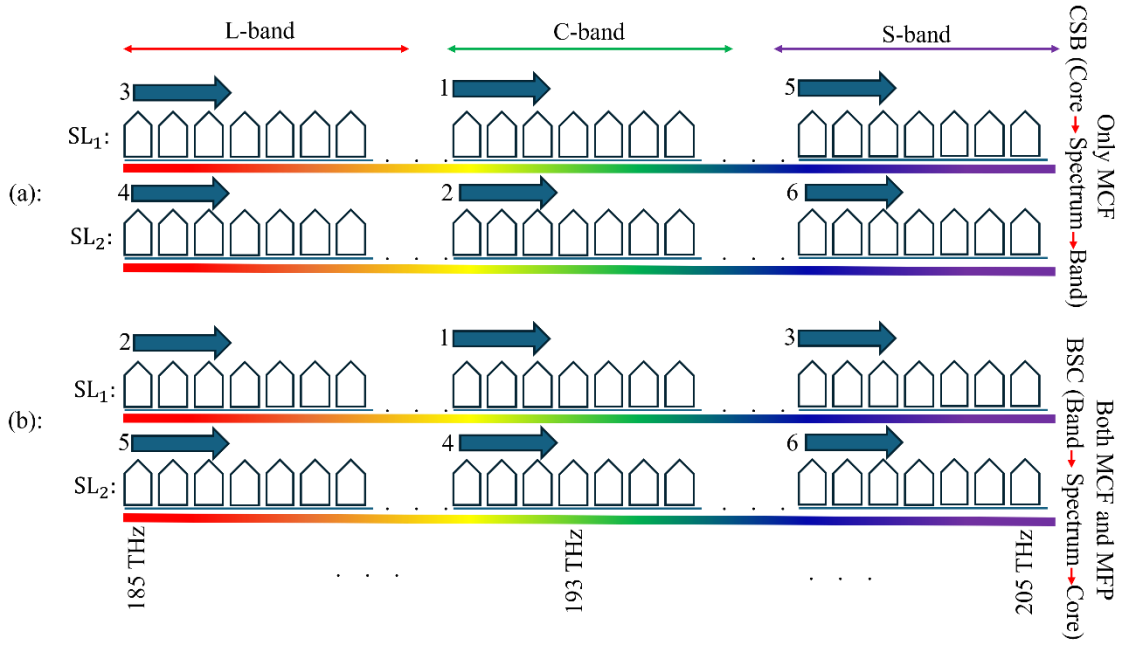

Figure 4.2-1 Different service provisioning in MBoSDM: (a) Core-Spectrum-Band (CSB), (b) Band -Spectrum- Core.

The L-band is prioritized next because the technology for L-band transmission is more mature, and the C-band amplifiers can also operate in the L-band with similar bandwidth. Additionally, the loss coefficient and dispersion in the L-band are relatively close to those in the C-band. However, the noise figure of amplifiers in the L-band is slightly higher compared to the C-band. As in the C-band, the service provisioning priority within the L-band follows the sequence of cores, starting from core 1 to the last core. Finally, the S-band is utilized. Channels in the S-band are provisioned sequentially, starting from core 1 and proceeding to the last core.

It should be noted that the component costs in each band are different, which creates a trade-off between band selection and the achieved capacity for each service provisioning approach. This trade-off arises because the Quality of Transmission (QoT) varies across bands due to the ISRS effect. For this reason, as a preliminary study, we evaluate different service provisioning approaches based on the priority of band, spectrum, and cores. The results are analyzed in terms of blocking probability, average GSNR, and the maximum reach distance for each modulation format.

To evaluate the performance of the proposed resource allocation methods, we developed the ICXT- and NLI-Aware Sliceable Routing, Modulation, Core, Band, and Spectrum Allocation (XT-NLI-A-RSA) algorithm (Algorithm 1) (see Figure 4.2-2). This algorithm uses pre-calculated physical layer parameters (including GSNR, supported modulation formats, and bandwidth) to ensure Quality of Transmission (QoT) requirements are met. XT-NLI-A-RSA operates in two stages:

Algorithm 1 ICXT- and NLI-Aware Sliceable Routing, Modulation, Core, Band and Spectrum Allocation (XT-NLI-A-RSA)

Inputs: (1) $KSPs$: Set of K-shortest paths, (2) bw_r: Bandwidth of request r, (3) MF^i_{path}: Pre-calculated modulation for channel i on $path$, (4) SAM: Spectrum Allocation Method.

Parameters: (1) bw_{rem}: Remaining bandwidth during slicing, (2) bw^i_{path}: Supported bandwidth for channel i on $path$.

Output: Path and Allocated Resources

1: $Allocated \leftarrow$ **False**
2: **for** ($path$ in $KSPs$) **do**
3: Find the first available channel in ASV using the first-fit approach and SAM, and assign its index to i
4: **if** i is valid **and** MF^i_{path} meets bw_r **then**
5: Allocate $path$, core, band, and channel to request r
6: $Allocated \leftarrow$ **True**
7: **return** Allocated resources for request r
8: **end if**
9: **end for**
10: **if** $Allocated$ is **False then**
11: **for** ($path$ in $KSPs$) **do**
12: $bw_{\text{rem}} = bw_i$
13: **while** $bw_{\text{rem}} > 0$ **do**
14: Find the first available channel in ASV using SAM, and assign its index to i
15: **if** i is valid **then**
16: Calculate bw^i_{path} based on MF^i_{path}
17: Allocate $path$, core, band, and channel to request r
18: $bw_{\text{rem}} \leftarrow bw_{\text{rem}} - bw^i_{path}$
19: **if** $bw_{rem} < 0$ **then**
20: **return** Allocated resources for all segments of request r
21: **end if**
22: **else**
23: Release all allocated resources to request r
24: **break**
25: **end if**
26: **end while**
27: **end for**
28: **end if**
29: **if** $Allocated$ is **False then**
30: Request r is blocked.
31: **end if**

Figure 4.2-2 ICXT- and NLI-Aware Sliceable Routing, Modulation, Core, Band, and Spectrum Allocation.

Stage 1: Single-Chunk Allocation

The algorithm first attempts to satisfy the request using a single, contiguous allocation along one of the K-shortest paths (KSPs, Lines 2-9). For each path:

1. An Available Spectrum Vector (ASV) is calculated using the specified Spectrum Allocation Method (SAM), which prioritizes either cores or bands. The ASV contains free channels that meet the continuity constraint and can support at least the basic Binary Phase-Shift Keying (BPSK) modulation format (based on pre-calculated data, Line 3).

2. A First-Fit approach selects the first available channel in the ASV that meets the QoT requirements (sufficient GSNR and supported modulation format for the requested bandwidth).

3. If a suitable channel is found, the necessary resources (path, core, band, and channel) are allocated, and the algorithm terminates successfully (Lines 4-7).

Stage 2: Sliced Allocation

If Stage 1 fails (the request cannot be allocated as a single chunk), the algorithm proceeds to Stage 2 (Lines 10-28). Here, the requested bandwidth is divided into smaller segments, and allocation is attempted sequentially along a single path using the First-Fit approach and the ASV. This process continues until either:

1. The entire request is successfully allocated.
2. The available resources are exhausted.

If allocation fails in Stage 2 across all paths, the request is considered blocked.

In Stage 2, the ASV is recalculated for each segment to ensure that the selected channel supports at least the minimum required modulation format. Resources are allocated iteratively for each segment until one of the following occurs:

1. The entire request is successfully allocated (Lines 14–21).
2. The available resources are exhausted.

If allocation fails at any point during the iterative process for a given path, all previously assigned resources on that path are released (Lines 22–26), and the algorithm attempts allocation on the next path in the path set. If the request cannot be fulfilled using either a single-chunk allocation (Stage 1) or sliced allocation (Stage 2) across all paths, the request is blocked (Lines 29–31). This version is more concise and improves the flow by using a more direct structure. The conditions for termination of the iterative process and the handling of allocation failures are more clearly defined.

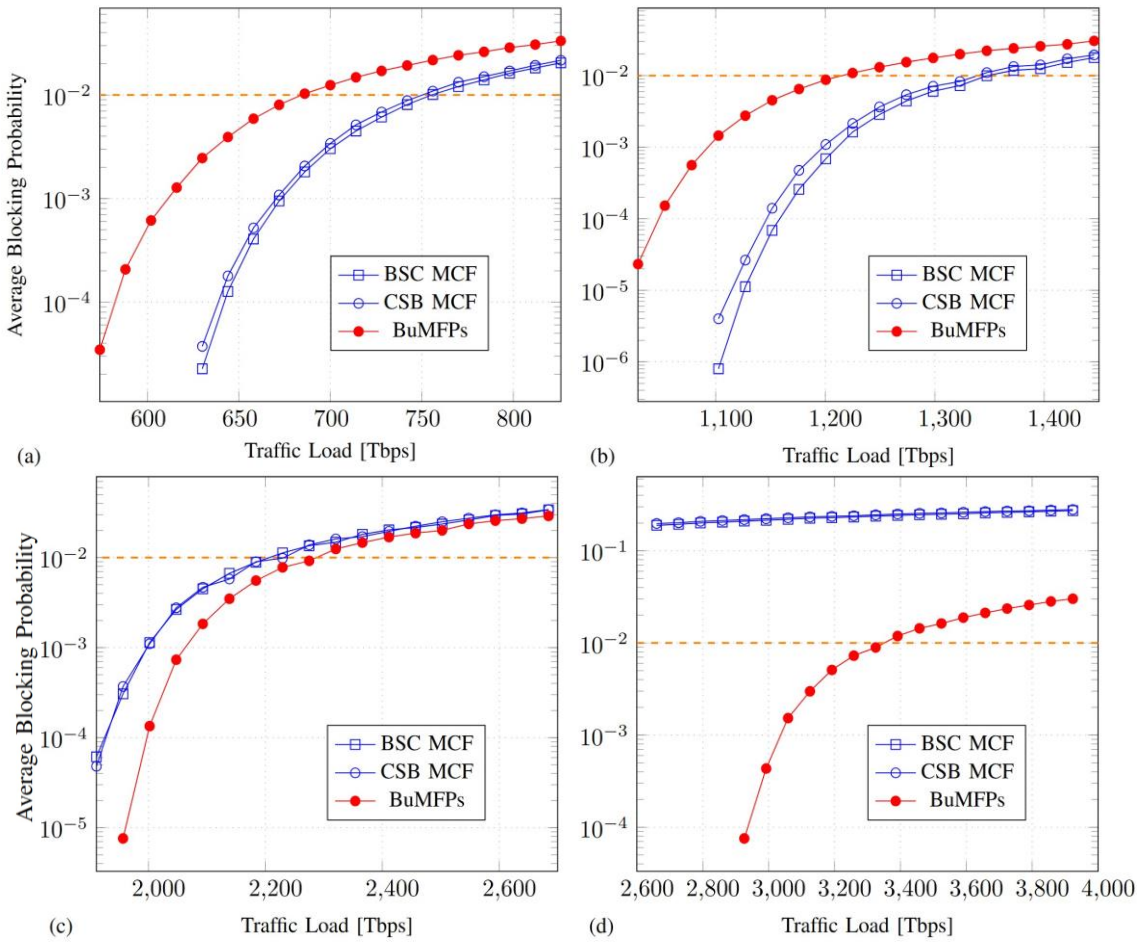

Figure 4.2-3 Average request blocking probability for the US Backbone topology using MCF with BSC and CSB approaches, and BuMFPs, for (a) 4, (b) 7, (c) 13, and (d) 19 cores/fibers.

Simulation results were obtained using the US Backbone topology (see Figure 4.1-7). The simulations considered C, L, and S bands across various configurations of bundled multi-fiber pairs (BuMFPs) and multi-core fibers (MCFs). BuMFP configurations included 4, 7, 13, and 19 single-core fibers, while MCF configurations used fibers with the same number of cores. All configurations featured 80, 80, and 108 fixed-grid channels in the C, L, and S bands respectively, each with 75 GHz bandwidth. Inter-arrival and holding times for requests followed an exponential distribution, with requested bandwidths uniformly distributed between 100 and 600 Gbps (in 100 Gbps increments). Line card interfaces (LCIs) supported data rates from 100 to 600 Gbps, corresponding to modulation formats ranging from BPSK to 64-QAM. Average blocking probabilities were calculated using either a 95% confidence interval or a maximum of 50 independent iterations (with 15,000, 25,000, 50,000, and 75,000 requests per iteration for 4, 7, 13, and 19 cores/fibers, respectively).

Figure 4.2-3 shows the blocking probability versus traffic load (in Tbps) for BuMFPs and MCFs, by using Core Priority (CSB) and Band Priority (BSC) spectrum allocation methods. BuMFPs exhibited significantly higher blocking probabilities than both BSC and CSB MCF configurations across all traffic loads. MCF configurations consistently reduced blocking probability by over 67%

compared to BuMFPs. This is attributed to the lower loss coefficients and ICXT in MCFs, enabling higher GSNR and the use of higher-order modulation formats, thus resulting in more feasible lightpaths. The analysis for 4-core MCFs showed that modulation formats and GSNR varied significantly across the bands due to differences in loss and ICXT. The C-band consistently outperformed the L- and S-bands. The L-band generally outperformed the S-band due to lower ICXT. The BSC approach, by prioritizing band allocation, reduced blocking probability by approximately 40% at 630 Tbps and by about 10% on average compared to the CSB approach.

5 POWER-EFFICIENT AND COST-EFFECTIVE ACCESS AND FRONT/MID-HAUL TRANSPORT SOLUTIONS

5.1 DYNAMIC SPATIAL AGGREGATION FOR ENERGY-EFFICIENT PASSIVE OPTICAL NETWORKS

The spatial PON architecture proposed in SEASON, summarized in Figure 5.1-1(a), leverages dynamic spatial aggregation to enhance the energy efficiency of Passive Optical Networks (PONs). The system dynamically activates and deactivates optical line terminal (OLT) ports and spatial lanes (e.g., cores in multi-core fibers or separate fibers) based on traffic conditions. By redirecting low-load traffic to fewer active OLT ports during off-peak hours, the architecture minimizes power consumption without compromising network performance (Figure 5.1-1 (b)). During peak load periods, all OLT ports are activated to maintain throughput (Figure 5.1-1 (c)), demonstrating the flexibility and scalability of the design.

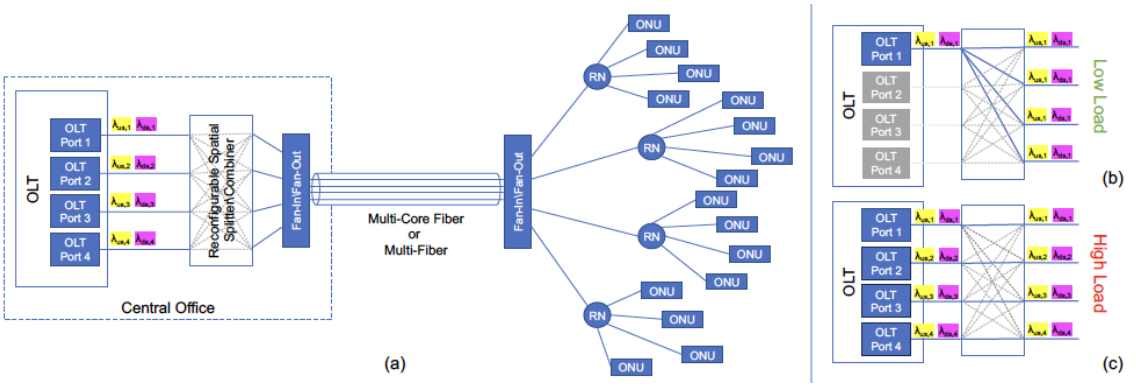

Figure 5.1-1 SEASON Spatial PON Architecture.

The considered performance evaluation parameter is energy saving. We define the energy saving S, obtained through the proposed approach, as Eq. 36, where E_{BL} is the baseline energy consumption, i.e., the energy consumption obtained when all the spatial lanes are always *active*, and E_S is the energy consumption obtained with our proposed spatial aggregation technique.

$$\mathrm{S} = \frac{\mathrm{E_{BL}} - \mathrm{E_S}}{\mathrm{E_{BL}}} \qquad \text{Eq. 36}$$

We assume decisions on spatial aggregation/disaggregation being applied with a fixed periodicity T. During a period defined by the periodicity T, the energy consumption of an OLT is given by Eq. 37, where $\mathrm{P_{OLT}}$ is the power consumed by the OLT. It is worth noticing that this implies that power savings are equivalent to energy savings.

$$\mathrm{E_{OLT}} = \mathrm{P_{OLT}} \times \mathrm{T} \qquad \text{Eq. 37}$$

We model the power consumed by the OLT as the sum of a fixed component P_F which accounts for all the elements which are not dependent on the number of active spatial lanes such as shelter circuitry, ethernet interfaces, and fans and a variable component P_V which is associated with the activation and deactivation of spatial lanes and accounts for transceiver power consumption, and PON interface circuitry.

Thus, the power consumed by the OLT through the baseline approach P_{BL} can be modelled as Eq. 38, where C is the number of spatial lanes in the considered spatial PON system.

$$\mathrm{P_{BL}} = \mathrm{P_F} + \mathrm{C} \times \mathrm{P_V} \qquad \text{Eq. 38}$$

Instead, the power consumed through the spatial approach P_S varies basing on the spatial aggregation decision taken in the interval t. Thus, we define $P_{S,t}$ as Eq. 39, where A_T is the number of active spatial lanes for the interval t of length T with $A_t \leq C$.

$$\mathrm{P_{S,t}} = \mathrm{P_F} + \mathrm{A_t} \times \mathrm{P_V} \qquad \text{Eq. 39}$$

Thus, the energy saving S in the interval t can be defined as S_t and calculated as Eq. 40.

$$\mathrm{S_t} = \frac{\mathrm{E_{BL}} - \mathrm{E_{S,t}}}{\mathrm{E_{BL}}} = \frac{\mathrm{P_{BL}} - \mathrm{P_{S,t}}}{\mathrm{P_{BL}}} = \frac{C - A_t}{\frac{P_F}{P_V} + C} \qquad \text{Eq. 40}$$

The energy efficiency gains are illustrated in Figure 5.1-2 and Figure 5.1-3. Figure 5.1-2 shows the percentage of spatial lanes that can be deactivated across varying traffic conditions for Small Office/Home Office (SOHO), Large Business, and Mobile traffic patterns. The results indicate that higher numbers of spatial lanes correspond to increased potential for deactivation, with SOHO traffic achieving the most significant deactivation rates (up to 40%).

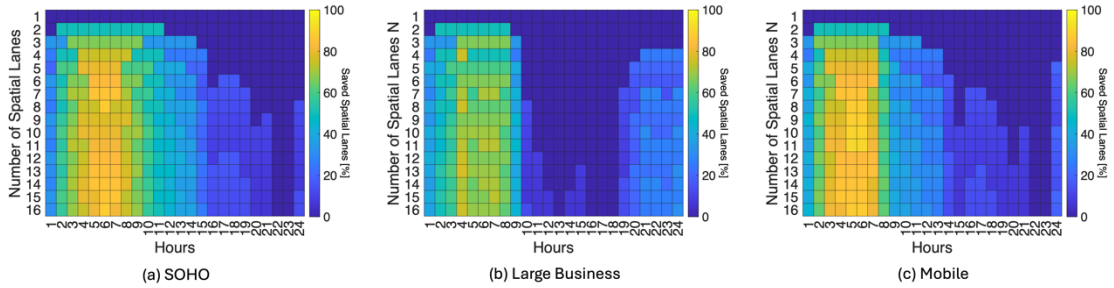

Figure 5.1-2 Savable Spatial Lanes for different traffic patterns and Spatial PON sizes.

Figure 5.1-3 presents the average energy savings achieved compared to a traditional PON architecture, which lacks spatial aggregation capabilities. Savings depend on the ratio of fixed power consumption (P_F) to variable power consumption (P_V). For configurations with 4, 8, and 16 spatial lanes, the savings range from 2-7% when P_F /P_V =100 to 18-38% when P_F /P_V =1, demonstrating substantial reductions in operational energy consumption. The architecture's

scalability and adaptability make it a viable solution for next-generation, energy-efficient optical networks.

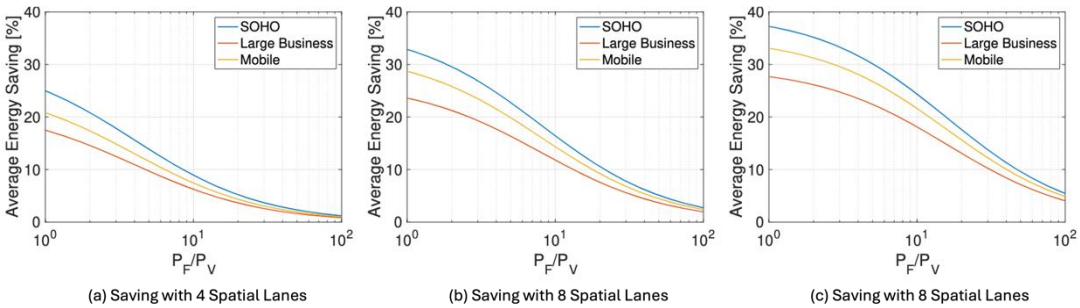

Figure 5.1-3 Achievable energy Savings.

This analysis highlights the potential for further optimization, particularly through real-time traffic monitoring and advanced algorithms for ONU handovers. Future work will focus on integrating these enhancements and evaluating their impact on latency and energy savings in experimental deployments.

5.2 POWER CONSUMPTION OF DSCM TRANSCEIVERS IN THE METRO-AGGREGATION DOMAIN

To investigate power consumption in metro-aggregation networks and generalize our findings with respect to the power consumption of transceivers with DSCM, we have implemented a numerical tool that generates random topologies based on network examples that were previously provided by Telecom Italia [Cas24, Cas24-2]. To simplify the analysis, spur-arc extensions, rings, or nodes without protection paths have been neglected. Figure 5.2-1 illustrates the general network topology used in this study, where s, N, and d denote the number of sublinks in the network, the number of leaf nodes in said sublink, and the distance between nodes, respectively.

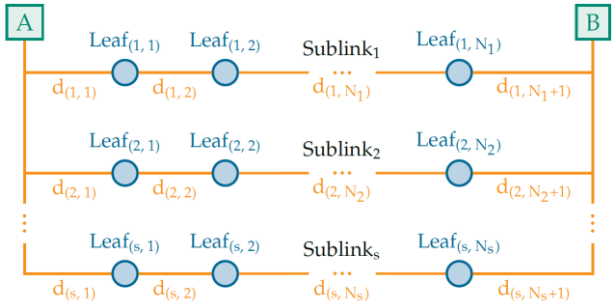

Figure 5.2-1 General topology for metro-aggregation networks.

The concept behind our study is to generalize the results in [Cas24-2], since despite their similarities, these network examples exhibit multiple aspects that make them different enough from a design perspective. Therefore, to draw more comprehensive solutions on the use of DSCM technologies in the metro-aggregation domain, it is necessary to investigate as many scenarios as possible. For this reason, we dissected the available examples given to us by Telecom Italia and drew some probability distributions regarding their main design characteristics. This information is summarized in Figure 5.2-2.

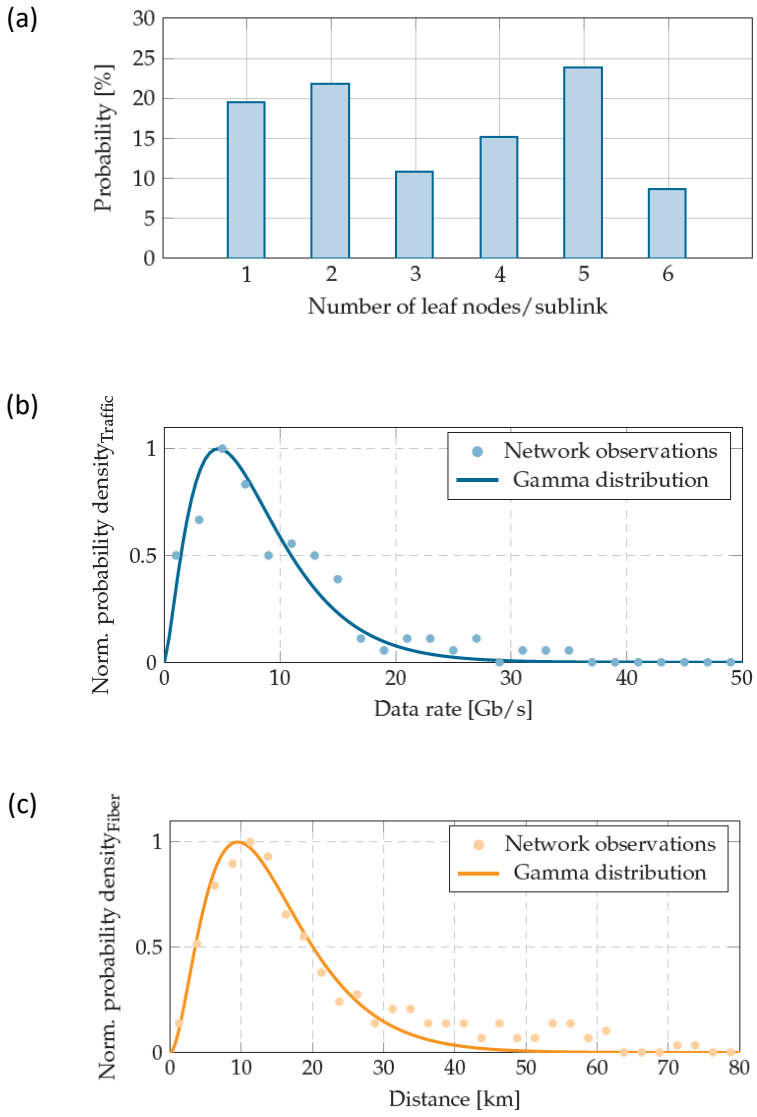

Figure 5.2-2 (a) Probability of generating sublinks with a particular number of leaf nodes. (b) Normalized probability density corresponding to the leaf node' traffic demands. (c) Normalized probability density corresponding to the fiber segments' distances.

Our investigation's primary focus is to draw a link between operating conditions in a network (e.g. OSNR performance and hardware activation) and the corresponding consumption as traffic demands increase over time. In this regard, we are assuming that traffic in the network exhibits

a year-over-year compound average growth rate (CAGR) between 10% and 40%. This behavior extends over a duration of 10 years.

To evaluate the hardware configuration in the network scenarios, we consider 100 Gb/s (4 x 25 Gb/s) and 400 Gb/s (16 x 25 Gb/s) DSCM pluggable transceivers, where the number of active subcarriers can be flexibly adjusted depending on the traffic situation (i.e., a granularity of 25 Gb/s). Regarding the placement of the pluggable units, there are certain constraints: for a network operating in point-to-point fashion, only 100 Gb/s modules will be used; while for point-to-multipoint, it will be possible to use 400 Gb/s units exclusively at the hub side. In consideration of the increasing traffic demands over time, we have adopted a 'Pay-As-You-Grow' model, where traffic will be inspected on a yearly basis and additional transceivers will be deployed based on whether the existing hardware is still able to cope with the demands.

By determining not only the growth of the network, but also how much hardware is required and the operating conditions of the transceivers (i.e., availability of bandwidth resources), we can investigate how the performance changes as traffic increases, its impact on reach, the effectiveness of optical aggregation in filterless point-to-multipoint networks, the usage of the transceivers across the network, and the extent to which DSCM can contribute to lower the power consumption from a transceiver-centric point of view.

5.3 COMPARISON BETWEEN TRANSCEIVERS WDM P2P AND P2MP TRANSCEIVERS WITHIN A FULL MESH FOR FH NETWORK

This section details the ongoing techno-economic analysis concerning experiments on metro-aggregation and single fiber bidirectional operations. This study is a part of our larger initiative to enhance network infrastructure by reducing costs while ensuring high performance and service quality.

The main goal of this techno-economic investigation is to evaluate the cost-effectiveness and performance advantages of deploying Point-to-Multipoint (P2MP) transceivers in the fronthaul segment. By decreasing the number of required transceivers, we aim to realize significant savings in both equipment and operational expenditures.

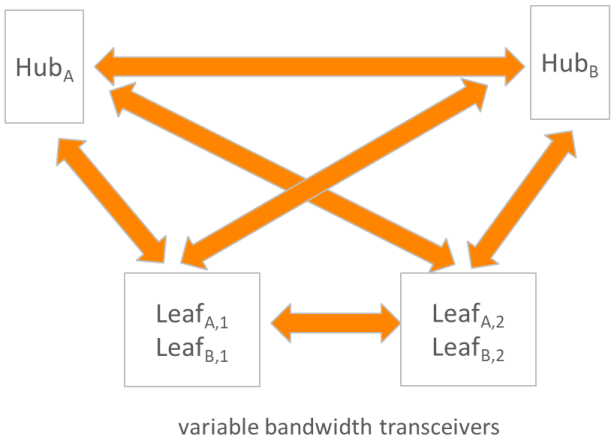

Figure 5.3-1 Simplification of Figure 5.1-1 enabled by P2MP transceivers.

Preliminary analyses indicate that incorporating P2MP transceivers can significantly reduce costs associated with transceivers since fewer units are needed to achieve the same coverage. Additionally, the simplified network architecture may lead to decreased maintenance and operational costs. Nevertheless, these advantages must be balanced against potential challenges, such as the need for precise network planning and the possible effects on signal quality.

These aspects will be examined in particular:

- Cost Analysis: analyzing the capital expenditure (CAPEX) and operational expenditure (OPEX) associated with traditional versus P2MP transceiver setups. This includes costs related to hardware, installation, maintenance, and energy consumption.
- Performance Evaluation: the study will measure the impact of P2MP transceivers on network performance metrics such as latency, bandwidth utilization, and reliability. This will be compared against existing configurations to quantify improvements.
- Scalability Assessment: evaluating the scalability of the proposed setup, particularly its ability to handle increased traffic loads and its adaptability to future technological advancements.

6 SMART EDGE NODES FOR PACKET/OPTICAL INTEGRATION WITH COMPUTING RESOURCES

6.1 RAILWAY-MOTORWAY MOBILE SERVICE COVERAGE SCENARIO DEFINITION FOR PDU APPLICATION USE CASE

The scenario we intend to analyze concerns the coverage of a railway line or a motorway section where the high-bandwidth, low-latency and high-reliability mobile radio connectivity service must be provided. Due to the inherent topography features of this service, it must be provided within a very narrow but continuous surface along the railway or motorway line. In terms of scenarios defined in the SEASON context, this means considering an additional geotype that is added to the four already identified in D2.1 (i.e., rural, suburban, urban and dense urban, the ones considered in the study reported in subsection 3.4) [SeaD2.1].

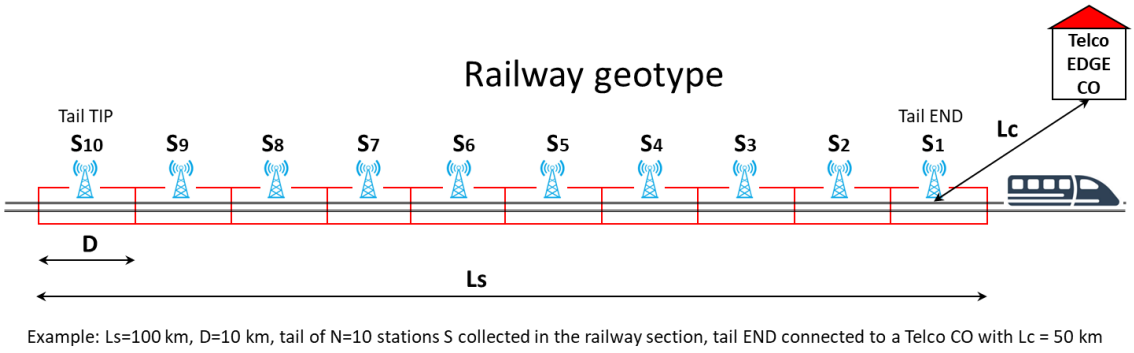

Figure 6.1-1 Logical and geometric model for the Railway coverage geotype.

Figure 6.1-1 shows this additional geotype model in terms of logical and geometrical representation. In the following we will refer to the railway, but similar considerations can be made for a motorway. A section of railway line is covered by several radio stations S equipped with 2 RU and a vDU in the middle of segments of length D along the line. A section of railway line of length L_s will have N stations of type S (S_1, S_2,..., S_N) with $N = L/D$. The radio signal propagates mainly to the left and right of the S station along the tracks with some overlap at the junction points with that of the adjacent segment. This is achieved by aligning the propagation lobes of the two RUs of each radio station to the railway tracks in opposite directions to each other. The set of mobile stations $\{S_1, S_2,..., S_N\}$can be viewed as a tail with the end of the tail END. S_1 is the mobile station connected to a Telco EDGE Central Office (L_c km away), while the TIP of the tail (S_N) is the last mobile station of the tail in the opposite direction. The tail is completed by other $N - 2$ mobile stations connected in a chain between the TIP and the END. Fiber optics is considered available for interconnection needs along the railway line and between the end-of-line mobile radio station (tail END in Figure 6.1-1) and the EDGE central office.

Telco EDGE Central Office allows traffic collected along the railway line to be processed and provides the requested services which can be supplied locally if it is possible, remotely otherwise. This kind of model that assure the radio coverage of the line can be implemented in different options in terms of RAN architecture and transport solutions.

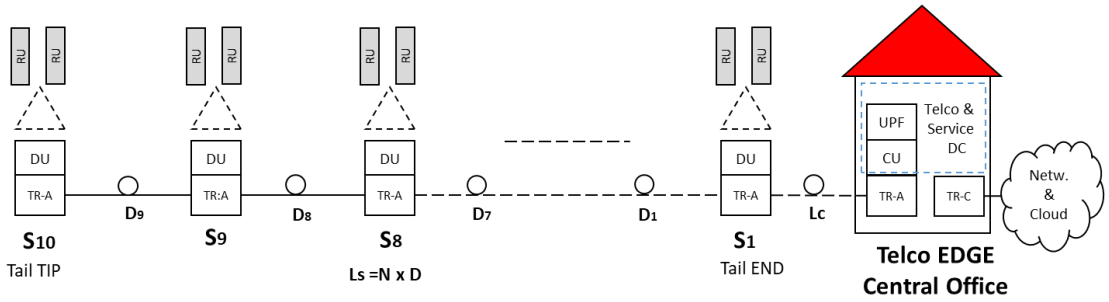

Figure 6.1-2 Cloud RAN architecture with distributed DU applied to Railway geotype.

A further step in the use case assumption is made in Figure 6.1-2 where the RAN architecture is illustrated. In Figure 6.1-2, the double split option 2 & 7.2 [ORA21] is assumed and DU function is placed at the radio station together with the 2 RUs serving the associated line segment D km long. Mid haul (MH) traffic is collected through a transport system (Transport aggregation, TR-A) interconnecting the radio stations with a chain topology from tail TIP to tail END (each fiber segment is D km length) and then from tail END to the Telco EDGE Central Office (DC) (fiber distance is L_c km), where other mobile functions (RAN CU and mobile core UPF) as well as other telco and service functions are installed in the CO DC. The Telco EDGE CO has a separate transport equipment for the interconnection with other COs (Cloud or Edge level) through the core transport network (TR-C). The analysis will concentrate on networking between radio base stations and Telco Edge central office.

6.1.1 Data rate requirement from radio units

Among many combinations of radio system parameters, two scenarios will be considered to assign data rate requirement in different sections of functional splits of the RAN. They are classified as 5G medium-term and 6G long-term scenarios, even though enabling technologies and availability of radio bands and frequency slots for carriers to implement both scenarios would be still available in the short term. The high-level radio requirement for the radio base stations used in the use case and for the two scenarios are the following ones:

Scenario 5GA in medium-term.
2xRU at 3.7 GHz with carrier width 200 MHz, 8 MIMO layers, less than 10 Gb/s of MH traffic at peak for the two RU. Max length for line segment D is estimated of 10 km, the maximum reach of radio signal is 7.5 km. The meaning of reach here is the distance at which the radio signal has enough power and signal to noise ratio to be to be used effectively by a radio mobile terminal.

Scenario 6G in long-term.
2xRU at 26 GHz with carrier width 1000 MHz, 8 MIMO layers, less than 50 Gb/s of MH traffic at peak for the two RU. Max length for line segment D is estimated of 2 km. The maximum reach of radio signal is 1.5 km.

It should be noted that the study focuses on transport solutions for RAN regarding fiber network, therefore the radio characteristics are not explored and specified in depth, and it is assumed that the solution is enabled under the radio aspect. In a real implementation the parameters (distances, reach of the base stations, radio parameters and resulting data rate of the FH flows) mentioned above could be subject to even significant variations.

6.1.2 Comparison of different RAN architectures

For the railway geotype the C-RAN architecture with distributed DU shown in Figure 6.1-2 is not the only possible one, the reference scenario with which to make comparisons is a baseline scenario that uses a traditional non-cloud based architecture.

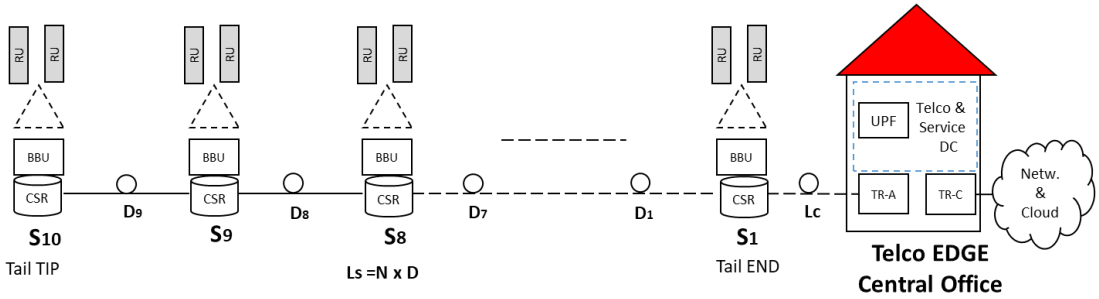

Figure 6.1-3 Baseline traditional architecture for scenarios comparison.

A possible baseline scenario is depicted in Figure 6.1-3. It involves the use of BBU aggregated equipment (like the ones used in legacy traditional mobile networks) that integrate DU and CU functions and an aggregator router (Cell Site Router, CSR) that collects the traffic from BBU. In this scenario the traffic sent from BBU to CO through aggregator routers is backhaul (BH), slightly lower than mid haul traffic of Cloud RAN with distributed DU case of Figure 6.1-2 . The transport solution can be a dark fiber connection from router to router obtained with gray pluggable transceivers inserted directly into the routers. With this solution, the router at the head (the one in position 1) must process and retransmit the BH traffic of all the base stations of the entire segment of railway line (in the example there are 10 stations) and therefore must be sized to have sufficient capacity. The links between routers must also have increasingly greater capacity going from the tip of the queue (position 10) to its end (position 1). If 10 Gb/s is sufficient between S_{10} and S_9, 90 Gb/s becomes necessary between S_2 and S_1 and 100 Gb/s between S_1 and the CO. In the traditional architecture other transport solutions could be used to carry the backhaul traffic from the BBUs to the central office. For example with transceivers directly plugged on the BBUs (but it would require a couple of fiber for each BBU and in the sections near the end of the chain and from the end of the chain to the CO many pairs would be

necessary) or, to save fiber, with P2MP optical networking done with DSCM transceivers with star connectivity from the radio base stations to the central office. In this case a line system with splitters at the intermediate points would be necessary.

6.1.3 Use of DPU and P2MP transceivers in Cloud RAN

Smart network interface cards (smart NICs) and Data Processing units (DPUs) providing hardware-accelerated networking and computing functionalities enabling new applications and use cases in Telco cloud scenarios. One of the aspects that we intend to evaluate is the use of DPU cards in equipment hosting RAN functionalities (e.g., vDU or VCU): referring to the innovative architectural scheme illustrated in Figure 6.1-2, the system that hosts the vDU and the TR transport device could be created in an integrated way with a server equipped with a DPU card. This card ensures, through pluggable transceivers directly inserted in it, also the transport functions. In this way, specialized transport devices would be avoided, achieving a simplification, and obtaining economic and energy savings. This type of card was considered in the work [Bar21] from which Figure 6.1-4 is taken. In the figure it is possible to see how the DPU cards, equipped with an autonomous processing capacity (Figure 6.1-4(b)), can perform functions that in traditional architectures must be performed by the internal HW of the server (by the motherboard, as in Figure 6.1-4(a)). P4 programming language (P4 logo is highlighted in Figure 6.1-4 next to the routers and cards) can be used for enabling an efficient way to handle packets forwarding in the IP layer. In the solution we intend to analyze for the railway coverage scenario, the DPU cards, which should host the pluggable transceivers with data rates adequate for FH traffic, would integrate with the pluggable the transport function avoiding dedicated equipment like switches or separated optical devices.

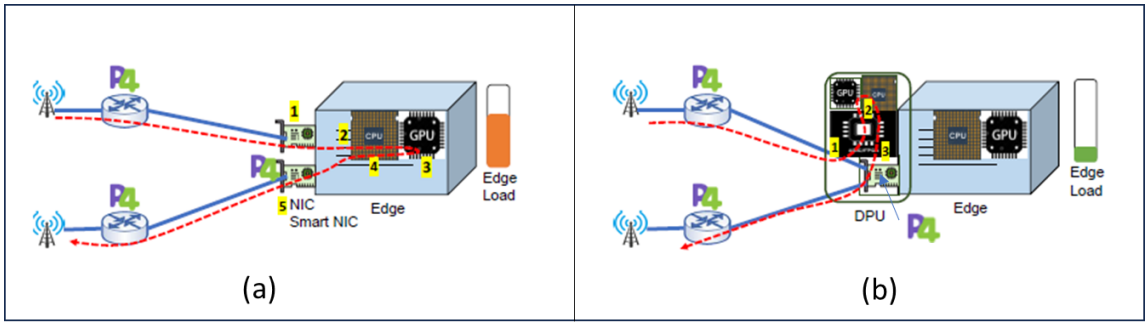

Figure 6.1-4 Edge box (typically a server) equipped with smart Network Interface Card (NIC) (a) and with the more powerful Digital Programmable Unit (DPU) (b) [Bar21].

An example of a possible transport networking for RAN X-haul that is suitable for the railway scenario of Figure 6.1-2 is exemplified in the Figure 6.1-5 and in Figure 6.1-6. This solution for transport networking is described extensively in D5.1 [SeaD5.1] where in addition to the transport solution an innovative 5G Automation Platform to dynamically activate DUs according to cell traffic conditions is proposed and experimentally validated. The considered O-RAN

transport networking solution is deployed on a bidirectional optical horseshoe network, and we propose two alternative architectures for the O-RAN implementation.

In a first architectural option the vDU runs in a Telco Edge Central Office including computing resources and IPoWDM equipment (as it is represented in Figure 6.1-2 on right). Radio Unit boxes are present on base stations along the railway (S_1, S_2, …). Front Haul high data rate flows must be carried from base stations to the Telco Edge CO. Communication from a central hub (i.e., Telco Edge CO) to multiple leaf locations (i.e., S_1, S_2,…) can leverage on P2MP digital subcarrier multiplexing (DSCM). In particular, the ports at hub location are split into lower rate sub-ports (e.g., a single 400G port can be divided into 4x100G ports), with each sub-port independently routable to different endpoints. In the Telco Edge CO, the function performed by the switch can be replaced by a DPU. This solution can be applied if capacity required by FH flows are compatible with data rates of P2MP DSCM transceivers, but this should be assured in realistic scenarios including the scenario 6G for the long-term as base stations are equipped with only one radio layer and two radio cells and radio parameters are not extremely challenging (in 6G for the long-term FH aggregated flow per base station (two cells) is calculated to be less than 50 Gb/s). Please note that the optical interworking in the horseshoe is based on a filterless architecture and in requires only passive splitter and combiners (sp1, sp2, …) at the branch points avoiding the use of WDM equipment like OADM.

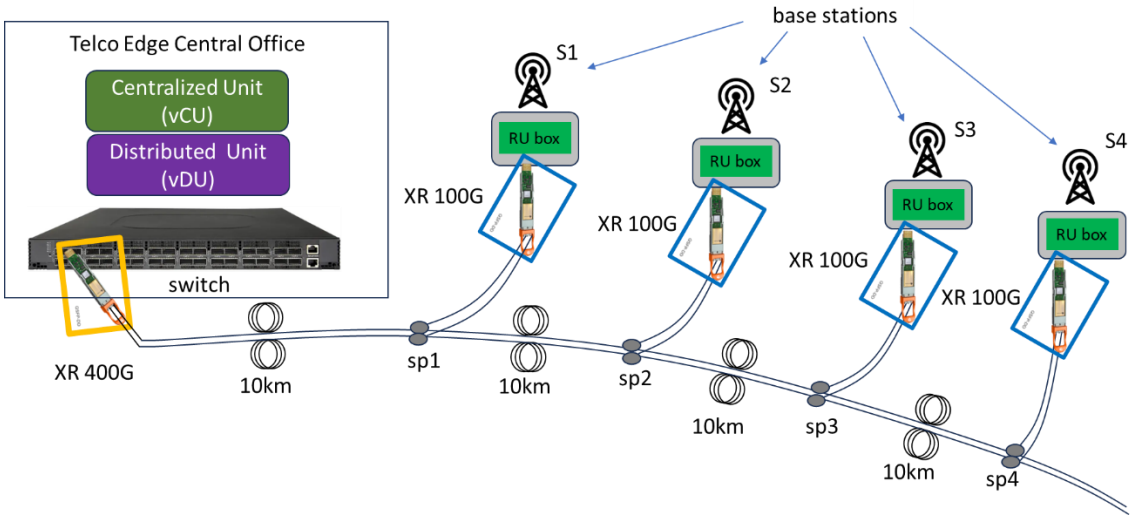

Figure 6.1-5 O-RAN architecture applied in Raylway coverage use case with vDU function placed at Telco Edge CO and Front Haul flows carried by DSCM P2MP internetworking from base station to Telco Edge CO.

An alternative architecture (considered in D5.1) that moving the vDU to the radio base station is illustrated in Figure 6.1-6. Radio base stations become Far Edge Nodes for the Telco Cloud infrastructure as they are host the vDU functionality on a dedicated HW box (typically a specialized server). In this case the O-RAN control functions are also highlighted (orange boxes) and they allow to dynamically manage the activation/deactivation of the vDU on the base of traffic load. In this case the traffic flows to be transported from the radio base stations to the Telcom Cloud are of the mid-Haul (MH) type and therefore much lower than in the FH case considered in the first alternative with vDU at Telco Edge CO. for the long term 6G case the mid-haul flows generated by a radio base station would be less than 10 Gb/s requiring only one 25

Gb/s subcarrier to be transported. The P2MP DSCM networking based on filterless nodes on horseshoe topology is the same type as the one presented in the scenario of Figure 6.1-5.

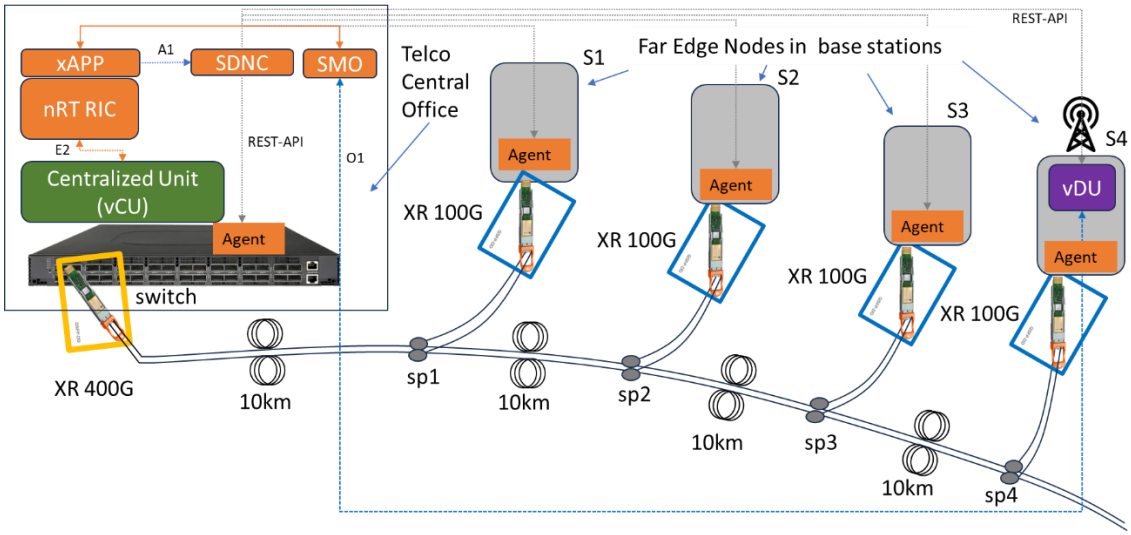

Figure 6.1-6 O-RAN architecture applied in Railway coverage use case with vDU function placed at base stations that became Far Edge nodes, and Mid Haul flows carried by DSCM P2MP internetworking from base station (Far Edge nodes) to Telco Edge CO.

6.1.4 Cost and power model and techno economic evaluations

The cost model for the railway 6G coverage use case presented in this subsection will have to consider the characterizing elements that constitute the solution. In particular, the comparison will focus on a legacy-type baseline solution based on aggregated and closed RAN functionalities (baseband unit (BBU) at the site and centralized core network) and a solution based on the O-RAN architecture that uses DPU cards on the servers and P2MP networking for transport with pluggable elements hosted on switches or PDUs. Only the components relevant for the transport of X-Haul flows will be evaluated. The work of defining the cost model is in progress in WP2 and will be presented in the next deliverable D2.3 together with the results of the technical-economic evaluation of the railway 6G coverage use case.

7 CONTROL PLANE, MONITORING AND STREAMING TELEMETRY

7.1 INTELLIGENT DATA AGGREGATION FOR TELEMETRY DATA REDUCTION

In this section, telemetry data compression results that are achieved by the different intelligent data aggregation techniques developed within SEASON project are summarized. These results aim at highlighting the achievement of KPI 7.1. The details of the different algorithms, as well as other performance evaluation results are presented in [Vel23], as well as in WP4 deliverables.

7.1.1 Summary of methods

In this project, three techniques are proposed for reducing the dimensionality of telemetry measurements that need to be collected and conveyed to a centralized system, thus dealing with telemetry volume and velocity. The techniques are specifically designed for the measurements of larger size, i.e., optical spectrum and IQ constellations. These techniques are:

- **Supervised Feature Extraction**: this simple but effective dimensionality reduction technique is intended to generate a set of features $\varphi(M)$ that characterize a measurement sample M. Examples of feature set φ are:
    - **For Optical Spectrum Signals:** ordered list S of frequency–power pairs; specifically, power is characterized by the mean and the standard deviation of the power around the central frequency, as well as a set of primary features computed as cutoff points of the signal with different power levels including -3dB and -6 dB.
    - **For IQ Constellations:** parameters of the empirical bivariate Gaussian distribution (mean and covariance matrix) obtained after applying Gaussian Mixture Models [Bou20] to the optical constellation sample.
- **Data Compression:** this technique allows compressing optical constellation samples by using auto-encoders (AE), a type of neural network with two components: the encoder, which maps input data into a lower-dimensional latent space, and the decoder, which gets data from the latent space and reconstructs the original data back [Rui22-2].
- **Data Summarization:** even when telemetry sample size is greatly reduced by both feature extraction and compression techniques, assuming a high collection frequency entails a large volume of data being conveyed. However, this is not needed in general in normal conditions. Hence, we could measure variations in the computed features to decide whether a new sample M or a representation of it needs to be processed. In case no significant variations with respect to the previous past values are found, averaged values of the features with a much lower frequency are sent to the centralized controller, thus reducing the volume of collected and conveyed telemetry data.

7.1.2 Results

Using openly available datasets [Rui22], [Rui24], we numerically evaluated the compression performance of the different methods mentioned above. Table 7.1-1 and Table 7.1-2 show the compression results of supervised feature extraction and auto-encoder based compression. For the former, each spectrum sample has been reduced to 13 cut-off points, while optical constellation samples of 16-QAM signals have been reduced to 80 features (5 coefficients of the bivariate Gaussian distribution that better characterize each of the constellation points). For the latter, an auto-encoder with a latent space of 32 hidden neurons has been trained with a number of training 16-QAM constellations and evaluated on a different validation set. The accuracy of the sample reconstruction of the decoder is larger than 95%, which leads to negligible loss of information. In view of both tables, one can observe that outstanding compression is achieved (>90% in all the cases). Note that increasing sample resolution, expands the size of original samples but not the size of compressed ones, highlighting the great scalability of the proposed methods.

Table 7.1-1 Compression Results (Supervised Feature Extraction).

Sample	**Original Size n_o (Bytes)**	**Compressed Size n_c (Bytes)**	**Compression Ratio (%) = $100 \times (n_o - n_c) / n_o$**
Spectrum (75GHz)	600	52	91.33%
Spectrum (4.8 THz)	38400	52	99.87%
IQ Constellation (2048 symbols)	16384	320	98.05%
IQ Constellation (10k symbols)	80000	320	99.60%

Table 7.1-2 Compression Results (Data Compression).

Sample	**Original Size n_o (Bytes)**	**Compressed Size n_c (Bytes)**	**Compression Ratio (%) = $100 \times (n_o - n_c) / n_o$**
IQ Constellation (2048 symbols)	16384	128	99.22%
IQ Constellation (10k symbols)	80000	128	99.84%

Finally, Figure 7.1-1 represents the total amount of data from measurements collected in one day, every 30 seconds (IQ constellations and spectrum) in a simulated network consisting in 50 nodes. By combining compression (both supervised feature extraction and auto-encoder based compression) and summarization, total telemetry data volume conveyed from distributed probes (coherent receivers and spectrum analyzers) to the centralized controller can be reduced in 3 orders of magnitude.

In conclusion, the results allow clearly achieving the target KPI 7.1: Intelligent data aggregation to provide data compression ratio >90% without significant information loss (Figure 7.1-1).

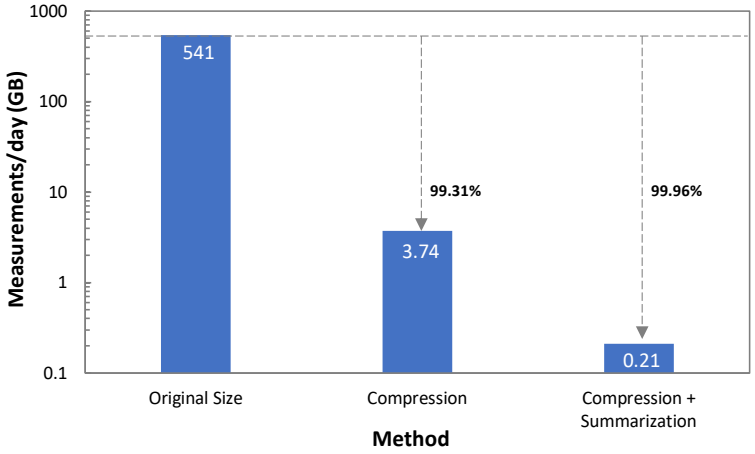

Figure 7.1-1 Provisional figure to illustrate how P2MP could be used to collect MH traffic.

Dissemination Level	SEN (Sensitive - limited under the conditions of the Grant Agreement)

8 Artificial Intelligence (AI)/Machine Learning (ML) Service Orchestration and Self-Management and Secure AI

8.1 Dynamic Subcarrier Allocation in P2MP Connections To Reduce Energy Consumption

Optical point-to-multipoint (P2MP) connectivity [Rui14] based on digital subcarrier multiplexing (DSCM) has been shown as a solution for the metro-access segment that is able to reduce capital and operational costs and support the capacity and high dynamicity needs of future 6G services [Wel21]. To achieve maximum performance, activation and deactivation of subcarriers must be done near-real-time to provide just the capacity needed to support the input traffic.

In addition, OPEX savings can be obtained by exploiting DSCM capability for operating the different SCs independently, so just enough capacity to support the input traffic is provided, which reduces energy consumption. However, that requires near-real-time operation, as well as some anticipation to give time to timely activate the SCs, so that they become available when it is required.

DSCM facilitates the deployment of P2MP optical connectivity, since SCs sourced from a single hub node can be assigned to different leaf nodes. In the reverse direction (denoted MP2P), SCs generated from different leaves can merge to connect the source nodes to the hub node. For illustrative purposes, Figure 8.1-1(a) presents an example where four-leaf nodes are connected to a hub node in a P2MP connection. In the example, the hub node can support 16 SCs and each leaf node is assigned 4 contiguous SCs, while ensuring that each SC is assigned to a single leaf node, so as to avoid SC overlap (also referred to as oversubscription) since it leads to data loss.

Comparing the P2MP optical connection in Figure 8.1-1(a) to a regular P2P one, we observe the reduction in the total number of transponders that are required, i.e., four Txs for the leaf nodes and one Rx for the hub node in the case of the P2MP connection in contrast to four Txs and four Rxs, respectively, in the case of optical P2P.

The above observation can also be stated in a slightly different way. In the example in Figure 8.1-1(a), 4 leaf nodes are serviced since DSCM Txs can generate up to 4 contiguous SCs and the DSCM Rx can process up to 16 SCs. The number of leaf nodes in a P2MP connection can be further increased with dynamic SC management, which can assign SCs dynamically to the leaf nodes, so those not requiring the full capacity of the transponder to support the local traffic can give one or more of their SCs up to other leaf nodes with higher capacity requirements. This can result in cost savings, as more leaf nodes [e.g., five leaves, as in Figure 8.1-1(b)] can be serviced, as well as in power savings, since not every SC might be required to be active for the current traffic. For these gains to be fully realized, a control mechanism is necessary to ensure the proper P2MP connection operation, specifically from leaves to the hub (MP2P), to avoid oversubscriptions and to assure that the capacity needs of every leaf node are met.

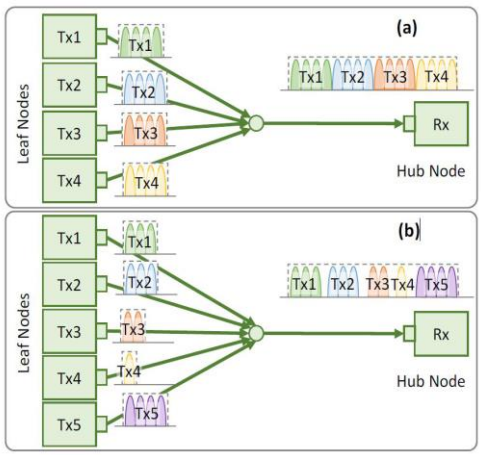

Figure 8.1-1 Example of a P2MP connection with four (a) and five(b) leaf nodes.

8.1.1 Summary of methods

Among different methods for the control of MP2P DSCM-based connections that have been developed so far in the context of SEASON project, we focus on the three alternatives depicted in Figure 8.1-2. These are:

- A classical centralized approach in the SDN controller (or in any other centralized control plane system) that gathers all necessary information and makes decisions on the spectrum that is allocated to each leaf node (Figure 8.1-2(a))
- A decentralized mixed strategy game (MSG), includes a model within each agent that is used for local decision making based on the knowledge of the traffic and the spectral allocations of all the agents in the P2MP system (Figure 8.1-2(b)).
- A collaborative Multi Agent system (MAS) approach, where decision making is carried out considering the spectrum information currently available in the agent. The agents decide their own spectral allocation based on such prediction and from the spectral allocations previously shared by the agents and update their allocations to the rest of the agents when some change (SC activation/deactivation) is performed (Figure 8.1-2(c)). Two different options have been considered for this alternative:
    - Distributed deterministic MAS (DD-MAS): Tx agents use a deterministic algorithm for spectral allocation based on the capacity required for the local transponder, as well as the current spectral allocations composed of the information shared by the other Tx agents.
    - Multiagent Reinforcement Learning (MARL): This approach inherits the inter-agent communication capabilities and other functions from the DD-MAS one, except for capacity prediction, which here is implemented using Deep Reinforcement Learning (DRL).

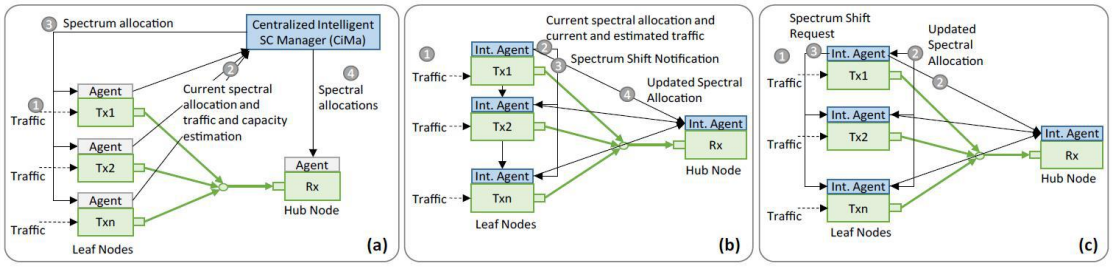

Figure 8.1-2 Centralized (a), decentralized mixed strategy game (b), and collaborative multiagent system (c) approaches.

Extended details of the algorithms and workflows of each of the approaches can be found in available in deliverables and outcomes carried out in WP4, as well as in [Sha24].

8.1.2 First results

To test the different methods proposed, a simulator was implemented in Python, providing the needed distributed framework for implementing each approach. The MP2P connection was modeled by assuming the Rx can support a total of 16 SCs with a capacity of 25 Gb/s each, while Txs support 4 SCs. Therefore, we can configure a maximum of four Txs with a fixed capacity of 100 Gb/s (four SCs). The performances of the different approaches are compared considering more than four Txs in the MP2P connection.

Two basic traffic profiles have been considered: a residential profile and a data center to data center (DC2DC) one [Vel17]. The profiles are shown in Figure 8.1-3(a) normalized for a period of one day, where we observe that they reach their maximum value at different times and converge to similar values near the end of the day. The actual traffic entering each of the Txs is a unique combination of the basic traffic profiles scaled to be within the range [10–100] Gb/s and values have a granularity of 0.1 sample/s. For illustrative purposes, Figure 8.1-3(b) presents some traffic mixes for five Txs. In the example, we observe that some Txs receive similar traffic patterns, e.g., Tx1 and Tx3. The traffic mixes are scaled considering a maximum load, described as the maximum of the sum of all traffic at a given time over the total capacity of the P2MP connection, i.e., 16_25D400 Gb/s. Figure 8.1-3(c) shows the aggregated traffic for the traffic in Fig. 4(b), where the maximum value is 280 Gb/s, i.e., 70% load. The color bar helps visualize traffic load and it will be used in other graphs. In general, the load is higher at the beginning and the end of the day with a large decrease in traffic in between, as shown by the red markers in Fig. 4(c). For performance comparison, we consider maximum loads ranging from 70%–95%.

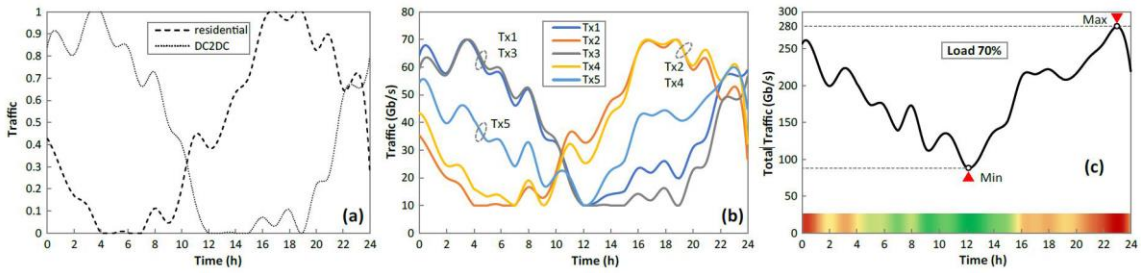

Figure 8.1-3 Residential and DC2DC traffic profiles (a), example of traffic mixes in a MP2P connection (b), and aggregated traffic in a MP2P connection(c).

The comparison of the different approaches is summarized in Figure 8.1-4 for one day of operation. To further understand the behavior of each approach and the loss that they incur, let us examine the performance under 82% traffic load with six leaf nodes, where all approaches operate with some loss.

Starting from traffic loss [Figure 8.1-4(a)], we observe that the MSG approach produces large spikes of loss at the beginning and near the end of the period when the traffic load is higher. However, small spikes of loss can also be observed around 10 h, 15 h, and 21 h, even though the traffic low is not that much high. In contrast, DD-MAS and MARL approaches produce loss when the traffic load is high, i.e., at the beginning of the period (DD-MAS) and the end of the period (both DD-MAS and MARL). The centralized approach shows also some loss at the end of the period, although slightly smaller than those of the deterministic approaches.

To further understand the reasons behind these losses, Figure 8.1-4(b) depicts the total number of SCs used by all the leaves over the period. All methods use a similar number of SCs with most differences presenting themselves during high load periods, when the centralized approach uses fewer SCs followed by the MARL one. This could be a consequence of the definition of the objective function in the centralized approach, which aims to minimize the number of active SCs; such an objective is not enforced in the distributed approaches. Interestingly, we observe that the DRL-based capacity prediction in the MARL approach in fact reduces the capacity of its spectral allocation—it uses fewer SCs compared to the DDMAS one, especially at higher loads—which can explain its lower loss. On the opposite, the MSG approach shows spiked increases in the number of SCs, as highlighted in Figure 8.1-4(b). Overall, that approach shows a larger number of fluctuations in the number of SCs activated and deactivated, which can explain some of the loss observed. During the periods of higher loss (22–24 h), all approaches activate all available SCs in the spectrum. Note that during these periods, capacity increments requested by the leaf nodes are less likely to be fulfilled, which results in traffic loss.

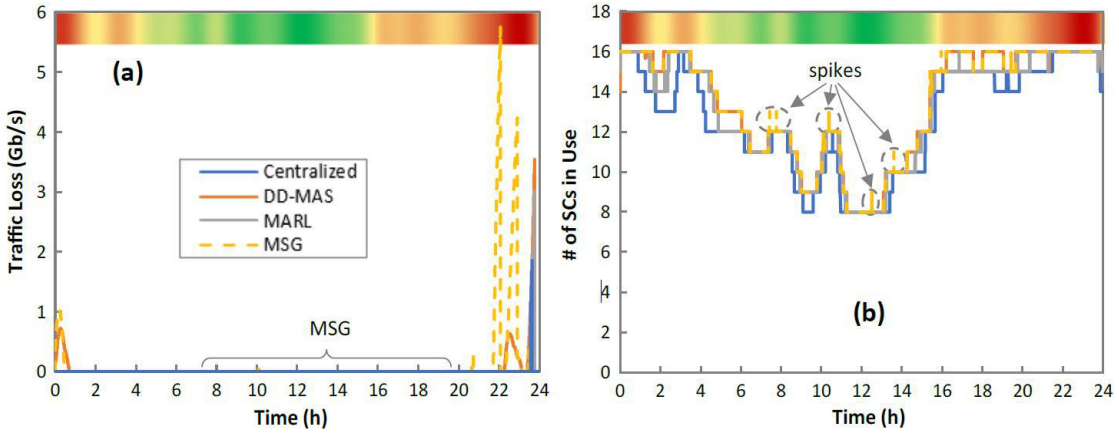

Figure 8.1-4 Residential and DC2DC traffic profiles (a), example of traffic mixes in a MP2P connection (b), and aggregated traffic in a MP2P connection(c).

In conclusion, four approaches supporting near-real-time SC operation in a P2MP connection have been presented and their performances compared. Distributed approaches eliminate the need for centralized decision making by moving decision making to the agents of the transponders participating in the specific P2MP connection. The performance of the distributed approaches is, in general, below that of the centralized one, and MARL is the approach with the best performance among the distributed ones. The most significant finding, however, is that dynamic DSCM allocation, regardless of the method, allows reducing the number of active SCs during extended periods throughout the day. This reduction is directly linked to energy consumption costs. As future work, we plan to translate these results into OPEX reduction evaluation, to quantify the energy consumption savings of both dynamic DSCM allocation and oversubscription in MP2P optical connections, compared to fixed and statically planned operation.

8.2 Optical Line System Automatic Setup (Amplifier Configuration)

In a Dense Wavelength Division Multiplexing (DWDM) network that uses EDFAs, managing amplifiers can be challenging. EDFAs can function in either Constant Gain mode or Constant Power mode. Constant Power mode is often preferred because it allows direct control over the power levels of each wavelength. However, this mode necessitates precise, real-time knowledge of the number of channels entering the amplifier. This requires reliable methods for channel counting, such as using OCM or WSS.

On the other hand, when operating in Constant Gain mode, there is no need to know the exact number of channels entering the EDFA. The amplifier is configured to match the gain with the optical losses of the preceding span, including any passive components. The challenge here lies in accurately determining these losses during network setup and tracking any variations over time. In Constant Gain mode, any inaccuracies in setting the EDFA's gain directly affect the

received power and OSNR of the channels. In a long chain of amplifiers, these errors can accumulate, potentially causing some channels to fall outside the receiver's acceptable range.

In summary, operating in Constant Power mode is preferred in DWDM networks where real-time monitoring and channel counting are feasible. This is typically the case in highly engineered DWDM networks, such as long-haul core networks, where monitoring equipment like OCM is installed at every node. In scenarios where such monitoring is not available, Constant Gain mode becomes advantageous. However, it is crucial to have a reliable method for estimating, in real time, the appropriate gain setting for each amplifier. If this is not done, some channels may end up with received power levels or OSNR that fall outside the acceptable operating range. This issue is illustrated in the accompanying simulation (Figure 8.2-1), which shows the impact of improper gain setting on both received power and OSNR. The heights of the bars in these histograms represent the probability of various received power levels or OSNRs (shown on the x-axis). With incorrect gain settings, the likelihood of deviating from the design parameters is significantly increased.

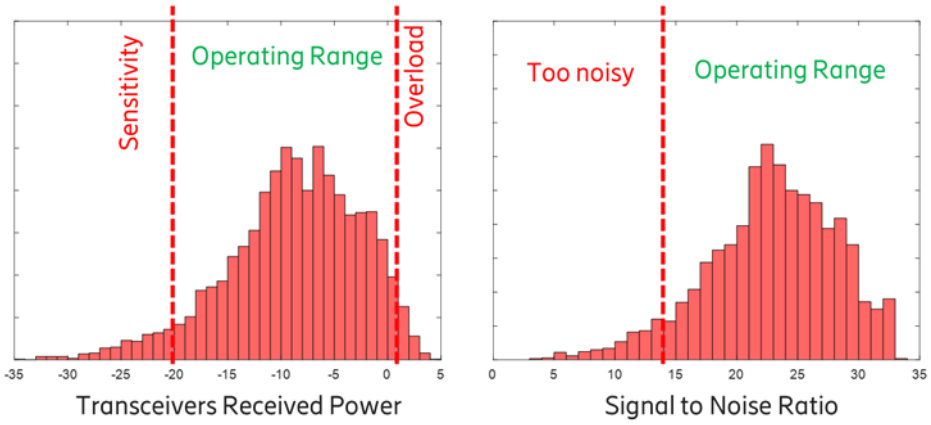

Figure 8.2-1 Simulation that sets the gain by improperly influencing both the received power and the optical signal-to-noise ratio (OSNR).

In this section, we discuss simpler DWDM networks that lack monitoring modules and thus operate in Constant Gain mode. This scenario is common in IP-over-WDM networks within Access/Aggregation and Metro areas. In these networks, amplification is sometimes necessary to compensate for span losses and the losses introduced by OADM filters or splitters. However, including channel monitoring elements everywhere would be too costly for these budget-sensitive network segments.

Fortunately, we can now utilize OLCs, akin to SDN controllers, which connect to all nodes in the optical network through a DCN. OLCs provide a level of automation that significantly benefits operators and improves serviceability. They can monitor optical parameters across all network nodes and, using this data, execute control actions and make parameter adjustments—such as modifying EDFA gain—based on sophisticated algorithms and Artificial Intelligence techniques.

In DWDM optical networks operating in Constant Gain mode, setting the EDFA gain typically relies on measuring the span loss before the amplifier. This can be achieved in two main ways:

1. Using power monitor photodiodes: These are placed at the transmitter and receiver ends of the EDFA. The method involves calculating the difference between the total optical power output from the previous EDFA and the power received by the next EDFA. This difference reflects the cumulative losses the optical signal experiences along the link.

   Issue: This approach is influenced by the presence of added or dropped channels, which can skew the end-to-end loss measurement.

2. Using an Optical Supervisory Channel (OSC): The OSC, commonly used to connect all nodes to a DCN, can help estimate span loss. It is typically inserted after one EDFA and extracted before the next, using specific filters. The span loss is determined by the difference in power measured at the OSC's transmitter and receiver, accounting for the insertion loss of add/drop filters and wavelength differences.

   Issue: OSC transceivers often have poor power measurement accuracy, with errors of ±2 dB. This can lead to a total error in span loss estimation of up to ±4 dB.

Alternatively, in more cost-effective setups without monitoring capabilities, a simpler method can be used:

3. Manual measurement and adjustment: Upon setup, operators use appropriate instruments, like a portable laser source and a power meter, to measure the exact loss of each span and set each EDFA accordingly. Adjustments are then made manually when necessary, such as during span aging alarms or after link repairs following faults.

   Issue: This method does not automatically adapt to span aging or other network changes over time. It also requires manual intervention, which contradicts serviceability principles, increases operational costs for operators, and necessitates skilled field personnel.

The solution relies on the traffic matrix and the DWDM network's topology. It begins with an approximate estimate of the span loss, which serves as the initial basis for determining the optimal gain. Additionally, it requires measurements of the received power for all channels at every point where they are added or dropped, using the power monitors available on transceivers.

This approach estimates the optimal gain for each amplifier in the network to minimize the difference between the actual and target receiver power for all channels at any drop node. It also ensures that all channels remain within the receiver's acceptable range, with a specified margin.

A crucial aspect of this method is that the target receiver power is not just any value within the acceptable range. Instead, it is the expected average value by design for the specific node and

transceiver type. This ensures that system parameters, including Optical Signal-to-Noise Ratio and launch power, naturally converge to their intended values.

In conclusion, implementing this method, network operators can achieve a more accurate and automated calibration of amplifier gains, enhancing overall network performance and reliability. This approach reduces the need for manual intervention and allows the network to dynamically adapt to changing conditions, ensuring optimal performance across various network segments.

8.3 NUMERICAL EVALUATION OF SOFT FAILURE MANAGEMENT

In this section, the main results of the different methods for soft-failure management developed in the OCATA digital twin are presented. Specifically, the results Illustrate the performance of models and algorithms that exploit IQ constellation features analysis for soft-failure detection, identification, and severity estimation. The extended details of the different algorithms, as well as other related performance evaluation results can be found in [Dev24], as well as they will be presented in WP4 deliverables.

8.3.1 Summary of methods

Figure 8.3-1 illustrates several possible soft failures affecting a lightpath. Figure 8.3-1(a) corresponds to the regular network operation, i.e., when the lightpath is not affected by any failure or misconfiguration. Figure 8.3-1(b) illustrates a soft failure in the transmitter, e.g., an extra gain in its booster amplifier leading to an extra transmission power (eTxP). Figure 8.3-1(c) illustrates the impact of an EDFA in the first ROADM with an increased noise figure (iNF). Finally, Figure 8.3-1(d) corresponds to a failure in a WSS in the first ROADM that produces Filter Shift (FS) or Filter Tightening (FT) on the optical signal.

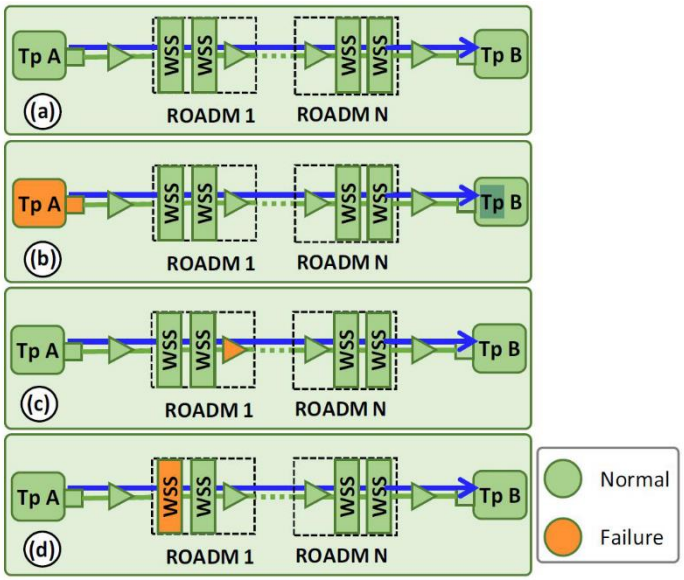

Figure 8.3-1 Considered use cases for failure management: (a) normal operation, (b) TP failure, (c) EDFA failure, (d) WSS failure.

Following, the main methods for failure management based on the analysis of IQ constellation samples are briefly described:

- For failure detection, the expected IQ constellation features are generated using the model for the lightpath (available in the OCATA DT), and the features from the received constellation are compared by means of a distance function. These values, together with lightpath's details (i.e., number of ROADMs and total distance) are given as inputs to a binary classifier. Whenever a failure is pinpointed for more than nth consecutive optical constellation measurements, a positive detection is triggered.
- For failure identification/localization, a set of hierarchical binary classifiers trained offline for each of the failures are used. Specifically, after positive failure detection, a classifier for identifying whether a failure is eTxP or not is used. If eTxP is not detected, then two models for identifying filter (FS/FT) and amplifier (iNF) soft failures are executed. A positive identification happens when only one of the two models detects a soft-failure whereas, when either both models detect a soft-failure or neither of them do, the soft-failure remains unidentified.

8.3.2 Results

A simulator of a digital coherent system has been implemented in MATLAB and employed to model the optical layer. In particular, we consider an 11-channel wavelength-division multiplexed (WDM) system, where each channel is modulated with 16-QAM and operates at 64 GBd. Additional details of the simulation environment can be found in [Dev24]. The simulator allows reproducing the failure scenarios sketched in Figure 8.3-1, where failures are introduced as soft failures and gradually evolve to hard failures. In particular, we assume a linear evolution

of the magnitude of soft-failures starting from a small value at normalized time 1 until the soft-failure becomes a hard-failure (normalized time 2).

Figure 8.3-2(a) shows the accuracy achieved when detecting the degradations that affect an example lightpath of 1440 km for the considered failure scenarios, i.e., eTxP (a), iNF (b), FS (c), and FT (d). The results are generalized in Figure 8.3-2(b), where the failure detection times obtained for different LP configurations are plotted as a function of the lightpaths total distance. As can be observed, similar normalized times can be observed for the different distances. Regarding the different types of failures, FT and eTxP are detected faster than FS and iNF.

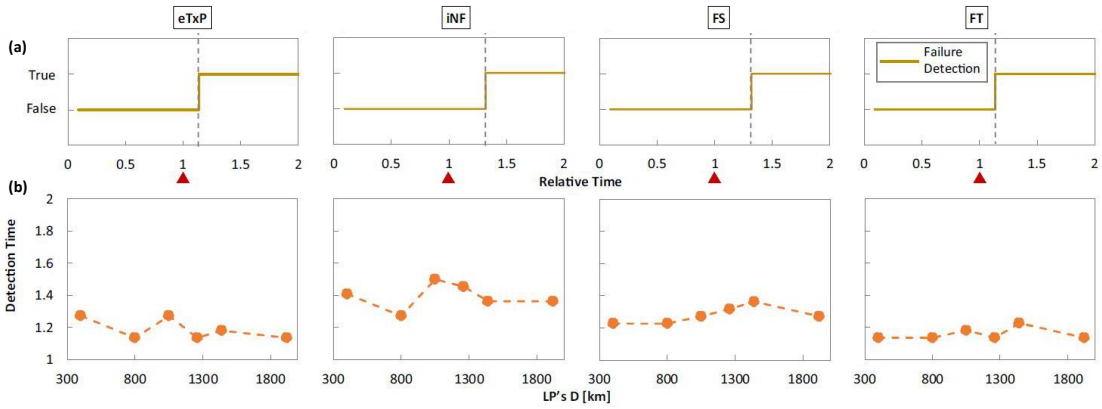

Figure 8.3-2 Evaluation of failure detection for the considered soft failures. Failure detection (a) versus time for an example lightpath (1440 km) and (b) versus lightpath distance.

Table 8.3-1 shows the anticipation time for detection and identification before the soft failure become a hard failure. For identification, we consider the earliest time where identification accuracy is larger than 90%. The first columns present the values in the aforementioned normalized time scale. Then, to compute absolute time values, we assume three different evolution scenarios, i.e., the absolute time between time 1 and time 2 in the normalized scale. The scenarios of evolution are: 1 week (slow evolution), 1 day (medium evolution), and 1 hour (fast evolution). As can be observed, even in the worst case (FS in fast 1-hour evolution), detection, localization and identification are performed several minutes before the hard failure.

Table 8.3-1 Detection and identification times for different failure evolution scenarios.

Failure Type	Normalized		1-week evolution		1-day evolution		1-hour evolution	
	Detect.	Identif. (Acc >90%)	Detect.	Identif. (Acc >90%)	Detect.	Identif. (Acc >90%)	Detect.	Identif. (Acc >90%)
eTP	0.85	0.60	143 h	100 h	20 h	14 h	51 min	36 min
iNF	0.70	0.40	118 h	67 h	17 h	9 h	42 min	24 min
FS	0.65	0.30	109 h	50 h	15 h	7 h	39 min	18 min
FT	0.85	0.30	143 h	50 h	20 h	7 h	51 min	18 min

In conclusion, the results clearly validate the KPI 8.3 target, i.e., optical layer digital twin for gradual soft-failure detection and localization with at least 1min before major impact on the service, and an accuracy higher than 90% in soft-failure identification.

9 CONCLUSIONS

This deliverable is the first of a series of two dedicated to the technical-economic studies carried out to assess the architectural and technological solutions proposed by the SEASON project.

The approach used was to select among the KPIs of the project those that have a relevance to the technical and economic aspects. The selected KPIs (ten in total) and the summary report on the degree of progress of their achievement in the project are included in section 2.

The studies supporting the progress of the KPIs are reported in sections 3 to 8. Some of the studies have been concluded, others have obtained partial results and require more work to be finished, others have defined the scenario set-up, the baseline solution for comparison and the innovative solution that includes one or more architectural or technological innovations proposed by SEASON.

As detailed in section 2, out of the ten selected KPIs, two (KPI 7.1 and KPI 8.3) have been completely achieved. Five KPIs (KPI 2.2, 3.2, 4.2, 4.3, and 8.1) are partially achieved requiring further investigation during the final phase of WP2 activities to fully assess and validate the corresponding project KPI. The remaining three KPIs (KPI 3.1, 6.1, and 6.2) have not yet been achieved.

The D2.3 deliverable planned for M32 of the project (August 2025) will contain all the studies presented in this document in their final version with the complete and final report on the degree of achievement of the KPIs that it will have been obtained during the last period of WP2 work.

GLOSSARY

Acronym	Description
µBS	Micro Base Station
A/D	Add/Drop
ACO	Access Central Office
AE	Auto-Encoders
ASE	Amplified Spontaneous Emission
ASV	Available Spectrum Vector
B5G	Beyond 5G
BBU	Baseband Unit
BDM	Band Division Multiplexing
BER	Bit Error Rate
BH	Backhaul
BPSK	Binary Phase-Shift Keying
BS	Base Station
BSC	Band-Spectrum-Core
BSDM	Band and Spatial Division Multiplexing
BuMFP	Bundled Multi-Fiber Pair
CAGR	Compound Average Growth Rate
CAPEX	Capital Expenditure
CD	Cladding Diameter
CDC	Colorless, Directionless, and Contentionless
CFM	Closed-Form Transmission Models
CO	Central Office
COR	Central Office Router/Switch
C-RAN	Cloud RAN
CSB	Core-Spectrum-Band
CSR	Cell Site Router/Switch
CU	Centralized Unit
DC	Telco EDGE Central Office
DCN	Data Communication Network
DD-MAS	Distributed deterministic MAS
DEMUX	Demultiplexer
DFA	Doped Fiber Amplifiers
DGE	Dynamic Gain Equalizer
DPU	Data Processing Unit

DRL	Deep Reinforcement Learning
DSCM	Digital Subcarrier Multiplexing
DSP	Digital Signal Processing
DT	Digital Twin
DU	Distributed Unit
DWDM	Dense Wavelength Division Multiplexing
e2e	End-to-End
EDFA	Erbium-Doped Fiber Amplifier
EGN	Enhanced GN
eMBB	Enhanced Mobile Broadband
EON	Elastic Optical Networks
ER	Extended Reach
eTxP	Extra Transmission Power
FDR	Flexibility Decision Rules
FEC	Forward Error Correction
FH	Fronthaul
FLP	Flat Launch Power
FS	Filter Shift
FT	Filter Tightening
GA	Genetic Algorithm
GGN	Generalized GN
GN	Gaussian Noise
GNN	Graph Neural Network
GNPy	Gaussian Noise Model in Python
GSNR	Generalized Signal-to-Noise Ratio
HGA	Hybrid Genetic Algorithm
HPO	Hyper-Accelerated Power Optimization
I/O	Input/Output
ICXT	Inter-Core Crosstalk
IL	Insertion Loss
ILA	In-Line Amplifier
ILP	Integer Linear Programming
IMDD	Intensity Modulated Direct Detection
iNF	Increased Noise Figure
IP	Internet Protocol
IPoWDM	IP-over-WDM
IQ	In-phase and Quadrature
ISRS	Inter-Channel Stimulated Raman Scattering
JPNB4812	Japanese Backbone Network

KPI	Key Performance Indicator
KSP	K-Shortest Paths
LCI	Line Card Interfaces
LP	Lightpath
LT	Long Term
MARL	Multiagent Reinforcement Learning
MAS	Multi Agent System
MB	Multi-Band
MB-EON	Multi-band EON
MBoSDM	Multi-band over Spatial Division Multiplexing
MBS	Macro Base Station
MBT	Multi-Band Transmission
MCC	Mode Coupling Coefficient
MCF	Multi-Core Fiber
MCI	Multi-Channel Interference
MH	Mid Haul
MIMO	Multiple Input Multiple Output
mIoT	Massive Internet of Things
ML	Machine Learning
MP2P	Multi-point to Point
MPLS	Multiprotocol Label Switching
MSG	Mixed Strategy Game
MT	Medium Term
MUX	Multiplexer
NCO	National Central Office
NF	Noise Figure
NIC	Network Interface Card
NLI	Nonlinear Impairments
NN	Neural Network
NSGA	Non-dominated Sorting Genetic Algorithm
O/E/O	Optical-Electrical-Optical
OADM	Optical Add-Drop Multiplexer
OCATA	Optical Constellation Analysis
OCM	Optical Channel Monitoring
OLC	Open-Levels Control Plane Architecture
OLS	Optical Line System
OLT	Optical Line Terminal
ONU	Optical Network Unit
OPEX	Operating Expenses

O-RAN	Open-RAN
OSC	Optical Supervisory Channel
OSNR	Optical Signal-to-Noise Ratio
OTDR	Optical Time-Domain Reflectometer
OTN	Optical Transport Network
P2MP	Point-to-Multipoint
P2MP-WP	Point-to-Multipoint with Pre-Aggregation
P2P	Point-to-Point
PCC	Power Coupling Coefficient
PDU	Protocol Data Unit
PEP	Power Evolution Profile
PON	Passive Optical Network
PRB	Physical Radio Block
QAM	Quadrature Amplitude Modulation
QoS	Quality of Service
QoT	Quality-of-Transmission
R&D	Research and Development
R&S	Route and Select
RAN	Radio Access Network
RCO	Regional Central Office
RFA	Raman Fiber Amplifier
RIC	RAN Intelligent Controller
RL	Reinforcement Learning
RMSCA	Routing, Modulation, Spectrum, and Core Assignment
ROADM	Reconfigurable Optical Add-Drop Multiplexer
RU	Radio Unit
Rx	Receiver
SAM	Spectrum Allocation Method
SC	Subcarrier
SD-EON	Software-Defined EON
SDM	Spatial Division Multiplexing
SDN	Software-Defined Network
SNR	Signal-to-Noise Ratio
SOHO	Small Office/Home Office
S-OXC	Spatial Optical Cross-Connect
SPM	Self-Phase Modulation
SPNB3014	Spanish Backbone Network
SR	Short Reach
SRS	Stimulated Raman Scattering

SSFM	Split-Step Fourier Method
SSMF	Standard Single-Mode Fiber
TAWC-MCF	Trench-Assisted Weakly Coupled MCF
TCO	Total Cost of Ownership
TDFA	Thulium-Doped Fiber Amplifiers
TP	Transponder
TR	Transport
TR-A	Transport Aggregation
TR-C	Transport Core
Tx	Transmitter
UC	Unity of Cost
UE	User Equipment
UPF	User Plane Function
URLLC	Ultra-Reliable Low-Latency Communications
US	United States
USB6014	United States of America Backbone Network
vDU	Virtual Distributed Unit
w.r.t.	With Respect to
WC-MCF	Weakly Coupled MCF
WDM	Wavelength Division Multiplexing
WP	Work Package
WSS	Wavelength Selective Switch
XPM	Cross-Phase Modulation
XT-NLI-A-RSA	ICXT- and NLI-Aware Sliceable Routing, Modulation, Core, Band, and Spectrum Allocation

REFERENCES

[Ami22]	A. D'Amico, B. Correia, E. London, E. Virgillito, G. Borraccini, A. Napoli, and V. Curri, "Scalable and disaggregated GGN approximation applied to a c+ l+ s optical network," Journal of Lightwave Technology, vol. 40, no. 11, pp. 3499–3511, 2022.
[Arp24]	Arpanaei, F. *et al*. (2024). Ultra-high-capacity band and space division multiplexing backbone EONs: Multi-core versus multi-fiber. *Journal of Optical Communications and Networking*, *16*(12), H66–H78. Journal of Optical Communications and Networking. https://doi.org/10.1364/JOCN.533086
[Arp24-2]	F. Arpanaei et al., "Enabling seamless migration of optical metro-urban networks to the multi-band: Unveiling a cutting-edge 6d planning tool for the 6g era," JOCN, 2024.
[Arp24-3]	F. Arpanaei, "Datasets for ultra-high-capacity band and space division multiplexing backbone EONs: multi-core versus multi-fiber, Zenodo (2024), https://zenodo.org/records/13759999
[Arp24-4]	F. Arpanaei, K. Ghodsifar, H. Beyranvand, et al., "Hyperaccelerated power optimization in multi-band elastic optical networks,"in Optical Fiber Communication Conference (OFC) (2024), paper Th1I.6.
[Bar21]	L. Barsellotti, F. Alhamed, J. J. Vegas Olmos, F. Paolucci, P. Castoldi and F. Cugini, "Introducing Data Processing Units (DPU) at the Edge [Invited]," International Conference on Computer Communications and Networks (ICCCN), Honolulu, HI, USA, 2022.
[Ber03]	Bertsimas, Dimitris, and Melvyn Sim. "Robust discrete optimization and network flows." *Mathematical programming* 98.1 (2003): 49-71.
[Ber20]	Bernal, A.; Richart, M.; Ruiz, M.; Castro, A.; Velasco, L. Near real-time estimation of end-to-end performance in converged fixed-mobile networks. Elsevier Comput. Commun. 2020, 150, 393–404.
[Bla20]	J. Blank and K. Deb, "pymoo: Multi-objective optimization in Python," IEEE Access 8, 89497–89509 (2020).
[Bos19]	G. Bosco, "Advanced modulation techniques for flexible opticaltra nsceivers: the rate/reach tradeoff," J. Lightwave Technol. 37, 36–49 (2019).
[Bou20]	N. Bouguila and W. Fao, *Mixture Models and Applications*, Springer, 2020.
[Bug21]	H. Buglia *et al*., "Challenges in Extending Optical Fibre Transmission Bandwidth Beyond C+L Band and How to Get There," *2021 International Conference on Optical Network Design and Modeling (ONDM)*, Gothenburg, Sweden, 2021, pp. 1-4.
[Bug22]	H. Buglia, E. Sillekens, A. Vasylchenkova, P. Bayvel, and L. Galdino, "On the impact of launch power optimization and transceiver noise on the performance of ultra-wideband transmission systems [invited]," Journal of Optical Communications and Networking, vol. 14, no. 5, pp.B11–B21, 2022.
[Bug23]	H. Buglia, M. Jarmolovicius, A. Vasylchenkova, E. Sillekens, L. Galdino, R. I. Killey, and P. Bayvel, "A closed-form expression for the gaussian noise model in the presence of inter-channel stimulated raman scattering extended for arbitrary loss and fibre length," Journal of Lightwave Technology, vol. 41, no. 11, pp. 3577–3586, 2023.

[Cap21]	Caputo, C., & Cardin, M.-A. (2021). Analyzing Real Options and Flexibility in Engineering Systems Design Using Decision Rules and Deep Reinforcement Learning. *Journal of Mechanical Design*, *144*(021705). https://doi.org/10.1115/1.4052299
[Cas18]	Casellas, R.; Martínez, R.; Vilalta, R.; Muñoz, R. "Control, Management, and Orchestration of Optical Networks: Evolution, Trends, and Challenges". IEEE J. Light. Technol. 2018, 36, 1390–1402.
[Cas24]	C. Castro et al., "OSNR-Based Hardware Optimization of a Filterless Point-to-Multipoint Network Using Digital Subcarrier Multiplexing," *2024 International Conference on Optical Network Design and Modeling (ONDM),* Madrid, 2024.
[Cas24-2]	C. Castro et al, "Power and Spectral Savings in Metro-Aggregation Networks Exploiting Coherent Point-to-Multipoint Transceivers," *50th European Conference on Optical Communications (ECOC 2024),* Frankfurt, 2024.
[Chr22]	Christou, F., Enderle, T., & Witt, A. (2022). Towards a Hybrid Architecture by Introducing Coherent Pluggable Transceivers in IP-Optical Core Networks with Optical Cross-Connects. *Photonic Networks; 23th ITG-Symposium*, 1–8. https://ieeexplore.ieee.org/abstract/document/9861845
[Chr24]	C. Christodifidis et al., "Feasibility study of Nyquist-switching node to enable mesh ru fronthaul interconnections and flexible 6g mobile network operation," in ONDM 2024, (2024).
[Clo16]	B. Clouet, J. Pedro, N. Costa, et al., "Networking aspects for next-generation elastic optical interfaces," IEEE/OSA J. Opt. Commun. Netw. 8, A116–A125 (2016).
[Cor21]	B. Correia *et al*., "Optical Power Control Strategies for Optimized C+L+S-bands Network Performance," *2021 Optical Fiber Communications Conference and Exhibition (OFC)*, San Francisco, CA, USA, 2021, pp. 1-3.
[Cur22]	V. Curri, "Gnpy model of the physical layer for open and disaggregated optical networking [invited]," Journal of Optical Communications and Networking, vol. 14, no. 6, pp. C92–C104, 2022.
[Dav24]	Davey, R. P., Iqbal, M. A., & Wright, P. D. (2024). ZR 400 Gbit/s and 800 Gbit/s use cases, trials, deployments, and future prospects [Invited]. *Journal of Optical Communications and Networking*, *16*(1), A33–A39. Journal of Optical Communications and Networking. https://doi.org/10.1364/JOCN.499365
[Deb02]	K. Deb, A. Pratap, S. Agarwal, and T. Meyarivan, "A fast and elitist multiobjective genetic algorithm: NSGA-II," IEEE transactions on evolutionary computation 6, 182–197 (2002).
[Dev24]	M. Devigili, M. Ruiz, N. Costa, C. Castro, A. Napoli, J. Pedro, and L.Velasco, "Applications of the OCATA time domain digital twin: from QoT estimation to failure management, " IEEE/OPTICA Journal of Optical Communications and Networking (JOCN), vol. 16, pp. 221-232, 2024.
[Eri22]	Mobility Report 2022. [On-line] https://www.ericsson.com/en/reports-and-papers/mobility-report/reports/june-2022.
[Ess12]	R.-J. Essiambre and R. W. Tkach, "Capacity trends and limits of optical communication networks," Proc. IEEE 100, 1035–1055 (2012).
[Ets22]	ETSI. Fixed 5th Generation Advanced and Beyond; ETSI White Paper, Version 1.0; ETSI: Sophia Antipolis, France, 2022.

[Faz23]	Fazeli, P. (2024, May 23). *OTN Switching: Where Do We Go from Here?* Infinera. https://www.infinera.com/blog/otn-switching-at-a-crossroads-where-do-we-go/tag/optical/
[Fer11]	G. C. M. Ferreira, S. P. N. Cani, M. J. Pontes, and M. E. V. Segatto, "Optimization of distributed Raman amplifiers using a hybrid genetic algorithm with geometric compensation technique," IEEE Photonics J. 3, 390–399 (2011).
[Fer19]	A. Ferrari, D. Pilori, E. Virgillito, et al., "Power control strategies in C+L optical line systems," in Optical Fiber Communication Conference (OFC) (2019), paper W2A.48.
[Gav21]	Gavras, A.; Bulakci, Ö.; Gramaglia, M.; Iordache, M.; Ghoraishi, M.; Garcia, A.; Cogalan, T.; Gutiérrez, J.; Tzanakaki, A.; Warren, D.; Li, X.; et al. 5G PPP Architecture Working Group—View on 5G Architecture; Version 4.0; 2021.
[Gum23]	Gumaste, A., Pedro, J., Momtahan, P., & Bock, H. (2023). Optimal Line-Rates for IP-over-DWDM in Metro and Core Networks: Comparison of ZR+ and Xponder Architectures. *2023 Optical Fiber Communications Conference and Exhibition (OFC)*, 1–3. https://doi.org/10.1364/OFC.2023.Tu2D.1
[Guo24]	N. Guo, G. Shen, N. Deng, and B. Mukherjee, "Can channel power optimization with GSNR flatness maximize capacities of C+L-band optical systems and networks?" J. Light. Technol. 42, 5506–5521 (2024).
[Ham19]	F. Hamaoka *et al*., "Ultra-Wideband WDM Transmission in S-, C-, and L-Bands Using Signal Power Optimization Scheme," in *Journal of Lightwave Technology*, vol. 37, no. 8, pp. 1764-1771, 15 April15, 2019.
[Hay12]	T. Hayashi, T. Taru, O. Shimakawa, et al., "Uncoupled multi-core fiber enhancing signal-to-noise ratio," Opt. Express 20, B94–B103 (2012).
[Hay19]	T. Hayashi, T. Nagashima, T. Morishima, et al., "Multi-core fibers for data center applications," in European Conference on Optical Communication (ECOC) (2019).
[Her23]	J. A. Hernandez et al., "Clustering-based dynamic bandwidth allocation for point-to-multipoint coherent optics," in Optical Fiber Communication Conference, (Optica Publishing Group, 2023), pp. Tu2D–5.
[Hos23]	Hosseini, Mohammad M., et al. "Optimized design of filterless horseshoe networks exploiting point-to-multipoint coherent transceivers." *Journal of Optical Communications and Networking* 15.9 (2023): 569-578.
[Hos24]	Hosseini, Mohammad M., et al. "Optimized design of horseshoe-and-spur filterless networks leveraging point-to-multipoint coherent pluggable transceivers." *Journal of Optical Communications and Networking*, 2024.
[Inf21]	Infinera, "The seven vectors of ROADM evolution" (2021), https://www.infinera.com/wp-content/uploads/The-Seven-Vectors-of-ROADM-Evolution-0302-WP-RevA-1121.pdf
[Jia11]	H. M. Jiang, K. Xie, and Y. F. Wang, "Novel design of flat gain spectrum Raman fiber amplifiers based on ant colony optimization," IEEE Photonics Technol. Lett. 23, 1823–1825 (2011).
[Jia11-2]	H. M. Jiang, K. Xie, and Y. F. Wang, "Optimization of pump parameters for gain flattened Raman fiber amplifiers based on artificial fish school algorithm," Opt. Commun. 284, 5480–5483 (2011).
[Jia12]	H. M. Jiang, K. Xie, and Y. F. Wang, "Flat gain spectrum design of Raman fiber amplifiers based on particle swarm optimization and average power analysis technique," Opt. Lasers Eng. 50, 226–230 (2012).

[Jia23]	Y. Jiang, A. Nespola, A. Tanzi, S. Piciaccia, M. R. Zefreh, F. Forghieri, and P. Poggiolini, “Experimental test of a uwb closed-form egn model,”in 49th European Conference on Optical Communications (ECOC 2023), 2023.
[Jia23-2]	Y. Jiang, G. Bosco, A. Nespola, A. Tanzi, S. Piciaccia, M. R. Zefreh, F. Forghieri, and P. Poggiolini, “Experimental test of a uwb closed-form egn model,” in 2023 IEEE Photonics Conference (IPC), 2023, pp. 1–2.
[Jia24]	Y. Jiang, J. Sarkis, A. Nespola, et al., “Optimization of long-haul C+L+S systems by means of a closed form EGN model,” IEEE Photonics Technol. Lett. pp. 1–1 (2024).
[Kon06]	A. Konak, D. W. Coit, and A. E. Smith, “Multi-objective optimization using genetic algorithms: A tutorial,” Reliab. Eng. & Syst. Saf. 91, 992–1007 (2006). Special Issue - Genetic Algorithms and Reliability.
[Lag21]	S. Lagén et al., “Modulation Compression in Next Generation RAN: Air Interface and Fronthaul Trade-offs,” IEEE Comm. Mag., vol. 59, pp. 89-95, 2021.
[Las23]	C. Lasagni, P. Serena, A. Bononi, and J.-C. Antona, “A generalized raman scattering model for real-time snr estimation of multi-band systems,” Journal of Lightwave Technology, vol. 41, no. 11, pp. 3407–3416, 2023.
[Liu04]	X. Liu and Y. Li, “Optimizing the bandwidth and noise performance of distributed multi-pump Raman amplifiers,” Opt. Commun. 230, 425–431(2004).
[Liu04-2]	X. Liu, J. Chen, C. Lu, and X. Zhou, “Optimizing gain profile and noise performance for distributed fiber Raman amplifiers,” Opt. express 12, 6053–6066 (2004).
[Lun21]	H. Lun, X. Liu, M. Cai, Y. Zhang, R. Gao, W. Hu, L. Yi, and Q. Zhuge, “Machine-learning-based telemetry for monitoring long-haul optical transmission impairments: methodologies and challenges,” Journal of Optical Communications and Networking, vol. 13, no. 10, pp. E94–E108, 2021.
[Mar17]	D. M. Marom, P. D. Colbourne, A. D’errico, et al., “Survey of photonic switching architectures and technologies in support of spatially and spectrally flexible optical networking [Invited],” J. Opt. Commun. Netw. 9, 1–26 (2017).
[Mar24]	Martínez, R. *et al*. (2024). “Autonomous Control Operations for Energy-Efficient Packet Optical Networks.” *2024 24th International Conference on Transparent Optical Networks (ICTON)*, 1–4. https://doi.org/10.1109/ICTON62926.2024.10648263
[Mou21]	U. C. de Moura, D. Zibar, A. M. Rosa Brusin, A. Carena and F. Da Ros, "Generalization Properties of Machine Learning-based Raman Models," *2021 Optical Fiber Communications Conference and Exhibition (OFC)*, San Francisco, CA, USA, 2021, pp. 1-3.
[Msa24]	Open-ROADM-MSA, “Open ROADM MSA device white paper (v13.1)” (Open ROADM MSA GitHub Repository, 2024), https://github.com/OpenROADM.
[Nap18]	A. Napoli, N. Costa, J. K. Fischer, J. Pedro, S. Abrate, N. Calabretta, W. Forysiak, E. Pincemin, J. P. F. Gimenez, C. Matrakidis, G. Roelkens, and V. Curri, "Towards multiband optical systems," in *Advanced Photonics 2018 (BGPP, IPR, NP, NOMA, Sensors, Networks, SPPCom, SOF)*, OSA Technical Digest (online) (Optica Publishing Group, 2018), paper NeTu3E.1.
[Now24]	Nowell, M., & Roberts, E. (2024). *400G, 800G, and Terabit Pluggable Optics: What you need to know*. Cisco live. https://www.ciscolive.com/c/dam/r/ciscolive/global-event/docs/2024/pdf/BRKOPT-2699.pdf
[OFLink]	OF-LINK COMMUNICATIONS CO., LTD , “Filter WDM C/L Band Datasheet.” [Online]. Available:https://www.of-link.com/C-L-Band-Filter-WDM_p308.html.

[OOPT-PSE]	OOPT-PSE team within the Telecom Infra Project, “Github repository of GNPy,” [Online]. Available:https://github.com/Telecominfraproject/oopt-gnpy.
[OpenROADM]	OpenROADM, “The open roadm multi-source agreement (MSA). [online] available: http://www.openroadm.org,”.
[Ora21]	O-RAN ALLIANCE Specification O-RAN.WG9.XTRP-REQ-v01.00, O-RAN Open Xhaul Transport Working Group 9, Xhaul Transport Requirements, Feb. 2021. [online] https://orandownloadsweb.azurewebsites.net/specifications
[Ora25]	O-RAN Alliance. Available online: https://www.o-ran.org/ (accessed on 10 January 2025).
[Par24]	Park, E. (2024, September 20). *Expanding Capacity and Reach with a New Generation of Coherent Pluggables*. Acacia. https://acacia-inc.com/blog/expanding-capacity-and-reach-with-a-new-generation-of-coherent-pluggables/
[Pat23]	Patri, S. K. (2023). *Planning and Control of Disaggregated Quantum-Safe Optical Transport Networks*. Technical University of Munich.
[Ped22]	J. Pedro, N. Costa, and S. Sanders, “Cost-effective strategies to scale the capacity of regional optical transport networks,” Journal of Optical Communications and Networking, vol. 14, no. 2, pp. A154–A165, 2022.
[Per02]	V. E. Perlin and H. G. Winful, "Optimal design of flat-gain wide-band fiber Raman amplifiers," in *Journal of Lightwave Technology*, vol. 20, no. 2, pp. 250-254, Feb. 2002.
[Per18]	G. Perez, J. A. Hernandez, and D. Larrabeiti, “Fronthaul network modeling and dimensioning meeting ultra-low latency requirements for 5G”, IEEE/OPTICA J. of Optical Communications and Networking, vol. 10, pp. 573-581,2018.
[Pog14]	P. Poggiolini, G. Bosco, A. Carena, V. Curri, Y. Jiang, and F. Forghieri, “The gn-model of fiber non-linear propagation and its applications,” Journal of Lightwave Technology, vol. 32, no. 4, pp. 694–721, 2014.
[Pog17]	P. Poggiolini and Y. Jiang, “Recent advances in the modeling of the impact of nonlinear fiber propagation effects on uncompensated coherent transmission systems,” Journal of Lightwave Technology, vol. 35, no. 3, pp. 458–480, 2017.
[Pog22]	P. Poggiolini and M. Ranjbar-Zefreh, “Closed form expressions of the nonlinear interference for UWB systems,” in European Conference on Optical Communication (ECOC) (2022).
[Ran20]	M. Ranjbar-Zefreh and P. Poggiolini, “A real-time closed-form model for nonlinearity modeling in ultra-wide-band optical fiber links accounting for inter-channel stimulated raman scattering and co-propagating raman amplification,” 2020, arXiv:2006.03088,[eess.SP].
[Rui14]	M. Ruiz and L. Velasco, “Performance evaluation of light-tree schemes in flexgrid optical networks,” IEEE Commun. Lett. 18,1731–1734 (2014).
[Rui22]	M. Ruiz, D. Sequeira, and L. Velasco, “Deep learning-based real time analysis of lightpath optical constellations,” J. Opt. Commun. Netw. 14, C70–C81 (2022).
[Rui22-2]	M. Ruiz, L. Velasco, D. Sequeira, "Optical Constellation Analysis (OCATA)", https://doi.org/10.34810/data146, CORA Repositori de Dades de Recerca, V2.
[Rui23]	Ruiz, M.; Hernandez, J.A.; Quagliotti, M.; Hugues-Salas, E.; Riccardi, E.; Rafel, A.; Velasco, L.; De Dios, O.G. Network Traffic Analysis under Emerging Beyond-5G Scenarios for Multi-Band Optical Technology Adoption. IEEE/OPTICA J. Opt. Commun. Netw. (JOCN) 2023, 15, F36–F47.

[Rui24]	M. Ruiz, L. Velasco, M. Devigili, M. B. Shariati, K. J. Fischer; C. M. Santos, "Simulation and experimental data of frequency domain and time domain optical signal measurements for optical network digital twins", https://doi.org/10.34810/data1143, CORA Repositori de Dades de Recerca, V1.
[Sad21]	R. Sadeghi *et al*., "Performance Comparison of Translucent C-band and Transparent C+L-band Network," *2021 Optical Fiber Communications Conference and Exhibition (OFC)*, San Francisco, CA, USA, 2021, pp. 1-3.
[Sai13]	K. Saitoh and S. Matsuo, "Multicore fibers for large capacity transmission," Nanophotonics 2, 441–454 (2013).
[Sak13]	J. Sakaguchi, B. J. Puttnam, W. Klaus, et al., "305 Tb/s space division multiplexed transmission using homogeneous 19-core fiber," J.Lightwave Technol. 31, 554–562 (2013).
[Sar21]	Sarikaya, E.; Onur, E. Placement of 5G RAN Slices in Multi-tier O-RAN 5G Networks with Flexible Functional Splits. In Proceedings of the International Conference on Network and Service Management (CNSM), Virtual, 25–29 October 2021.
[SeaD2.1]	SEASON Project, "Definition of use cases, requirements and reference network architecture," (2024). Deliverable D2.1.
[SeaD3.2]	SEASON Project, "Optical systems enabling ultra-high-capacity access/metro networks," (2025). Deliverable D3.2.
[SeaD5.1]	SEASON Project, "SEASON Project, "Optical systems enabling ultra-high-capacity access/metro networks," (2045). Deliverable D5.1.
[Sem19]	D. Semrau, E. Sillekens, R. I. Killey, and P. Bayvel, "A modulation format correction formula for the gaussian noise model in the presence of inter-channel stimulated raman scattering," Journal of Lightwave Technology, vol. 37, no. 19, pp. 5122–5131, 2019.
[Sem20]	D. Semrau, E. Sillekens, R. I. Killey and P. Bayvel, "The Benefits of Using the S-Band in Optical Fiber Communications and How to Get There," *2020 IEEE Photonics Conference (IPC)*, Vancouver, BC, Canada, 2020, pp. 1-2
[Seq18]	D. G. Sequeira, L. G. Cancela, and J. L. Rebola, "Impact of physical layer impairments on multi-degree cdc roadm-based optical networks,"in 2018 International Conference on Optical Network Design and Modeling (ONDM), 2018, pp. 94–99.
[Sha24]	H. Shakespear-Miles, Q. Lin, S. Barzegar, M. Ruiz, X. Chen, and L. Velasco, "Centralized and distributed approaches to control optical point-to-multipoint systems near-real-time," IEEE/OPTICA Journal of Optical Communications and Networking, 16, 565-575 (2024).
[Sou22]	A. Souza, N. Costa, J. Pedro and J. Pires, "Benefits of counterpropagating Raman amplification for multiband optical networks," in *Journal of Optical Communications and Networking*, vol. 14, no. 7, pp. 562-571, July 2022
[Sou22-2]	A. Souza, A. Eira, N. Costa, et al., "On the impact of fault-induced power transients in wideband optical networks," in 2023 Optical Fiber Communications Conference and Exhibition (OFC), (2023), pp. 1–3.
[Sou23]	A. Souza, N. Costa, J. Pedro, and J. Pires, "Comparison of fast quality of transmission estimation methods for C+L+S optical systems," J. Opt. Commun. Netw. 15, F1–F12 (2023).

[Sou24]	A. Souza, N. Costa, J. Pedro, and J. Pires, “Comparative assessment of S+C+L-band and E+C+L-band systems with hybrid amplification,” in 2024 Optical Fiber Communications Conference and Exhibition (OFC), (2024), pp. 1–3.
[SRIA]	Strategic Research and Innovation Agenda 2021-27, European Technology Platform NetWorld2020 "Smart Networks in the context of NGI” https://bscw.5g-ppp.eu/pub/bscw.cgi/d367342/Networld2020%20SRIA%202020%20Final%20Version%202.2%20.pdf.
[Sul22]	Sulaiman, M.; Moayyedi, A.; Salahuddin, M.A.; Boutaba, R.; Saleh, A. Multi-agent deep reinforcement learning for slicing and admission control in 5G C-RAN. In Proceedings of the IEEE/IFIP Network Operations and Management Symposium, Budapest, Hungary, 25–29 April 2022.
[Tak11]	K. Takenaga, Y. Arakawa, Y. Sasaki, et al., “A large effective area multi-core fibre with an optimised cladding thickness,” in European Conference and Exhibition on Optical Communication (2011).
[Tak20]	M. Takahashi, K. Maeda, K. Aiso, et al., “Uncoupled 4-core fibre with ultra-low loss and low inter core crosstalk,” in European Conference on Optical Communications (ECOC) (2020).
[Tan21]	T. Tanaka, T. Inui, S. Kawai, S. Kuwabara, and H. Nishizawa, “Monitoring and diagnostic technologies using deep neural networks for predictive optical network maintenance,” Journal of Optical Communications and Networking, vol. 13, no. 10, pp. E13–E22, 2021.
[Tor24]	P. Torres-Ferrera et al., “Validation of digital subcarriers coherent transceivers for mobile transport applications in 5G radio access networks,” in ONDM 2024, (2024).
[Uzu21]	D. Uzunidis, E. Kosmatos, C. Matrakidis, A. Stavdas, and A. Lord, “Strategies for upgrading an operator’s backbone network beyond the cband: Towards multi-band optical networks,” IEEE Photonics Journal, vol. 13, no. 2, pp. 1–18, 2021.
[Vel17]	L. Velasco and M. Ruiz, *Provisioning, Recovery and In-operation Planning in Elastic Optical Networks* (Wiley, 2017), Chap. 11.
[Vel23]	L. Velasco, P. González, and M. Ruiz, "Distributed Intelligence for Pervasive Optical Network Telemetry," IEEE/OPTICA Journal of Optical Communications and Networking (JOCN), vol. 15, pp. 676-686, 2023.
[Vir21]	E. Virgillito, E. London, A. D’Amico, B. Correia, A. Napoli and V. Curri, "Single- vs. Multi-Band Optimized Power Control in C+L WDM 400G Line Systems," *2021 Optical Fiber Communications Conference and Exhibition (OFC)*, San Francisco, CA, USA, 2021, pp. 1-3.
[Wel21]	D. Welch, A. Napoli, J. Bäck, et al., “Point-to-multipoint optical networks using coherent digital subcarriers,” J. Lightwave Technol. 39, 5232–5247 (2021).
[Win13]	P. J. Winzer, “Spatial multiplexing: the next frontier in network capacity scaling,” in European Conference and Exhibition on Optical Communication (ECOC) (2013), pp. 372–374.
[Win23]	P. J. Winzer, "The future of communications is massively parallel," in *Journal of Optical Communications and Networking*, vol. 15, no. 10, pp. 783-787, October 2023.
[Yan23]	M. P. Yankov, F. Da Ros, U. C. de Moura, A. Carena and D. Zibar, "Flexible Raman Amplifier Optimization Based on Machine Learning-Aided Physical Stimulated Raman Scattering Model," in *Journal of Lightwave Technology*, vol. 41, no. 2, pp. 508-514, 15 Jan.15, 2023.

[Ye14]	F. Ye, J. Tu, K. Saitoh, et al., “Simple analytical expression for crosstalk estimation in homogeneous trench-assisted multi-core fibers,” Opt. Express 22, 23007–23018 (2014).
[Zha23]	D. Zhang, M. Zuo, H. Chen, D. Ge, Z. Feng, B. Yan, D. Wang, H. Shi, S. Cao, Y. Li, L. Han, B. Ye, Y. He, T. Wang, and H. Li, “Technological prospection and requirements of 800g transmission systems for ultra-long-haul all-optical terrestrial backbone networks,” Journal of Lightwave Technology, vol. 41, no. 12, pp. 3774–3782, 2023.